論文 / 著書情報
Article / Book Information

題目(和文)	有機電界効果トランジスタにおける化学ドーピングと電荷注入
Title(English)	Chemical Doping and Charge Injection in Organic Field-Effect Transistors
著者(和文)	角屋智史
Author(English)	Tomofumi Kadoya
出典(和文)	学位:博士(工学), 学位授与機関:東京工業大学, 報告番号:甲第9757号, 授与年月日:2015年3月26日, 学位の種別:課程博士, 審査員:森　健彦,大内　幸雄,ﾊﾞｯﾊ　ﾏｰﾃｨﾝ,松本　英俊,腰原　伸也
Citation(English)	Degree:Doctor (Engineering), Conferring organization: Tokyo Institute of Technology, Report number:甲第9757号, Conferred date:2015/3/26, Degree Type:Course doctor, Examiner:,,,,
学位種別(和文)	博士論文
Type(English)	Doctoral Thesis

Chemical Doping and Charge Injection in Organic Field-Effect Transistors

Tomofumi Kadoya

Department of Organic and Polymeric Materials
Tokyo Institute of Technology

February, 2015

A THESIS SUBMITTED TO TOKYO INSTITUTE OF TECHNOLOGY
FOR THE DOCTOR DEGREE OF ENGINEERING

Acknowledgements

The present thesis is a summary of the author's studied from 2012 to 2015 at the department of organic and polymeric materials, Tokyo Institute of Technology under the directions of Prof. Takehiko Mori. The author is grateful to Prof. Takehiko Mori. First, he has given me an interesting subject of the research, and the chance to challenge. He always manages and keeps our laboratory comfortable. Such his support prompts the author to work more hard. Second, he also assisted me giving the appreciate advice, and having the practical discussion. The present research could not have been carried out without his distinguished direction covering the whole field of the present work. It is one of the author's prize that the author becomes to be *the* researcher like him, although very difficult.

Assistant Prof. Tadashi Kawamoto usually supports the students in Mori laboratory, including the author, and teaches about the solid physics in organic superconductors to us. The author also appreciates his careful supporting.

The author would like to thank the members of Mori laboratory (Tokyo Institute of Technology). Everyone is unique and always kinds to the author. It is my great pleasure to spend a lot of fun time with them. The author wishes that collaboration with T. Higashino and Dr. H. Kojima any numbers of times.

The author would like to express special thanks to Prof. Dominique de Caro, Prof. Lydie Valade, and Prof. Christophe Faulmann (Laboratorire de Chimie de Coordination du CNRS, France) for the collaboration.

The author is grateful to Dr. Kotani and Prof. Nakamura. They also prompt the author to decide the master and doctor courses. The author is also deeply grateful to

JSPS for a research fellow ship.

Finally, the author also wishes to thank his family for their financial and wholehearted supports.

February, 2015

Tomofumi Kadoya

TABLE OF CONTENTS

Chapter 1. General Introduction

Chapter 2. Experimental Section

Chapter 5. A Highly Conducting Organic Charge-Transfer Complex $(BTBT)_2PF_6$

Chapter 6. Suppression of Access Resistance by Using Carbon Electrodes in Organic Transistors Based on Alkyl-Substituted Thienoacene

Chapter 1

General Introduction

1.1 History of organic conductors

In general, organic compounds have been considered to be insulators for a long time. However, graphite is regarded as an analog of organic materials, but it shows metallic conductivity.[1] Conductivity of graphite is attributed to the molecular structure composed of network of the conjugated double bonds of carbon atoms with π-electrons. To investigate the origin of the charge transport, the research of conductivity of organic materials has started from the conducting properties of aromatic hydrocarbons.

In 1950, H. Akamatu and his co-workers reported that condensed polycyclic aromatic compounds showed electric conductivity with semiconductor-like temperature dependence, and these compounds were named as organic semiconductors.[2] In 1954, the same group reported that the perylene-bromine complex showed as low resistivity as 10 Ω cm.[3] These results prompted the research in organic conductors. In 1973, a charge-transfer (CT) complex composed of tetrathiafulvalene (TTF, Figure 1-1) as an electron donor and 7,7,8,8,-tetracyano-*p*-quinodimethane (TCNQ, Figure 1-1) as an electron acceptor was found to show metallic conductive behavior down to 53 K.[4] The first organic superconductivity was achieved in a radical-cation salt of tetramethyl tetraselenafulvalene (TMTSF, Figure 1-1) in 1980. In the TMTSF molecule, four sulfur atoms of TTF were replaced by selenium atoms for enhancing the intermolecular interaction between the adjacent stacks. The $(TMTSF)_2PF_6$ salt showed

superconductivity below 0.9 K under the pressure of 12 kbar.[5] In 1988, H. Urayama *et al* reported that κ-(BEDT-TTF)$_2$Cu(NCS)$_2$ (BEDT-TTF, Figure 1-1) showed superconductivity at ambient pressure with high T_C of 10.4 K.[6] In 2005, a giant nonlinear resistance effect was reported in an organic salt θ-(BEDT-TTF)$_2$CsCo(SCN)$_4$ as well as a spontaneous current oscillation phenomenon called as an organic thyristor.[7] In this connection, organic conductors are expected to play an important role in organic electronics in the near future.

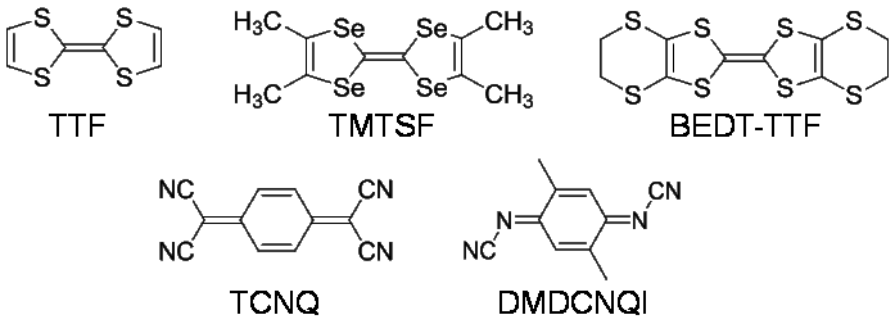

Figure 1-1. Molecular structures of representative organic donors and acceptors.

(a) (b)

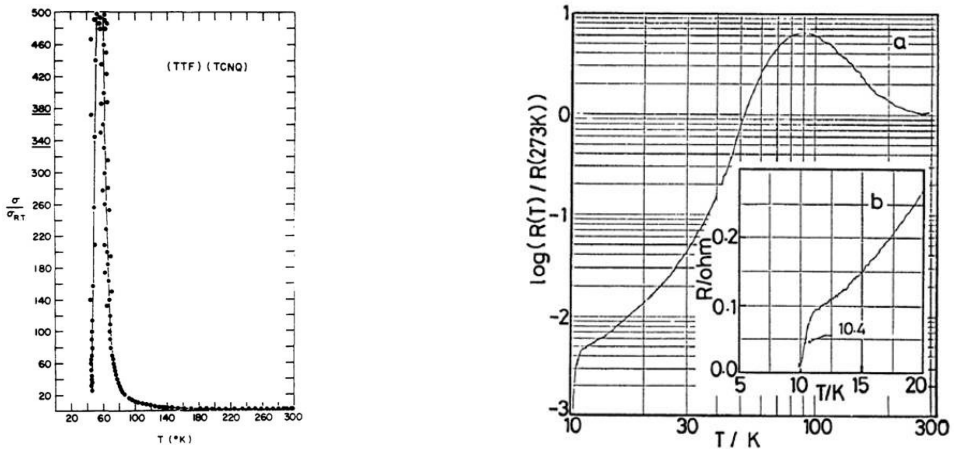

Figure 1-2. Temperature dependence of (a) conductivity of (TTF)(TCNQ)[4] and (b) resistivity of κ-(BEDT-TTF)$_2$Cu(NCS)$_2$.[6]

1.2 Redox potentials in organic donors and acceptors

Since the discovery of high conductivity in CT salts, several proposals have been suggested to design new organic metals. As mentioned in 1.1, (TTF)(TCNQ) is a representative metallic CT salt. (TTF)(TCNQ) is composed of an electron donor (TTF) and an acceptor (TCNQ), and the conductivity comes from the partial charge transfer from HOMO of TTF to LUMO of TCNQ. Naively speaking, when the donor HOMO is higher than the acceptor LUMO, CT takes place entirely, resulting in an ionic state. However, if the acceptor LUMO is much higher than the donor HOMO, CT takes place only in a very small extent, and this is called a ‘‘neutral’’ CT complex, in contrast to the ‘‘ionic’’ CT complex. In both of these CT salts, donor and acceptor molecules usually stack alternately to form mixed stacks (Figure 1-3 (a)). These complexes are insulators in many cases. On the other hands, partially charge transferred CT complexes such as (TTF)(TCNQ) have segregated stacks, where the donor and the acceptor molecules construct independent columns. These complexes are usually highly conductive in the direction of the columns (Figure 1-3 (b)).

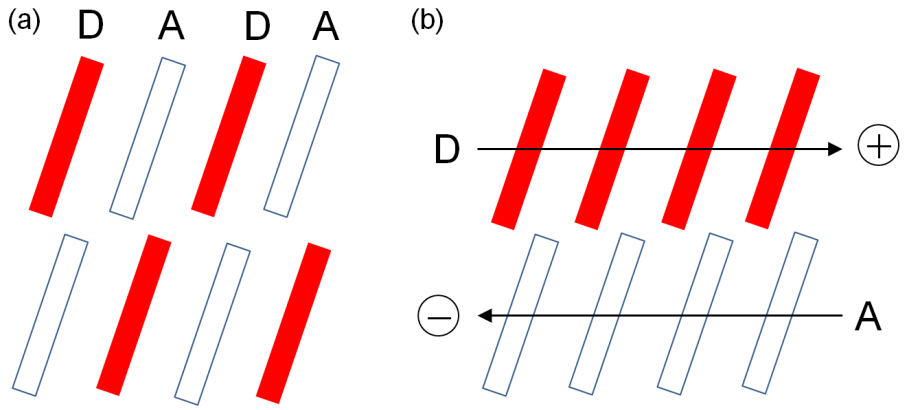

Figure 1-3. Schematic images of (a) mixed-stack, and (b) segregated structures of donor (D) and acceptor (A) molecules in CT complexes.

It is necessary that an electron is easily removed from the HOMO to the LUMO at the time of charge transfer, so HOMO and LUMO levels are key parameters for the properties of the CT salts. G. Saito and John P. Ferraris have reported that there is a high possibility of making ‘‘organic metals’’ when the donor and the acceptor have the redox potentials of the range, $-0.02 \leq E_1(\mathrm{D}) - E_1(\mathrm{A}) \leq 0.34$ V, where the E_1 values are the first electrochemical half-wave potentials for $\mathrm{D} \rightarrow \mathrm{D}^+ + \mathrm{e}$ and $\mathrm{A} + \mathrm{e} \rightarrow \mathrm{A}^-$, respectively.[8] Conductivities of such complexes are plotted in Figure 1-4. The complexes in the upper left of the figure have small (I–A) values, where I is the ionization potential of a donor, and A is the electron affinity of an acceptor, and tend to generate completely charge transferred ionic states. Those on the lower right tend to give neutral states. The complexes which are insulators or semiconductors are represented by triangles, whereas open circles designate highly conducting complexes and closed circles are metallic CT salts. In general, metallic CT salts such as (TTF)(TCNQ) are located between the two red lines. There are, however, a few exceptions. For example, although the origin is uncertain, (BEDT-TTF)(TCNQ), located out of the red-line region, is highly conducting.[9]

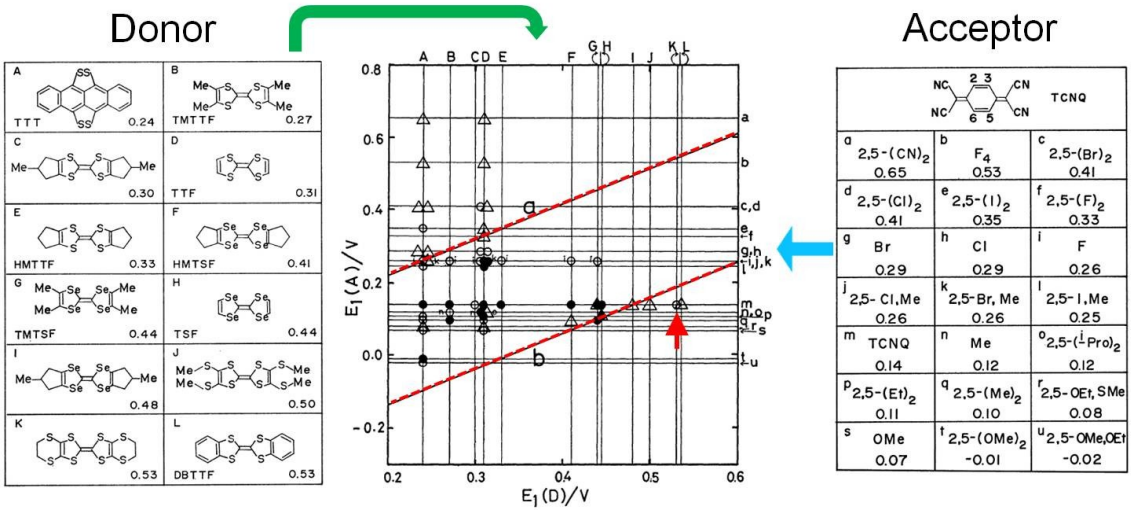

Figure 1-4. Conductivity of complexes plotted as E_1 (A) vs. E_1 (D).
Δ = insulators or semiconductors; ○ = highly conducting CT salts; ● = ‘‘organic metals’’ (BEDT-TTF)(TCNQ) is located at the top of the arrow.[8]

1.3 Metal-insulator transition in organic conductors: Peierls transition

Since most of organic conductors have a one-dimensional electric state due to the molecular stacking structure, a metal-insulator (MI) transition, which is sometimes called a metal-semiconductor transition, occurs at low temperatures. The MI transition is categorized depending on the insulator phases. In particular, “Peierls transition” is the most popular insulating phase in organic conductors. Consider a one-dimensional metal at 0 K (Figure 1-5). In the absence of electron-electron and electron-phonon interactions, the energy band is partly filled up to the Fermi level E_F, where the molecules form a uniform arrangement with a molecular spacing a. In the presence of electron-phonon interaction, however, the molecules are displaced with a periodicity of λ related to the Fermi wave vector k_F,

$\lambda = \pi / k_F$.

This distortion opens a gap at the Fermi levels as shown in Figure 1-5, and stabilizes the electric states. This is because of the nesting of the Fermi surface, in which the decrease in energy is expected from the perturbation theory. Although the distortion gives rise to an increase of the lattice energy, the destabilization is not as large as the electric stabilization owing to the Peierls distortion.

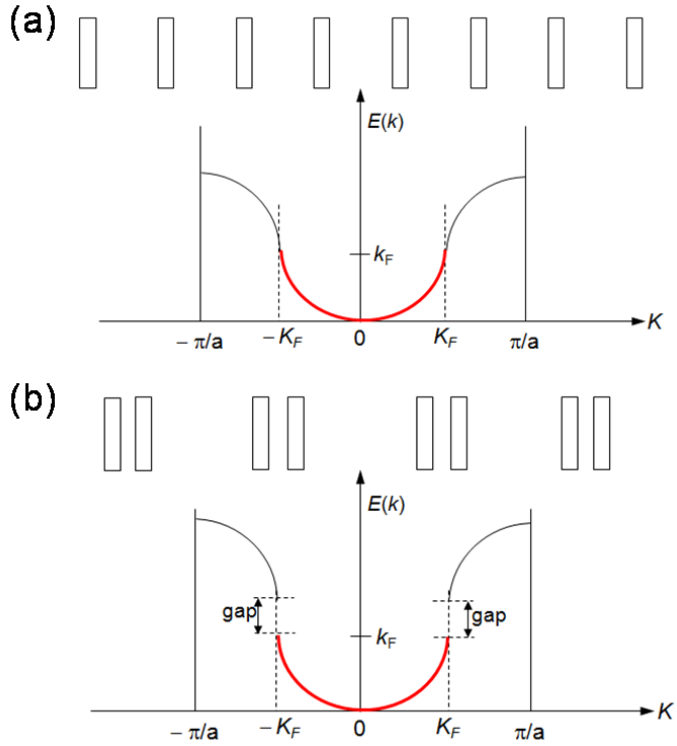

Figure 1-5. Energy band in a one-dimensional half-filled conductor in (a) an undistorted metal, and (b) the Peierls insulator.

If the energy band is half-filled, the $2k_F$ charge density wave (CDW) develops along the array of molecules with periodicity $2a$. After the Peierls transition, magnetic susceptibility goes down to zero at low temperatures. There is no magnetic anisotropy in the non-magnetic state.

1.4 Charge transfer at the interface between TTF and TCNQ

(TTF)(TCNQ) is one of the most famous one-dimensional organic conductors. In 2008, it has been reported that metallic conductivity is realized at the interface between TTF and TCNQ single crystals.[10] Since the energy levels of TTF and TCNQ are very similar, the origin of this phenomenon is probably ascribed to the molecular-level charge transfer at the interface between the two crystals. Y. Takahashi et al. have investigated the interface more precisely. According to the Raman spectroscopy, the charge transfer occurs and nanocrystals of (TTF)(TCNQ) are formed at the TTF/TCNQ interface.[11] Therefore, the metallic conductivity is observed at the TTF/TCNQ interface.

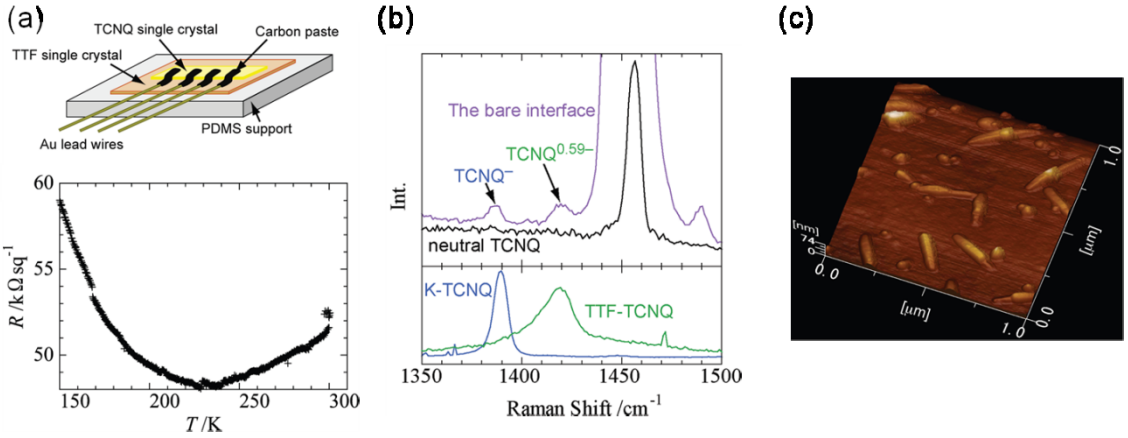

Figure 1-6. (a) Configuration for the conductivity measurement of the laminated interface between TTF and TCNQ single crystals, and temperature dependence of the resistance of the laminated sample. (b) Raman spectra of the bare interface on the TCNQ single crystal, TCNQ, (TTF)(TCNQ), and K(TCNQ). (c) AFM image of the bare interface on the TCNQ single crystal after removing the TTF crystal.[11]

1.5 Organic field-effect transistors

Recently, organic electronics using organic semiconductors have been developed rapidly, and have been applied to organic light-emitting diode (OLED), organic photonics, and organic field-effect transistors (OFETs).

The principle of a transistor stems from the ideas by J. E. Lilienfeld in 1925 and by O. Heil in 1934.[12] They, however, did not publish any research papers about their ideas. The first real transistor on the basis of their principles was realized by using germanium at the Bell laboratory in 1947. The discovery was reported by J. Bardeen, W. Brattain, and W. Schockley, yet they did not publish the discovery in any papers.

A transistor is a semiconductor device commonly used to amplify and switch electronic signals in electronic circuits. Today, a transistor is used in many circumstances and included in modern electronic instruments such as cell phones, personal computers, and displays. Most transistors are incorporated in integrated circuits (ICs).

Transistors are largely classified into two types: a bipolar transistor and a field-effect transistor (FET). Difference of a bipolar transistor and a FET comes from the device structure and the application. Bipolar transistors are constructed from p-n junctions and are the first transistors which are mass-produced. Since in a bipolar transistor, large collector-emitter currents are controllable by relatively small input current, they are useful in amplifiers, so that they are used in audio amplifiers in Hi-Fi systems. The FET is sometimes called a unipolar transistor in contract to a bipolar transistor, because either electrons or holes take part in the conduction. Compared to bipolar transistors, FET is operated with a low current, so FET is an indispensable device in an integrated circuit (IC). Although the usual FETs are constructed from

semiconductors such as silicon and GaAs, OFETs made of organic compounds have attracted much attention due to their potential application to flexible and low-cost electronics.[13]

1.6 Mechanism of OFET

1.6.1 Principles of operation

Figures 1.7(a) and (b) show schematic structures of bottom-contact (BC) and top-contact (TC) OFET geometries, which are commonly used in OFETs. It is noteworthy that a FET has three terminals, which are source, drain, and gate electrodes connected to external electronic circuits. When a gate voltage V_G is zero, the source-drain current I_D does not flow; the device is in the "off" state (Figure 1-7(c)). When V_G is applied, carriers are injected from the source and accumulated on the organic semiconductor-dielectric interface. This is the "on" state, and I_D flows (Figure 1-3(d)). The charge carrier is electron in an n-type semiconductor when $V_G > 0$. On the other hand, holes are generated in a p-type semiconductor when $V_G < 0$.

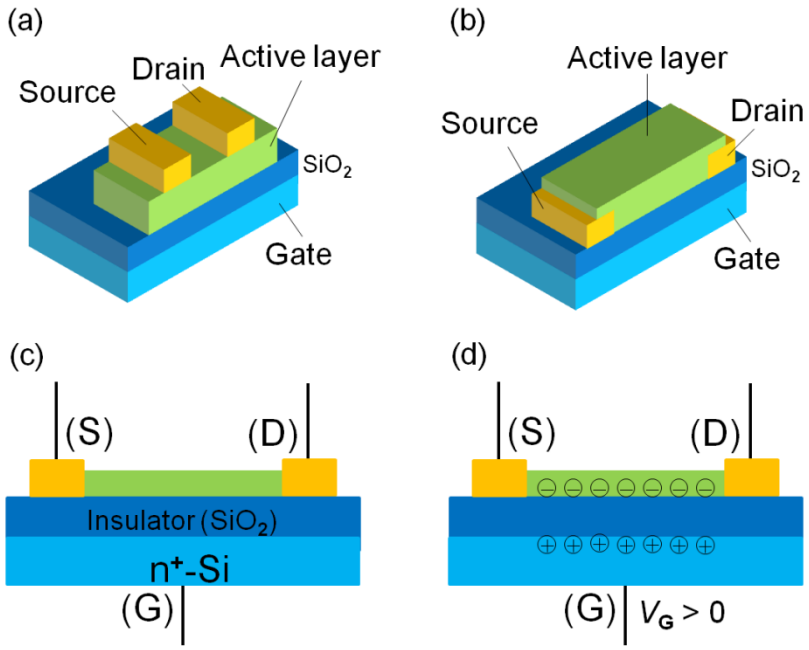

Figure 1-7. Geometry of (a) bottom and (b) top contact OFETs. Schematic structures of (c) the "off" state and (d) the "on" state.

1.6.2 Linear and saturation regions

Figure 1-8 shows a schematic model of an OFET in the linear and the saturation regimes with the potential shift between the source and the drain. If a small drain voltage is applied, a current flows from the source to the drain through the channel. The drain current I_D is proportional to the drain voltage V_D. This is the linear region (Figure 1-8(a)). As the drain voltage increases, the actual voltage between the gate and the channel at x is reduced to $V(x) = V_G - V_{th} - V_C(x)$ in the gradual channel approximation (Figure 1-8(d)). When $V_D + V_{th}$ reaches V_G, $V(x)$ at $x = L$ is eventually reduced to 0 V. This is called the pinch off (Figure 1-8(b)). Beyond the pinch off, the channel region is not uniform and vanishes near the drain (Figure 1-8(c)). The drain current, however, remains essentially the same in the whole channel region, and the carriers arriving at the point X move to the drain due to the large electric field. Beyond the pinch off, the device enters the saturation region (Figure 1-8(c)).

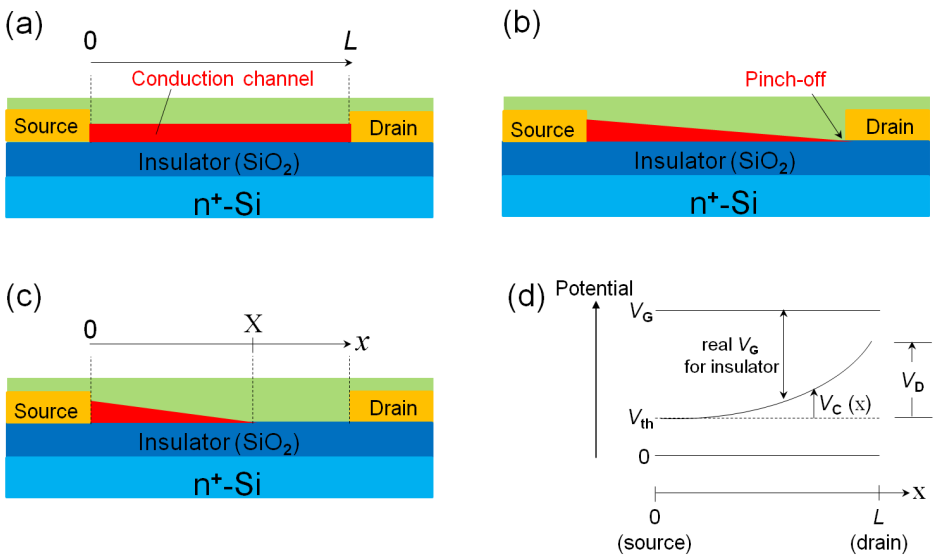

Figure 1-8. OFET operated in (a) linear region (b) pinch-off state (c) saturate region and (d) potential shift between the source and drain.

Under the idealized conditions, the source-drain current is obtained as follows. The total accumulated charge density in a semiconductor per unit area Q at a distance x from the source is given by

$$Q(x) = -C_{\mathrm{OX}}\{(V_{\mathrm{G}} - V_{\mathrm{th}}) - V_{\mathrm{C}}(x)\} \quad (1)$$

where C_{OX} is the capacitance per unit area, $V_{\mathrm{C}}(x)$ is the channel potential at point x. Since I_{D} is constant and independent of x, I_{D} is given by

$$I_{\mathrm{D}} = WQ(x)\mu E(x) = WQ(x)\mu\left(-\frac{dV_{\mathrm{C}}(x)}{dx}\right) \quad (2)$$

where W is the channel width, μ is the carrier mobility, which are postulated as constant in the channel, and $E(x)$ is the electric field in the channel along x. Substituting Eq. 1 into Eq. 2 and integrating from the source ($x = 0$) to the drain ($x = L$), it yields

$$\int_0^L I_{\mathrm{D}}\, dz = \int_0^L WC_{\mathrm{OX}}(V_{\mathrm{G}} - V_{\mathrm{th}} - V_{\mathrm{C}})\mu\frac{dV_{\mathrm{C}}}{dz}dz$$

$$I_{\mathrm{D}} = \frac{W}{2L}\mu C_{\mathrm{OX}}\{2(V_{\mathrm{G}} - V_{\mathrm{th}})V_{\mathrm{D}} - V_{\mathrm{D}}^2\}. \quad (3)$$

According to Figure 1-4(d), the voltage to achieve the saturate region is given by

$$V_{\mathrm{D}\,sat} = V_{\mathrm{G}} - V_{\mathrm{th}}. \quad (4)$$

The saturated current $I_{\mathrm{D}\,sat}$ is obtained by substituting Eq. 4 into Eq. 3:

$$I_{\mathrm{D}\,sat} = \frac{W}{2L}\mu C_{\mathrm{OX}}(V_{\mathrm{G}} - V_{\mathrm{th}})^2. \quad (5)$$

Eq. 5 represents that $I_{\mathrm{D}\,sat}$ increases as a square of V_{G}.

Figure 1-9 shows the output and transfer characteristics. An output characteristics is a plot of I_{D} vs. V_{D} for different values of V_{G}. The output characteristics is categorized into two regions: the linear region and the saturation region. In the linear region, I_{D} increases proportionally to V_{D} by satisfying Eq. 3, and finally approaches the saturation. In the saturation region, the value of I_{D} is constant

with increasing V_D as represented by Eq. 5. On the other hand, the transfer characteristics is a plot of I_D vs. V_G. There are two regions: the ‘‘off’’ state and the ‘‘on’’ state. In the off state, I_D does not flow. When the applied V_G exceeds a certain value defined as the threshold voltage V_{th}, I_D increases drastically in proportion to V_G^2. In general, carrier mobility μ and threshold voltage V_{th} are evaluated from the transfer characteristics.

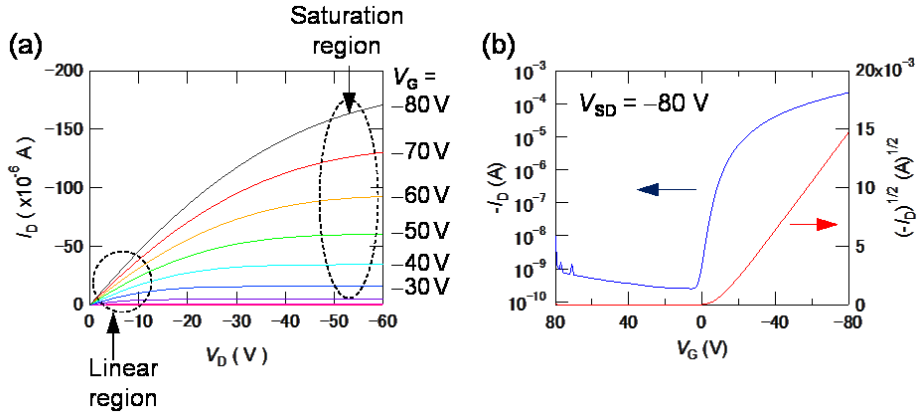

Figure 1-9. (a) Output and (b) transfer characteristics of a pentacene transistor.

1.6.3 Band bending at the metal-semiconductor interface

In general, it seems that energy bands are bending at the boundary of metal electrode and semiconductor. The Fermi levels of the metal and the organic layer are usually different. If the metal electrode and the semiconductor are close to each other, tunneling effect occurs and electrons are transferred. We consider an interface of a metal and a p-type semiconductor, where the HOMO level (valence band) of the semiconductor is close to E_F (Figure 1-10(a)). When the Fermi level of the metal is lower than that of the semiconductor, holes are transferred from the metal to the semiconductor HOMO. Then the energy level of the semiconductor drops as shown in Figure 1-10(a). The downward band bending makes a hole accumulation layer at the interface, giving rise to the energy shift and the interfacial polarization. On the other hand, we consider an n-type semiconductor, where the LUMO level (conduction band) of the semiconductor is close to E_F. If the Fermi level of metal is higher than that of semiconductor, electrons are moved from metal to semiconductor (Figure 1-10(a)). After transferred, the Fermi levels at the interface are completely adjusted. In Figure 1-10(b), hole transfer leads to negative charge at the metal and positive charge at the semiconductor. Similarly, electron transfer results in positively charged metal and negatively charged semiconductor. In the both cases, an electric field occurs at the metal-semiconductor interface and the bands bend.

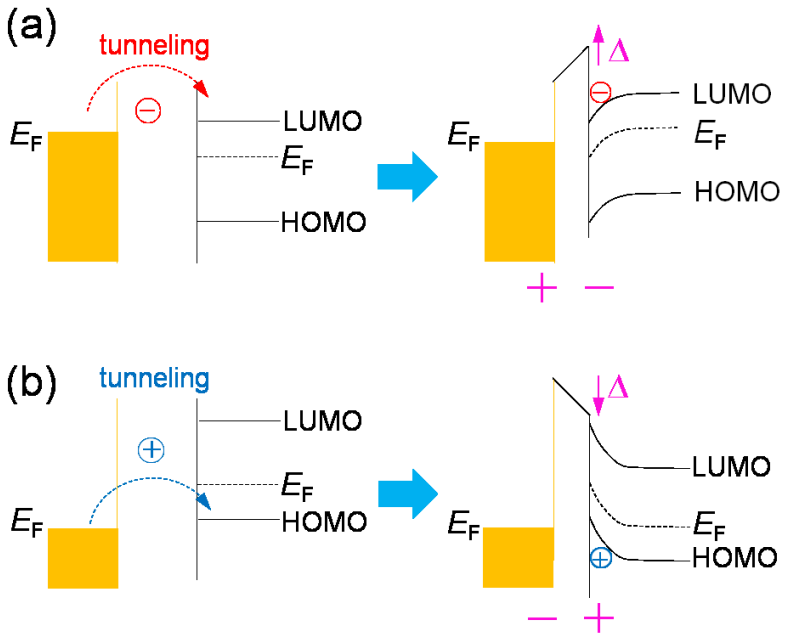

Figure 1-10. Interfacial energy diagram at metal/semiconductor.

1.6.4 Charge injection barriers

In a semiconductor, there are no free carriers on LUMO and HOMO and I_D does not flow even if V_D is applied. Free carriers are injected from the metal electrode. Now we assume an ideal case with no traps. In the case of Figure 1-11, the injection barrier heights at the interface is Φ_B^p for holes and Φ_B^n for electrons

$$\Phi_B^p = I - \Phi_m + \Delta$$

$$\Phi_B^n = \Phi_m - A - \Delta = E_g - \Phi_B^p$$

where I is the ionization energy, Φ_m is work function of the metal, Δ is the interfacial potential, and A is the electron affinity.

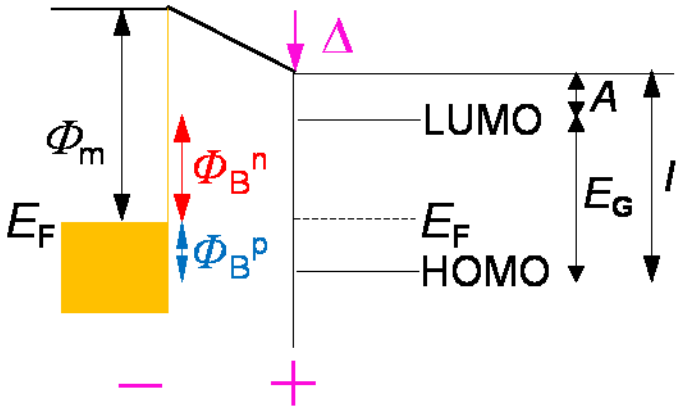

Figure 1-11. Injection barrier at the metal/organic semiconductor interface.

From this mechanism, it seems that both electron and hole can be respectively injected to LUMO and HOMO, when sufficiently large voltage is applied. Many organic semiconductors are, however, dominantly only electron or hole transport. As mentioned above, there are two types of injection barriers in semiconductors, but if Φ_B^p is smaller than Φ_B^n, hole injection is dominant, and the semiconductor is categorized as p-type. In contrast, electron transport is advantageous in n-type semiconductors where Φ_B^n is smaller than Φ_B^p. If the Fermi level of the metal is located at the center of the semiconductor LUMO and HOMO, and E_G is relatively small, ambipolar transport is expected.

1.7 Development of OFET

1.7.1 p-type OFETs

The first OFET was reported in 1984 on the basis of merocyanine, although the resulting mobility was as low as 1.5 x 10^{-5} cm^2/Vs.[14] The successive development of OFET, however, has realized performance comparative to amorphous silicon (a-Si) thin-film transistors (TFT) (~1 cm^2/Vs), as shown in Figure 1-12. Although the performance is still lower than those of polycrystalline silicon (~10^2 cm^2/Vs) and crystal silicon (~10^3 cm^2/Vs), interests in OFET have been increased owing to their potentials to easy processing and mechanical flexibility; these properties are difficult to attain in inorganic semiconductors.

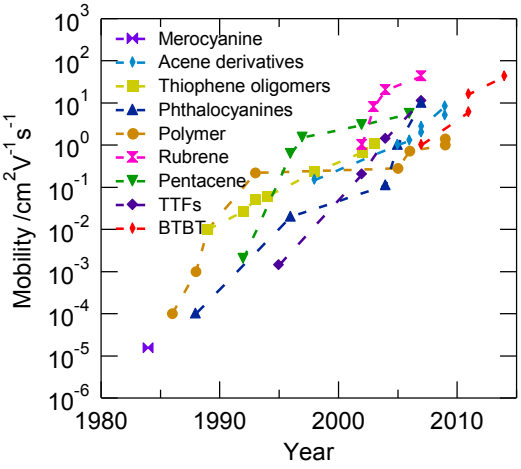

Figure 1-12. Evolution of OFET hole mobility for the representative p-type organic semiconductors. For comparison, a representative range of electron mobility for a-Si:H TFT is shown.

A variety of organic semiconductors have been developed for the use in OFET, and the record mobility has been significantly improved over the past two decades (Figure 1-12).[15] Recent rapid development of new materials is notable, and high

performance materials whose mobility exceeding 1 cm^2/Vs have been successively reported; particularly, progress is remarkable for solution-process materials, and for single-crystal transistors. Representative materials are poly- and oligothiophenes, acenes, tetrathiafulvalene derivatives, and metal-phthalocyanines. These are p-type semiconductors (Figure 1-13).[12-22] Field-effect mobilities of these materials have improved to the order of more than 10^{-2} cm^2/Vs, and are sufficient for the practical use. Some compounds such as polymers and derivatives with long alkyl chains have been used in solution process. The use of soluble organic semiconductors has prompted the development of printing technique. In general, the device characteristics fabricated by solution process are relatively low due to their low crystallinity and amorphous properties. However, H. Minemawari et al. have reported that single-crystal films fabricated by inkjet printing achieve the average carrier mobility of over 16 cm^2/Vs.[17] There is an increased interest in solution-process OFETs from the viewpoint of practical applications. Vacuum evaporated thin films of small molecules have good crystallinity, and the ordered molecular orientation results in high device performance. Pentacene is a representative p-type semiconductor with a mobility exceeding 1 cm^2/Vs.[16]

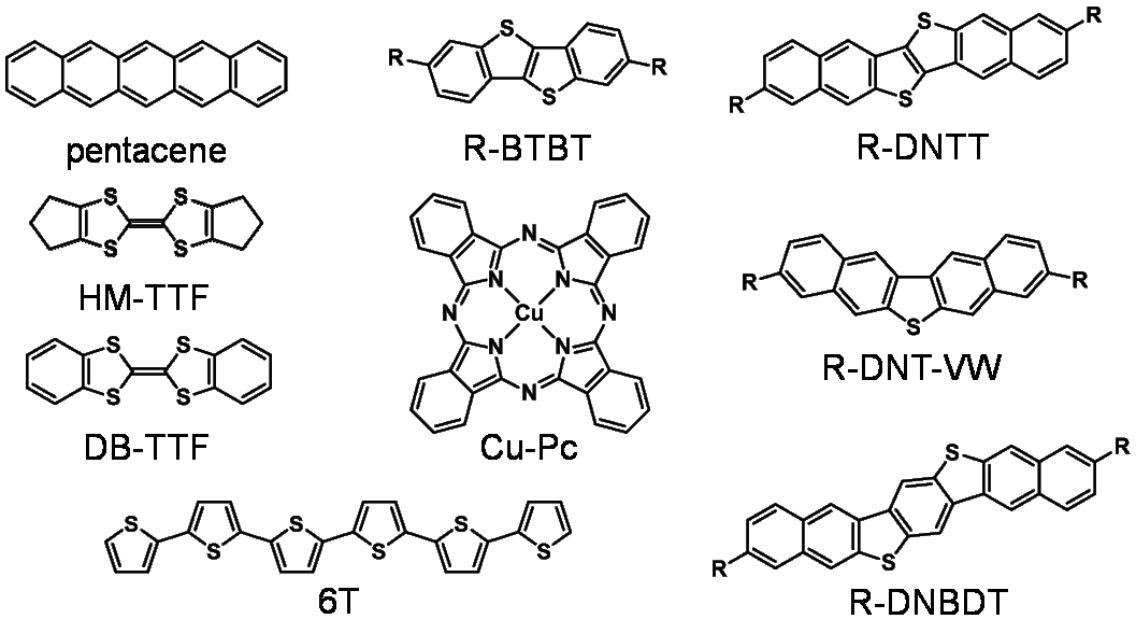

Figure 1-13. Representative p-type OFET materials. Pentacene: 3 cm^2/Vs,[16] R-BTBT: 31–43 cm^2/Vs,[17] HM-TTF: single crystal 11 cm^2/Vs,[18] 5.5 cm^2/Vs[19] DB-TTF: single crystal 1 cm^2/Vs,[20] 0.55 cm^2/Vs,[21] Cu-Pc: 0.02 cm^2/Vs,[22] 6T: 0.03 cm^2/Vs,[23] R-DNTT: 7.9 cm^2/Vs,[24] R-DNT-VW: 4–9.5 cm^2/Vs,[25] R-DNBDT: 16 cm^2/Vs,[26]

1.7.2 Molecular arrangements in organic semiconductors

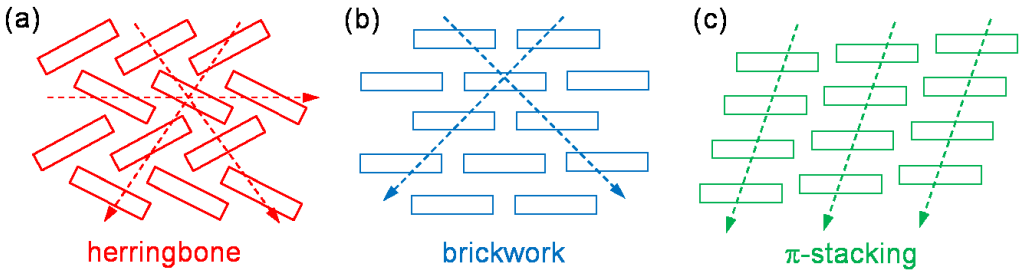

Figure 1-14. Molecular packing of (a) herringbone, (b) brickwork, and (c) π-stacking viewed along the molecular long axis.

Molecular packing is important characteristics in OFETs because the molecular-orbital overlaps form the charge-carrier pathways. An appropriate overlap significantly increases the mobility. Therefore the crystal structure is important for the carrier transport. The single-crystal packing also influences the thin-film morphology.

In many cases, organic molecules are standing perpendicular to the substrate. This is called as the "edge-on" geometry and results in straightforward conduction pathways. Figure 1-14 shows the representative packing motifs in edge-on geometry.

The herringbone structure is most popular among the crystal structures of straight-shaped molecules such as acenes and benzothienobenzothiophenes. The molecular planes are inclined from each other when viewed along the molecular long axis, and are governed by the edge-to-face intermolecular interactions owing to the CH-π interactions. Thus the small C/H ratio leads to this tilted arrangement.[27] The dihedral angles vary in the range of 40°–130° for the usual organic semiconductors. The conduction pathways are found not only along the molecular stacking but also in the intercolumnar directions. The two-dimensional transport is advantageous in such a disordered state as thin films, and tends to show high mobility.

The brickwork structure is another type of two-dimensional molecular packing. All molecules are parallel to each other, but instead of forming the usual stacking structure, two molecules are equivalently located on the top of a molecule. In this face-to-face overlap, the molecules are slipped largely along the molecular short axis, and the resulting intermolecular interactions run in two diagonal directions. The compounds having an ideal brickwork structure are not many but exhibit relatively high mobility due to the two-dimensional structure.

In contrast, the π-stacking structure has one-dimensional pathways, where the molecules have face-to-face parallel arrangement. The cofacial π-π interactions are predominant compared to the edge-to-face interactions, and large aromatic planar molecules tend to have this stacking arrangement. This structure has strong intermolecular interaction along the stacking, where the interplanar distance is usually

c.a. 3.4 Å. The cofacial molecules are often slipped along the long and short molecular axes from the eclipsed stack. Here, another molecule moves from the position exactly on the top of the original molecule (Figure 1-14(c)) in order to avoid the electronic repulsion. The uniform stacking results in relatively high conductivity, but when the stacked molecules are dimerized, the charge transport is prevented. The situation is further complicated when the molecules have twisted arrangement,[28] where the problem is not simple even in the one-dimensional transport.

1.7.3 n-type OFETs

Representative organic n-type semiconductors are shown in Figure 1-15.[29–35] In the last decade, there has been an increasing attention to n-type semiconductors. C_{60} and naphthalene tetracarboxy dianhydride derivatives are representative n-type organic semiconductors. So far, p-type organic materials for OFET have been found in various skeletons, but n-type OFET is relatively limited. There are several reasons why high-performance n-type organic semiconductors are difficult to realize in comparison with p-type organic semiconductors. The first is that most of n-type semiconductors are not stable in air. D. M. de Leeuw et al. have reported that n-type organic semiconductors are unstable with respect to oxidation by O_2 and H_2O. Although some n-type semiconductors are air stable, they have reported that the oxidation occurs at the redox potentials of 0.57 V and –0.66 eV (vs. SCE).[34] Second, electron traps exist at the interface between the organic semiconductors and dielectrics. For example, hydroxyl groups on insulators are electron traps and reduce the performance of n-type OFET considerably.[36] Third, metals typically used for electrodes, such as Au and Cu, have relatively deep work functions and are suitable for

hole injection into the HOMO levels than for electron injection to the LUMO of organic semiconductors. Another kind of metals such as Al, Mg, and Ca have small work functions, but these metals are oxidized easily and sometimes form reactive complexes with organic semiconductors. Accordingly, there are many problems to operate n-type OFET efficiently. However, electron mobilities over 1 cm^2/Vs have been reported in several organic semiconductors. It has been not completely understood yet why some organic semiconductors make air-stable n-type devices. For instance, semiconductors including $F_{16}CuPc$, several NTCDI (naphthalene-3,4,9,10-tetracarboxydiimide) derivatives, and TCNQ are known to be air-sensitive, in contrast, dimethyldicyanoquinonediimine (DMDCNQI) has been reported by H. Wada et al. to be air-stable.[33,34] In this context, synthesis of new air-stable n-type OFET materials has attracted much attention. The problem of electron traps is avoided by surface chemical modification, called ‘‘self-assembled monolayers (SAMs)’’ (Figure 1-16). Recently, SAMs such as 1,1,1,3,3,3-hexa-methlenedisilazane (HMDS) and octadecyltrichlorosilane (ODTS) have been widely used to modify the surface of the dielectric in order to reduce the surface energy and improve performance of not only n-type but also p-type OFET. Ito et al. have reported crystalline ultrasmooth SAMs of alkylsilanes (octadecyltrimethoxysilane OTMS) fabricated by spin-cast, resulting in much higher carrier mobilities for both p- and n-type OFET.[37] Iwasa et al. have demonstrated that the threshold voltage is shifted by using SAMs with fluorine or amino groups.[38] These SAMs have character of donor or acceptor in themselves, and weak charge transfer takes place at the interface between organic semiconductors and these SAMs. In addition, thiol treatment on Au electrodes has been used to improve the performance of bottom-contact transistors.

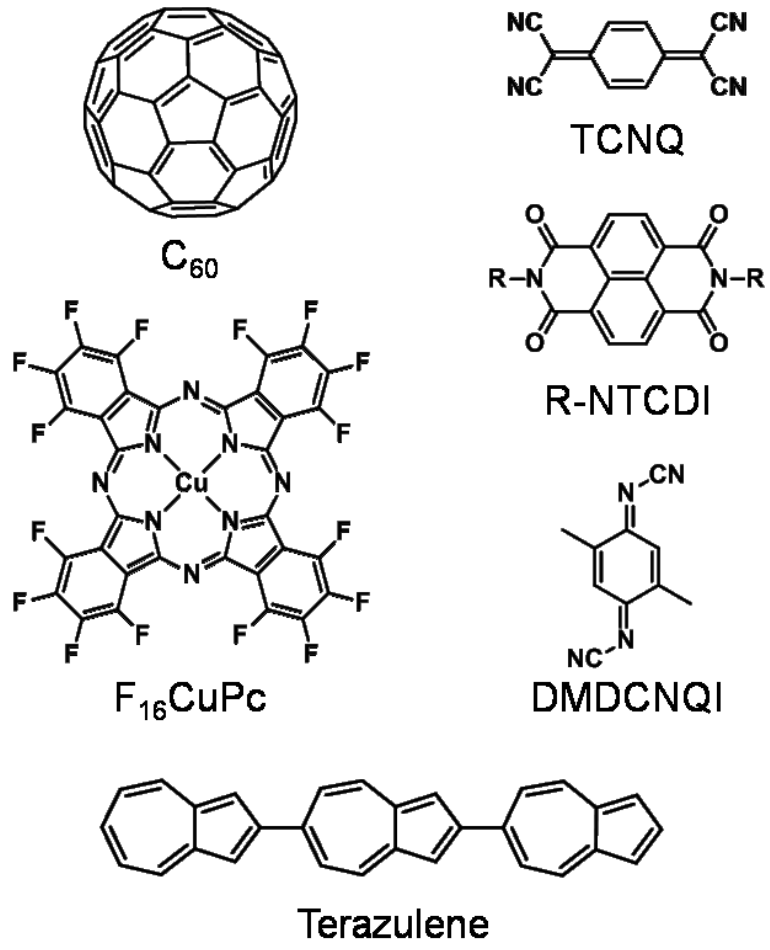

Figure 1-15. Representative n-type OFET materials. C_{60}: 6.0 cm^2/Vs[29], TCNQ: 3 x 10^{-5} cm^2/Vs[30], F_{16}Cu-Pc: 0.03 cm^2/Vs[31], R-NTCDI: 6.2 cm^2/Vs[32], DMDCNQI: 0.01–0.42 cm^2/Vs[33,34] Terazulene: 0.29 cm^2/Vs[35]

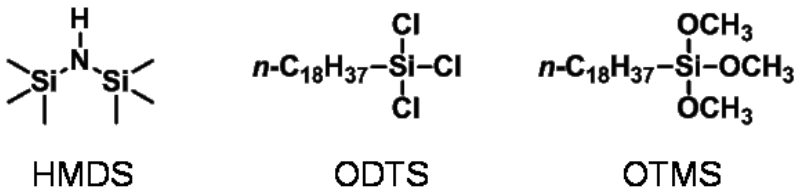

Figure 1-16. Molecular structures of HMDS, ODTS, and OTMS.

1.7.4 Ambipolor OFETs

Ambipolar organic semiconductors, where both electron and hole transports are possible in single-component materials, have recently attracted a lot of attention to design organic electronic devices. High-performance ambipolar transistors have been reported by using donor-acceptor (DA) polymers. A typical DA polymer is composed of thiophene and diketopyrrolopyrole (DPP). The resulting polymers show low band gap and high mobilities over 1 cm^2/Vs. As well as polymers, small-molecule ambipolar materials also show excellent properties. Indigo and Tyrian purple (6,6'-dibromoindigo), which have been well known as dye compounds, show ambipolar transport and attain well-balanced mobilities.[39] A very high melting point and low solubility in common organic solvents are inherent in indigo, and this is due to the stabilization coming from the inter- and intramolecular hydrogen bonds. Indigo derivatives are of interest not only as a natural dye but also as an ambipolar material, which is realized by the minimal molecular structure composed of the electron-donor nitrogen atoms together with the electron-acceptor carbonyl groups. In particular, remarkable transistor properties have been reported in an indigo derivative, 5-5'-diphenyleindigo (μ_e = 0.95 and μ_h = 0.56 cm^2/Vs).[40] This compound has a unique hybrid molecular packing, where the phenyl groups form a herringbone structure and the indigo parts align as a brickwork structure. Many ambipolar semiconductors have been developed on the basis of indigo and DPP, while it should be mentioned that semiquinone species also show ambipolar transport.[41]

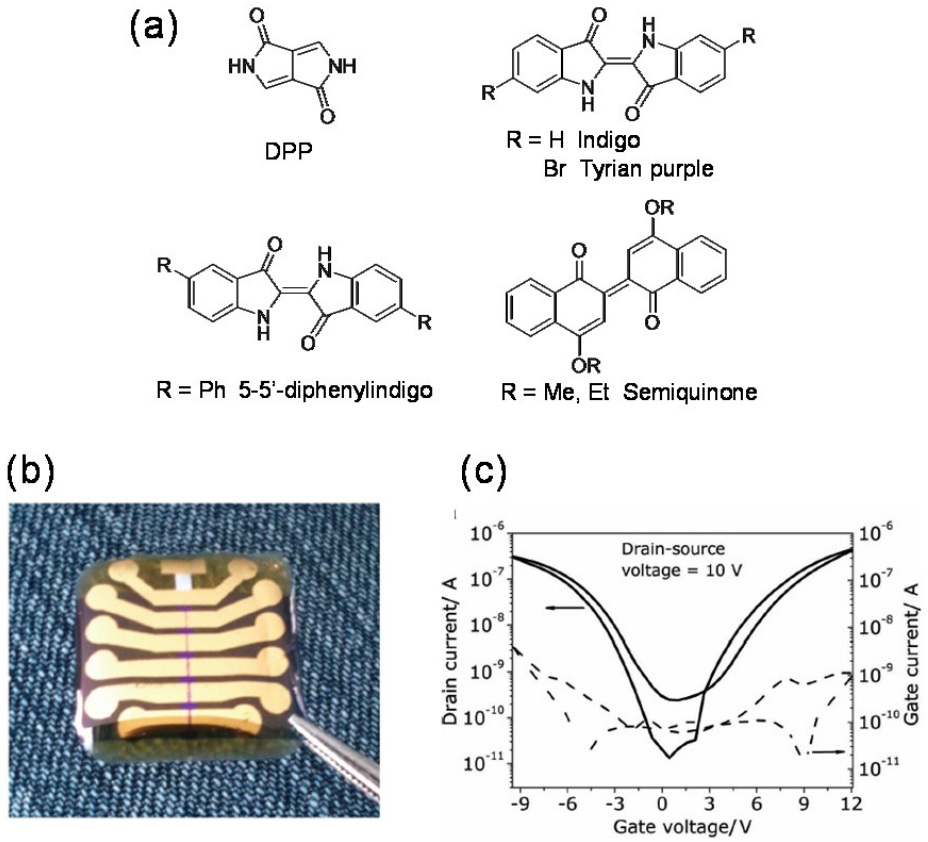

Figure 1-17. (a) Ambipolar organic semiconductors. (b) Optical image of an indigo transistor. (c) Transfer characteristics of ambipolar indigo thin-film transistors.[39]

1.7.5 Self-contact organic transistors using laser sintering

In general, organic compounds are transformed to conducting carbon by laser sintering. In this connection, organic thin-film transistors with carbon electrodes, where the organic semiconductors are selectively transformed to carbon by using laser sintering, have been developed.[42] This type of transistor is called "self-contact" organic transistors because electrode parts are constructed from an active layer. The resulting carbon film is practically transparent because the thickness is as thin as 60 nm; the transparent conducting film is interesting as a replacement of indium tin oxide (ITO). This method is also useful for fabrication of single-crystal transistors.

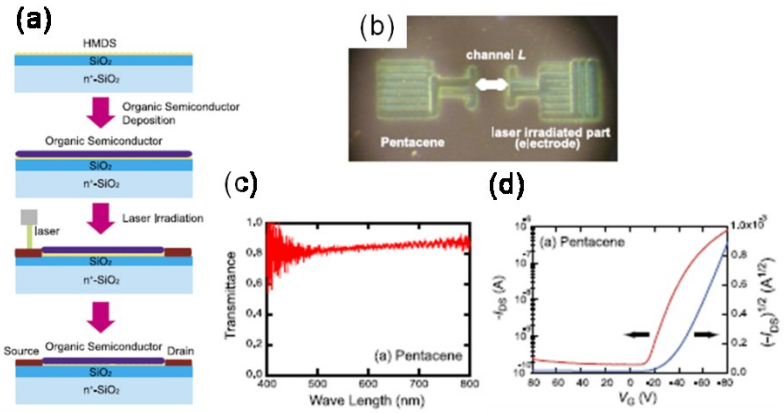

Figure 1-18. (a) Fabrication of self-contact organic transistors by laser sintering. (b) Optical image of self-contact organic transistors. (c) Transmittance of electrode parts. (d) Transfer characteristics of pentacene-based self-contact organic transistors.[42]

1.8 Organic CT salts in OFET

1.8.1 Charge-transfer salts as electrodes

It has been well known that bottom-contact (BC) transistors, in which organic semiconductors are deposited on the source and drain (S/D) electrodes, result in considerably reduced performance in comparison with top-contact (TC) transistors, where the S/D electrodes are formed on the thin films of organic semiconductors.[43,44] This has been attributed to (1) morphological discontinuity where organic semiconductor molecules are standing in the channel region but deposited in a face-on manner on the metal S/D electrodes (Figure 1-18)[43,44], and (2) interfacial potentials in which organic molecules at the metal/organic interface are usually charged in the direction to increase the injection barrier (Figure 1-19).[45–48]

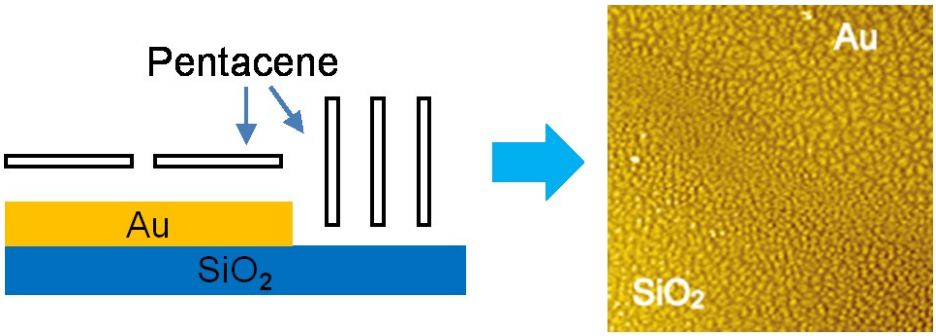

Figure 1-18. Schematic image of face-on and end-on arrangements, and AFM image of the morphological discontinuity area in a pentacene transistor.

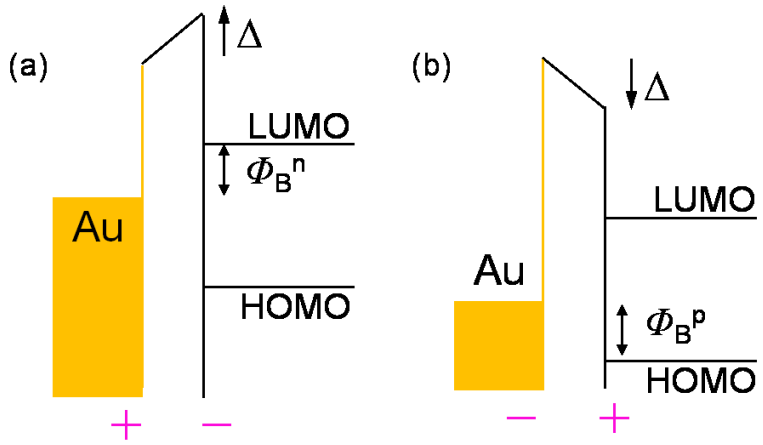

Figure 1-19. General interfacial energy diagram of (a) n-type and (b) p-type OFET.

To recover the performance of BC transistors, a buffer layer of oppositely charging molecules between the electrode and the active layer improves the performance. A thin layer of TCNQ deposited on Ag or Cu electrodes before evaporating active layer, works as a buffer layer and improves the performance.[49,50] However, metal TCNQ complexes are low-conducting.[51,52] Instead of TCNQ, when DMDCNQI is deposited from a solution between Ag or Cu electrodes and pentacene, the resulting mobility (0.3 cm^2/Vs) is nearly comparable to the Au TC transistors (0.49 cm^2/Vs).[53] This is related to the highly conducting metallic CT salt of $Cu(DMDCNQI)_2$.[54,55]

(TTF)(TCNQ) is also useful as electrodes. It has been reported that S/D electrodes made of (TTF)(TCNQ) result in drastic reduction of contact resistance and almost the same for BC and TC geometries, and comparable to the Au TC transistors (Figure 1-20 (a)).[44] This comes from the absence of morphological discontinuity at the organic/organic interface (Figure 1-20 (b)). It is a heart of this method that a two-component complex is easily vacuum deposited from a single crucible. In case of

(TTF)(TCNQ), the sublimation temperatures of the two components are very close to 120 °C. Therefore, this method is not applicable to other complexes such as cation- and anion-radical salts containing hardly evaporating counter ions. Similarly to this, recently Wada et al. have reported that conducting carbon instead of (TTF)(TCNQ) as electrodes exhibits excellent performance even in solution-processed BC transistors.[56] Inkjet printing of CT-salt electrodes from a solution of BO (bis(ethylenedioxy) tetrathiafulvalene) and alkyl-TCNQ complex has been achieved as well.[57]

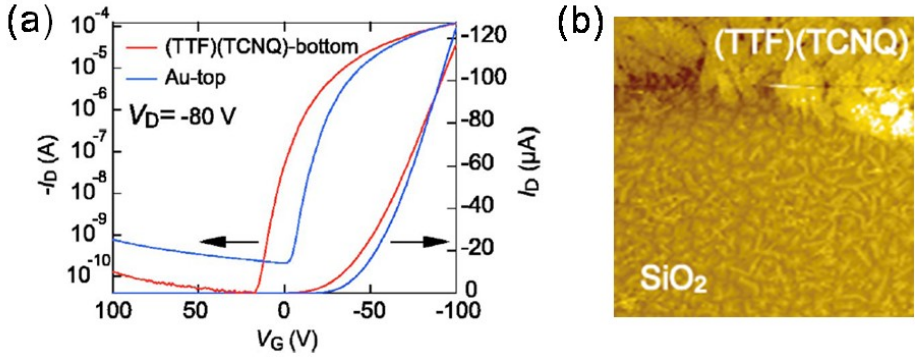

Figure 1-20. (a) Transfer characteristics of pentacene transistors with (TTF)(TCNQ)-bottom, and Au-top contact transistor. (b) AFM image near the channel-electrode boundary.[44]

1.8.2 Charge-carrier control based on CT salts

Attempts to use CT complexes as an active layer have been reported by Kudo et al, where OFET composed of stacked layers of TMTSF and TCNQ gives rise to interfacial CT.[58,59] Sakai et al. have achieved fabricating a short channel (400 nm in length) transistors of self-wired (TTF)(TCNQ).[60]

Takahashi et al. have reported electrodes composed of (TTF)(TCNQ)-type CT salts vacuum deposited on (DBTTF)(TCNQ) single crystals, and observed large n-type

mobility of 1.0 cm^2/Vs in air.[61] Furthermore, it has been achieved that the characteristics of (DBTTF)(TCNQ) transistors are controlled from hole, electron, and ambipolar transport with the use of chemically tuning the Fermi energy in (TTF)(TCNQ)-based CT-salt electrodes by changing TTF and TCNQ to similar molecules (Figure 1-21).[62]

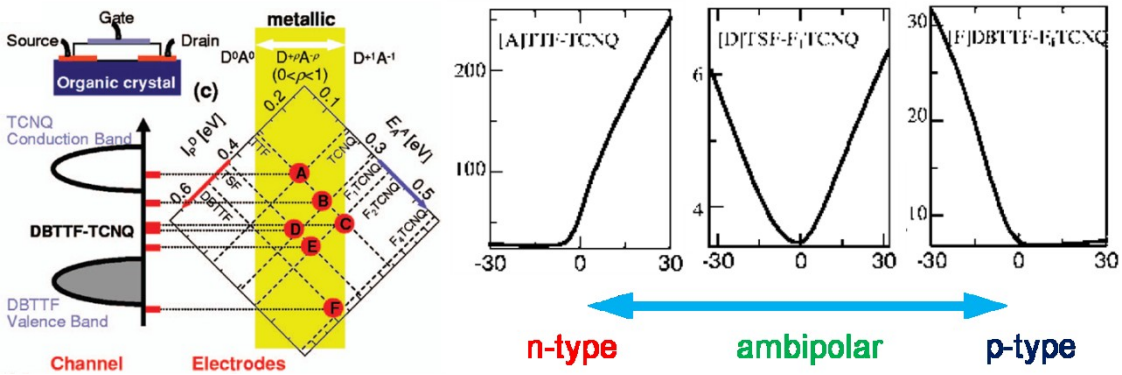

Figure 1-21. Energy diagrams of CT salts, and the transfer characteristics of (DBTTF)(TCNQ) transistors with CT-salt electrodes.[62]

1.8.3 Nanoparticles of organic CT complex in OFETs

Ionic liquid and some polymers such as poly(vinylpyrrolidone) (PVP) are useful to prepare nanoparticles of organic CT complexes.[63–65] This method gives a general way to obtain CT-complex films which are not vacuum evaporated. After nanoparticles of several CT complexes stabilized by PVP are prepared, conducting films are obtained by using the surface-selective deposition. Then organic semiconductors are vacuum evaporated. Surprisingly, not only holes but also electrons are efficiency injected from the radical-cation salts. The radical-anion salts also inject both of holes and electrons. This is convincing when we recognize these CT complexes as simple

metals. In general, the conductivity of radical-cation salts solely comes from the organic donors, in contrast, the organic acceptors attain the transport of radical-anion salts. Upon band formation, the Fermi energy is shifted by one quarter or one third of the bandwidth because of the partly-filled energy band. When the bandwidths of these CT complexes are about 0.8–1.0 eV, and when the band centers are unchanged from the original energy levels, the Fermi energy of the anion-radical salt is pushed down by about 0.2 eV, while that of the cation-radical salt is pushed up by about 0.2 eV. As a consequence, all the Fermi levels come to approximately 4.8 eV.[65] This is because the classical organic donors and acceptors have similar redox potentials.

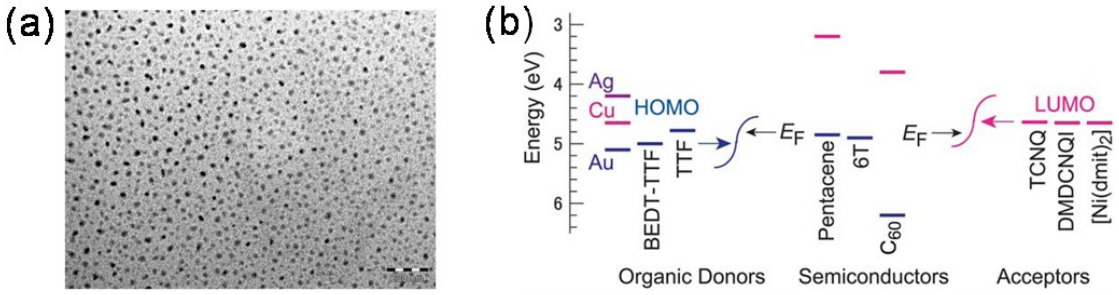

Figure 1-22. (a) SEM image of (TTF)(TCNQ) nanoparticles.[64] (b) Energy levels of organic donors, acceptors, semiconductors, and inorganic metals.[65]

1.8.4 Field-induced superconducting channel in OFETs

Superconductivity in a transistor channel has been reported by H. Y. Yamamoto et al.[66] The transistor uses a very thin single crystal of κ-(BEDT-TTF)$_2$Cu[N(CN)$_2$]Br (κ-Br salt), which exhibits a superconducting phase at 13 K. The κ-Br salt is laminated on a Nb-doped $SrTiO_3$ substrate covered with an Al_2O_3 dielectric layer. Then, the device is cooled down to low temperature. Due to the difference of the thermal expansion coefficient, the κ-Br salt is expanded and becomes not a

superconducting but a Mott insulating phase at low temperatures. Finally, the electric state is changed by applying the gate voltage and tunable from the Mott insulating to the superconducting phase.

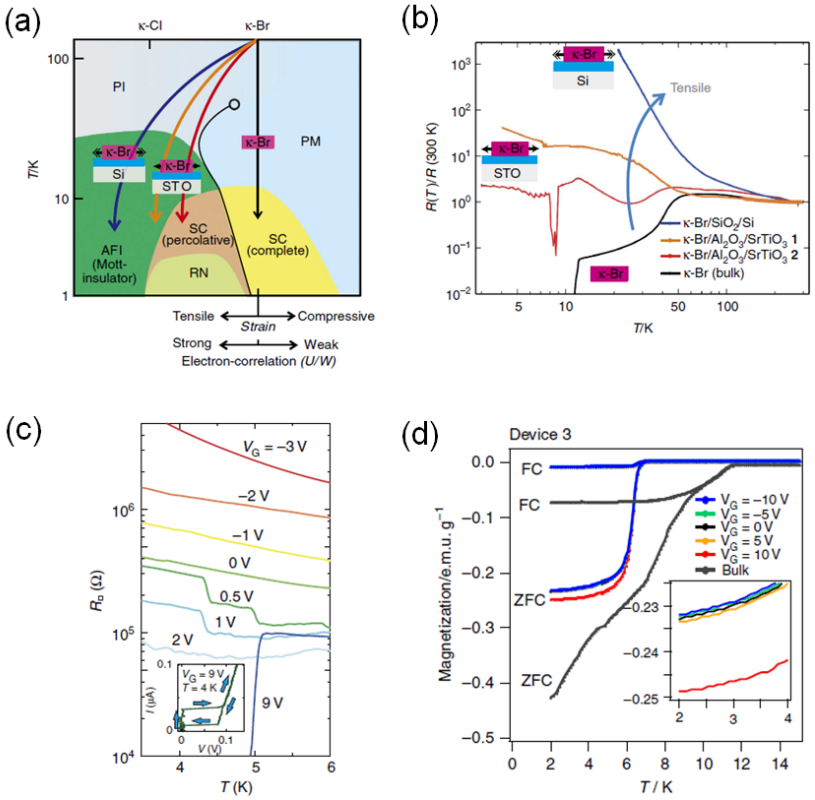

Figure 1-23. (a) Phase diagram of the κ-type BEDT-TTF system. (b) Temperature dependence of the relative resistance for κ-Br on SiO_2/Si (blue) and Al_2O_3/$SrTiO_3$ substrates (1 orange, 2 red), as well as that of the bulk crystal (black). (c) Temperature dependence of the resistance under various V_G in a logarithmic scale. The inset shows current (I)-voltage (V) characteristics at V_G = 9V and T = 4 K. (d) Magnetic susceptibility under various V_G (red, yellow, black, green and blue) along with that for bulk κ-Br (grey). FC and ZFC designate the measurements under field-cooled and zero-field-cooled conditions, respectively. The inset shows a magnified plot at the low-temperature region.[66]

1.9 Purpose and outline

Chemical doping is a conventional tool to realize conductivity in silicon technology but usually not used in organic electronics. This is partly because representative organic semiconductors do not form stable and high conducting materials. In this thesis, how to use chemical doping in organic transistors is investigated. The experimental details are shown in Chapter 2. Organic thin-film transistors with chemically-doped electrodes are described in Chapter 3, in which an organic acceptor 7,7,8,8-tetracyano-p-quinodimethane (TCNQ) is selectively vacuum deposited on an organic semiconductor tetramethyltetrathiafulvalene (TMTTF), and the resulting CT complex (TMTTF)(TCNQ) is used as the high conducting source and drain electrodes. In Chapter 4, inkjet-printed self-contact transistors are shown. Owing to the solution process, the CT complex which is not vacuum evaporated is capable to be applied to the self-contact technique. The resulting self-contact transistors attain satisfactory performance. Energy-level engineering at the electrode/semiconductor interface is also discussed. The self-contact technique based on chemical doping has a limitation that the single organic molecule has to work as the semiconductor layer and as the conducting electrodes. Therefore the highly conducting CT complex derived from an organic-transistor material is essential. In chapter 5, a highly conducting CT complex $(BTBT)_2PF_6$ is described. The structural, conducting, magnetic, and optical properties are investigated. It is remarkable that BTBT is a very weak electron donor, but forms the high conducting material. In chapter 6, access resistance of organic transistors on the basis of alkyl-substituted thienoacene is shown. Contact resistance comes from two kinds of contributions: the interface resistance (R_{int}) and the access resistance (R_{acc}). Although a considerable number of investigations have been devoted to reduce R_{int}, no

effective solution has been proposed to reduce R_{acc}. It is demonstrated that carbon electrodes are effective not only in interfacial morphological improvement but also in suppressing R_{acc}.

1.10 Reference

1 P. r. Wallace, *Phys. Rev.* **71**, 622 (1947).

2 H. Akamatu and H. Inokuchi, *J. Chem. Phys.* **18**, 810 (1950).

3 H. Akamatsu, H. Inokuchi, and Y. Matsunaga, *Nature* **173**, 168 (1954).

4 L.B. Coleman, M. J. Cohen, D. J. Sandman, F. J. Yamaguchi, A. F. Garito, A. J. Heeger, *Solid State Commun.* **12** 1125 (1973).

5 D. Jerome, A. Mazaud, M. Ribault, K. Bechgaasrd, *J. Phys. E.* **41**, L95 (1980).

6 H. Urayama, H. Yamochi, G. Saito, K. Nozawa, T. Sugano, M. Kinoshita, S. Sato, K. Oshima, A. Kawamota, and J. Tnaka, *Chem. Lett.* 55 (1988).

7 F. Sawano, I Terasaki, H. Mori, T. Mori, M. Watanabe, N. Ikeda, Y. Nogami, Y. Noda, *Nature* **437**, 522 (2005).

8 G. Saito and John. P. Ferraris., *Bull. Chem. Soc. Jpn.* **53**, 2141 (1980).

9 T. Mori and H. Inokuchi, *Solid State Commun.* **59**, 355 (1986).

10 H. Alives, A. S. Molinari, H. Xie and A. F. Morpurgo, *Nature Mater.* **7**, 574 (2008).

11 Y. Takahashi, K. Hayakawa, T. Naito, and T. Inabe, *J. Phys. Chem. C* **116**, 700 (2012).

12 J. E. Lilienfeld, US *patent* 1745175 (1925).

13 Z. Bao, J. Locklin ed., Organic Field-Effect Transistors; CRC Press, 2007

14 K. Kudo, M. Yamashita, and T. Morizumi, *Jpn. J. Appl.Phys.* **23**, 130 (1984).

15 T. Mori, *Chem. Lett.* **40**, 428 (2011).

16 H. Klauk, M. Z. U. Halik, G. Schmid, and W. Radlik, *J. Appl. Phys.* **92**, 5259 (2002).

17 (a) H. Minemawari, T. Yamada, H. Matsui, J. Tsutsumi, S. Haas, R. Chiba, R.

Kumai, and T. Hasegawa, *Nature* **475**, 364 (2011). (b) Y. Yuan1, G. Giri, A. L. Ayzner, A. P. Zoombelt, S. C. B. Mannsfeld, J. Chen, D. Nordlund, M. F. Toney, J. Huang1 and Z. Bao, *Nat. Commun.* **5**, 3005, (2014).

18 Y. Takahashi, T. Hasegawa, S. Horiuchi, R. Kumai, Y. Tokura, and G. Saito, *Chem. Mater.* **19**, 6382 (2007).

19 T. Yamada, R. Kumai, Y. Takahashi, and T. Hasegawa, *J. Mater. Chem.* **20**, 5810 (2010).

20 M. Mas-Torrent, P. Hadley, S. T. Bromely, N. Crivillers, J. Veciana, and C. Rovira, *Appl. Phys. Lett.* **86**, 012110 (2005).

21 T. Yamada, T. Hasegawa, M. Hiraoka, H. Matsui, Y. Tokura, and G. Saito, *Appl. Phys. Lett.* 92, 023305 (2008).

22 Z. Bao, A. J. Lovinger, and A. Doabalapur, *Appl. Phys. Lett.* **69**, 3066 (1996).

23 A. Dodabalapur, L. Torsi, and H. E. Katz, *Science* **268**, 270 (1995).

24 M. J. Kang, I. Doi, H. Mori, E. Miyazaki, K. Takimiya, M. Ikeda, H. Kuwabara, *Adv. Mater.* **23**, 1222 (2011).

25 T. Okamoto, C. Mitsui, M. Yamagishi, K. Nakahara, J. Soeda, Y. Hirose, K. Miwa, H. Sato, A. Yamano, T. Matsushita, T. Uemura, and J. Takeya, *Adv. Mater.* **25**, 6392 (2013).

26 C. Mitsui, T. Okamoto, M. Yamagishi, J. Tsurumi, K. Yoshimoto, K. Nakahara, J. Soeda, Y. Hirose, H. Sato, A. Yamano, T. Uemura, and J. Takeya, *Adv. Mater.* **26**, 4546 (2014).

27 G. R. Desiraju and A. Gavezzotti, *Acta Crystallogr., Sect. B* **45**, 473, (1989).

28 J. Idé, R. Méreau, L. Ducasse, F. Castest, Y. Olivier, N. Martinelli, J. Cornil, and D. Beljonne, *J. Phys. Chem. B* **115**, 5593 (2011).

29 Th.B.Singh, N.S.Sariciftci, H.Yang, L.Yang, B.Plochberger and H.Sitter, *Appl. Phys. Lett.* **90**, 213512 (2007).

30 A. R. Brown, D. M. de Leewuw, E. J. Lous, and E. E. Havinga, *Synth. Met.* **66**, 257 (1994).

31 Z. Bao, A. J. Lovinger, and J. Brpwn, *J. Am. Chem. Soc.* **120**, 207 (1998).

32 D. Shukla, S. F. Nelson, D. C. Freeman, M. Rajeswaran, W. G. Ahearn, D. M. Meyer, and J. T. Carey, *Chem. Mater.* **20**, 7486 (2008).

33 H. Wada, K. Shibata, Y. Bando, and T. Mori, *J. Mater. Chem.* **18**, 4165 (2008).

34 T.Takahashi, S. Tamura, Y. Akiyama, T.Kadoya, T. Kawamoto, and T.Mori, *Appl. Phys. Exp*. **5**, 061601 (2012).

34 D. M. de Leewuw, M. M. J. Simenon, A. R. Brown, and R. E. F. Einerhand, *Synth. Met.* **87**, 53 (1997).

35 Y. Yamaguchi, K. Ogawa, K. Nakayama, Y. Ohba, and H. Katagiri, *J. Am. Chem. Soc.* **135**, 19095 (2013).

36 L.-L. Chua, J. Zaumseil, J.-F. Chang, E. C.-W. Ou, P. K.-H. Ho, H. Sirringhaus, and R. H.Friend, *Nature* **434**, 194 (2005).

37 Y. Ito, A. A. Virkar, S. Mannsfeld, J. H. Oh, M. Toney, J. Locklin, and Z. Bao, *J.Am.Chem.Soc.* **131**, 9396 (2009).

38 S. Kobayashi, T. Nishikawa, T. Takenobu, S. Mori, T. Shimoda, T. Mitani, H. Shimotani, N. Yoshimoto, S. Ogawa, and Y. Iwasa, *Nature Mater.* **3**, 317 (2004).

39 M. I-. Vladu, E. D. Głowacki, P. A. Troshin, G. Schwabegger, L. Leonat, D. K. Susarova, O. Krystal, M. Ullah, Y. Kanbur, M. A. Bodea, V. F. Razumov, H. Sitter, S. Bauer, and N. S. Sariciftci, *Adv. Mater.* **24**, 375, (2012).

40 O. Pitayatanakul, T. Higashino, T. Kadoya, M. Tanaka, H. Kojima, M. Ashizawa,

T. Kawamoto, H. Matsumoto, K.Ishikawa, and T. Mori, *J. Mater. Chem. C* **2**, 9311 (2014).

41 T. Higashino, S. Kumeta, S. Tamura, Y. Ando, K. Ohmori, K. Suzuki, and T. Mori, *J. Mater. Chem. C* **3**, 1588 (2015).

42 J. Inoue, H. Wada, and T. Mori, *Jpn. J. Appl. Phys*. **49**, 071605 (2010).

43 C. D. Dimitrakopoulos, and P. R. L. Malenfant, *Adv. Mater.* **14**, 99 (2002).

44 K. Shibata, H. Wada, K. Ishikawa, H. Takezoe, and T. Mori, *Appl. Phys. Lett.* **90**, 193509 (2007).

45 H. Ishii, K. Seki, *IEEE Trans. Electron Devices* **44**, 1295 (1997).

46 H. Ishii, K. Sugiyama, D. Yoshimura, E. Ito, Y. Ouchi, and K. Seki, *IEEE J. Sel. Top. Quantum Electron.* **4**, 24 (1998).

47 I. G. Hill, A. Kahn, in Organic Light-Emitting Materials and Devices II (Proceedings of SPIE), ed. by Z. H. Kafafi, Vol. 3476, p. 168 (1998).

48 H. Ishii, K. Sugiyama, E. Ito, and K. Seki, *Adv. Mater.* **11**, 605 (1999).

49 C.-a. Di, G. Yu, Y. Liu, X. Xu, D. Wei, Y. Song, Y. Sun, Y. Wang, D. Zhu, J. Liu, X. Liu, and D. Wu, *J. Am. Chem. Soc.* **128**, 16418 (2006).

50 C.-a. Di, G. Yu, Y. Liu, Y. Guo, Y. Wang, W. Wu, and D. Zhu, *Adv. Mater.* **20**, 1286 (2008).

51 L. Shields, *J. Chem. Soc., Faraday Trans. 2* **81**, 1 (1985).

52 R. A. Heintz, H. Zhao, X. Ouyang, G. Grandinetti, J. Cowen, and K. R. Dunbar, *Inorg. Chem.* **38**, 144 (1999).

53 Y. Yu, M. Kanno, H. Wada, Y. Bando, M. Ashizawa, A.Tanioka, and T. Mori, *Phys. B* **405**, S378 (2010).

54 T. Mori, H. Inokuchi, A. Kobayashi, R. Kato, and H. Kobayashi, *Phys. Rev. B* **38**,

5913 (1988).

55 R. Kato, *Bull. Chem. Soc. Jpn.* **73**, 515 (2000).

56 H. Wada, and T. Mori, *Appl. Phys. Lett.* **93**, 213303 (2008).

57 M. Hiraoka, T. Hasegawa, Y. Abe, T. Yamada, Y. Tokura, H. Yamchi, G. Saito, T. Akutagawa, and T. Nakamura, *Appl. Phys. Lett.* **89**, 173504 (2006).

58 M. Iizuka, Y. Shiratori, S. Kuniyoshi, K. Kudo, and K. Tanaka, *Appl. Surf. Sci.* **130-132**, 914 (1998).

59 M. Iizuka, M.Nakamura, and K. Kudo, *Jpn. J. Appl. Phys.* **41**, 2720 (2002).

60 M. Sakai, M. Nakamura, and K. Kudo, *Appl. Phys. Lett.* **90**, 062101 (2007).

61 Y. Takahashi, T. Hasegawa, Y. Abe, Y. Tokura, K. Nishimura, and G. Saito, *Appl. Phys. Lett.* **86**, 063504 (2005).

62 Y. Takahashi, T. Hasegawa, Y. Abe, Y. Tokura, and G. Saito, *Appl. Phys. Lett.* **88**, 073504 (2006).

63 D. de Caro, K. Jacob, C. Faulmann, J.-P. Legros, F. Senocq, J. Fraxedas and L. Valade, *Synth. Met.* **160**, 1223 (2010).

64 D. de Caro, K. Jacob, H. Hahioui, C. Faulmann, L. Valade, T. Kadoya, T. Mori, J. Fraxedas, and L. Viau, *New J. Chem*. **35**, 1315 (2011).

65 T. Kadoya, D. de Caro, K. Jacob, C. Faulmann, L. Valade, and T. Mori, *J. Mater. Chem*. **21**, 18421 (2011).

66 H. M. Yamamoto, M. Nakano, M. Suda, Y. Iwasa, M. Kawasaki, and R. Kato, *Nat. Commun.* **4**, 2379, (2013).

Chapter 2

Experimental Section

2.1 Sublimation

Compounds used for an active layer in OFETs were purified by a vacuum sublimation system. Figure 2-1 shows a schematic image of the sublimation system. Source material was placed in the bottom of a short glass tube. The short glass tube was put into a long glass tube which was connected to a turbo molecular pump. Then the long glass tube was set in a heater. After being evacuated to 10^{-3} ~ 10^{-4} Pa, the bottom of the glass tube was heated up to an appropriate temperature. Some impurities sublimed below the sublimation temperature of the target material and deposited at an upper position of the short glass tube. If sublimation was conducted slowly enough, single crystals were obtained.

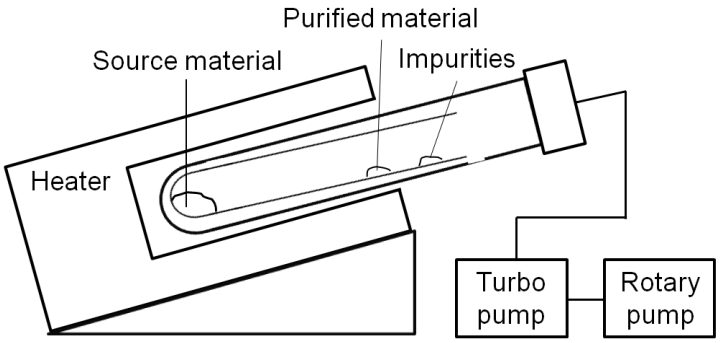

Figure 2-1. Schematic image of the sublimation system.

2.2 General device fabrication

Both top- and bottom-contact transistors were fabricated on heavily doped n^+-Si wafers with 300 nm thermally grown SiO_2. Before fabrication of the device, substrates were washed ultrasonically in acetone, 2-proparnol, and ultra pure water for 10 minutes, respectively. After dried, the substrates were irradiated by UV light (Technovision Model 208) to remove organic substances. As another method of cleaning, the substrates were immersed in piranha solution (70 vol % H_2SO_4 + 30 vol % H_2O_2) for 20 minutes at room temperature and washed with sufficient amounts of distilled water.

SAMs treatment was subsequently conducted after these processes. For hexamethylenedisilazane (HMDS) treatment, the substrates were put into a closed Teflon pod with a small vial containing a few millimeter depth of HMDS. The Teflon pod was annealed at 150 °C for 3 h in an ambient condition to expose the substrates to the HMDS vapor. After the treatment, the substrates were washed ultrasonically again in acetone for 20 minutes to remove excess HMDS. Octadecyltrimethoxysilane (OTMS) treatment was also conducted following the report.[1] 3 mM OTMS solution in trichloroethylene (12μl OTMS in 10ml trichloroethylene) was prepared. After cleaned

by a piranha solution, the OTMS solution was cast on the substrate, to cover the entire surface, and was allowed to partially self-assemble for 10 s. Then the substrate was spun at 3000 rpm for 10 s. In the same way as the HMDS treatment, the spin-casted substrate was put in a closed Teflon pod with a small vial containing a few millimeter depth of ammonia solution (30 % in water) for 24 - 48 h at room temperature. The substrate was then rinsed with distilled water and sonicated in toluene and acetone.

Metal electrodes were formed by vacuum deposition through a shadow mask in a small chamber in a vacuum of ~ 10^{-3} Pa. Organic thin films for an active layer were also fabricated by vacuum deposition. Organic compounds in an alumina crucible were thermally evaporated in a vacuum of 10^{-3} ~ 10^{-5} Pa. The schematic image of a vacuum evaporation chamber is shown in Figure 2-2.

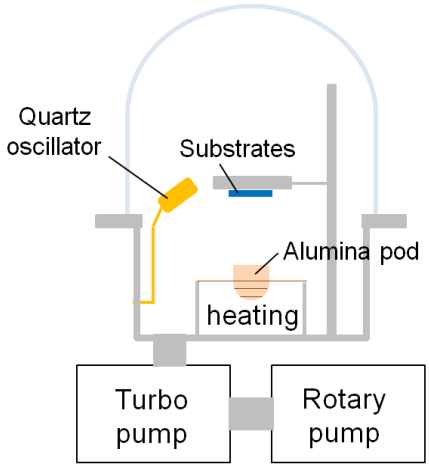

Figure 2-2. Schematic image of the vacuum-evaporation chamber.

2.3 Atomic force microscopy (AFM)

In order to investigate the films, AFM images were taken with an SII scanning probe microscope system SPI 3800N and SPA 300 by using an Si_3N_4 cantilever.

2.4 Scanning electron microscopy (SEM)

To investigate the films, SEM images were taken with a HITACHI FE-SEM S-4700.

2.5 Micro area X-ray diffraction (MAXRD)

Micro area X-ray diffraction analyses of the films were performed by Bruker AXS D8 DISCOVER μHR.

2.6 Raman spectroscopy

To investigate the electric state, raman spectrum was measured on a NRS-2100 spectrometer (Nihon Bunko).

2.7 Field-effect transistor characteristics

FET characteristics were measured by a Keithley 4200 semiconductor parameter analyzer. The measurements in air were carried out using an OYAMA manual prober system model TB-2-H-200. For the vacuum measurement, the substrate was transferred to a vacuum micro prober system. After transferred and set up, the vacuum prober system was evacuated to 10^{-3} Pa, and the transistor properties were measured.

Field-effect mobility (μ) was calculated from transfer characteristics in the saturation regime using the conventional equation,[2]

$$I_{D,sat} = \frac{\mu WC(V_G - V_{th})^2}{2L}$$

$I_{D,sat}$ was the saturated current, W was the channel width, L was the channel length, and C was the capacitance of the SiO_2 insulator per unit area (13 nF/cm^2). This equation was converted to the following equation,

$$\mu = \frac{2L}{W}\frac{(a)^2}{C}$$

where a was the gradient which is fitted to the V_G-$I_D^{1/2}$ plot in the transfer characteristics (Figure 2-3). The threshold voltage V_{th} was estimated from the intercept of this line.

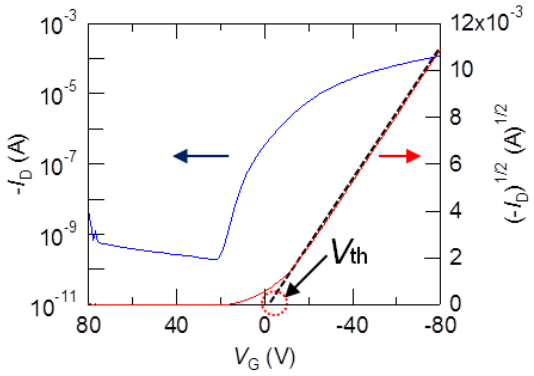

Figure 2-3. Estimation of μ and V_{th} from the transfer characteristics.

2.8 Transfer-line method

Contact resistance provides an indication of the carrier injection barrier between the S/D electrodes and organic semiconductor, so this is extracted by the transfer-line method (TLM). To estimate the contact resistance, the devices with different channel

lengths were prepared on the same substrate. The total resistance $R_T = \Delta V_D/\Delta I_D$ was plotted as a function of the channel lengths L (Figure 2-4). From the intersection at the channel length $L = 0$ μm, the contact resistance was extracted. The contact resistance was normalized as $R_C W$ because it was inversely proportional to W.

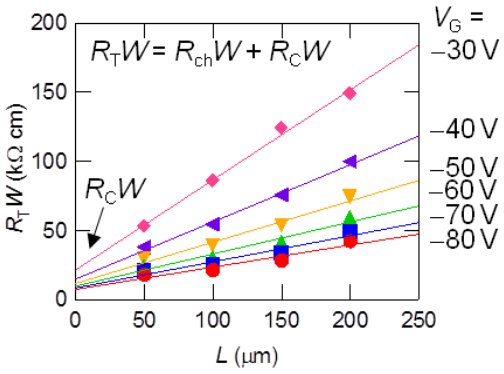

Figure 2-4. Analysis of contact resistance.

After the estimation of the contact resistance, the channel resistance is obtained as,

$$R_{ch} = \frac{L}{W\mu C(V_G - V_{th})} \qquad (\text{for } V_G - V_{th} >> V_D)$$

where μ is the channel mobility without including the contact resistance. Accordingly, L/R_{ch} is

$$\frac{L}{R_{ch}} = W\mu C(V_G - V_{th}) \qquad (\text{for } V_G - V_{th} >> V_D)$$

here $R_{ch}W/L$ corresponds to the gradient of the respective line in Figure 2.5, and the channel mobility is extracted from this relation.

2.9 Electrochemical oxidation

Single crystals of molecular conductors were prepared by the electrochemical oxidation. 5mg of organic donor and 16 ~ 20 mg supporting electrolyte were set in an H-type cell fitted with a glass filter. By applying a constant current of 0.5–5 μA under an Ar atmosphere for 2–3 days, electrochemical oxidation was performed in an organic solvent at room temperature.

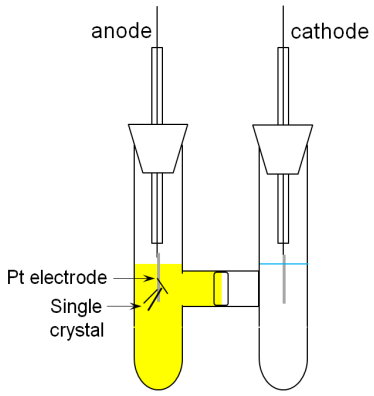

Figure 2-5. H-type cell for electrochemical oxidation.

2.10 Single-crystal X-ray structure analysis

The X-ray diffraction data were collected by using a Rigaku AFC-7R diffractometer with graphite monochromated Mo Kα radiation (0.71069 Å). Alternatively, X-ray photographs were taken on a Rigaku R-AXIS RAPID-II diffractometer using CuKα radiation (λ = 1.54187 Å) monochromated by confocal mirror (Rigaku VariMax). The crystal structures were solved by the direct method (SIR2008[3]) and refined by full-matrix least squares on F^2 (SHELXL-97[4]).

2.11 Resistivity measurement

The temperature dependence of the resistivity was measured by using a lock-in amplifier (Stanford Research Systems, SR830) by the four-probe method in order to eliminate the contact resistance (Figure 2-6 (a)). Gold wires (15 μm ϕ diameter) were attached to a crystal using carbon paste. Constant current was applied by converting the reference ac voltage to ac current by using a load resister. A frequency as low as about 13 Hz was used for the reference signal. For high-pressure measurements, a pressure cell of the clamp type was used with a Daphne #7373 oil as a pressure medium (Figure 2-6 (b)). The pressure was estimated from the resistance change of a manganin wire at room temperature.

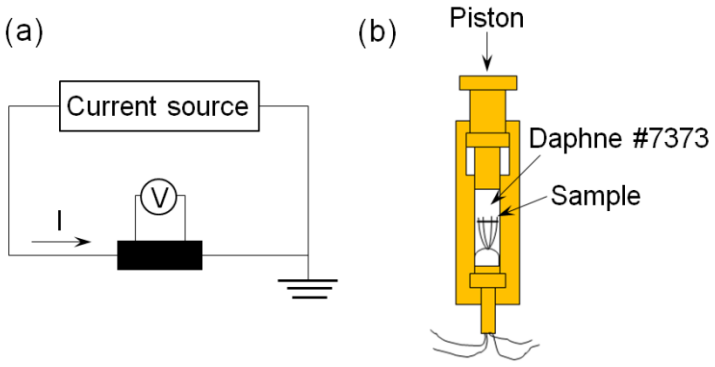

Figure 2-6. (a) Electric circuits used in the four-probe method and (b) the clamp cell.

2.12 Electron spin resonance (ESR)

The ESR measurements were carried out for single crystals by using an X-band spectrometer (JEOL JES-TE100). The *g* values were calibrated by the spectra of diphenyl-(2,4,6-trinitrophenyl)iminoazanium (DPPH): $g = 2.0036$, and Li(TCNQ): $g = 2.0026$. Since the signal of the present sample was very close to DPPH and Li(TCNQ), the signal was not measured at the same time. Calibration was performed as follows. First, the *g* value of the sample was measured without DPPH and Li(TCNQ). Second, the *g* values of DPPH or Li(TCNQ) were measured under nearly the same conditions, and the differences of the *g* values from the reported values were evaluated. Finally, the sample *g* value was corrected on the basis of the evaluated difference. The corrected *g* values coincided with each other up to five digits for DPPH and Li(TCNQ).

2.13 Redox potentials

Cyclic voltammograms (CVs) were measured by using ALS model 701E (BAS) in dichloromethane containing tetrabutylammonium hexafluorophospate as a supporting electrolyte at a scan speed of 0.1 V/s. Counter and working electrodes were made of Pt and glassy carbon, respectively, and the reference electrode was Ag/AgCl. The potentials were calibrated with the standard ferrocene/ferrocenium redox couple.

2.14 Reference

1 Y. Ito, A. A. Virkar, S. Mannsfeld, J. H. Oh, M. Toney, J. Locklin, and Z. Bao, *J. Am. Chem. Soc.* **131**, 9396 (2009).

2 C. D. Dimitrakopoulos and P. R. L. Malenfant, *Adv. Mater.* (Weinheim, Ger.), **14**, 99 (2002).

3 M. C. Burla, R. Caliandro, M. Camalli, B. Carrozzini, G. L. Cascarano, L. de Caro, C. Giacovazzo, G. Polidori, D. Siliqi, and R. Spagna, *J. Appl. Crystallogr.* **40**, 609 (2007).

4 G. M. Sheldrick, *Acta Crystallogr., Sect. A* **64**, 112 (2008).

Chapter 3

Self-Contact Organic Transistors Using Chemical Doping

3.1 Introduction

Chemical doping using such elements as boron and phosphorus is a conventional tool to construct a conductive part in usual silicon technology. In contrast, a similar chemical doping method has not been widely used in organic electronics, where single-component materials are used as organic semiconductors. This is related to the fact that representative and high-performance organic semiconductors including small molecules and polymers usually do not form stable and high-conducting complexes. Chemical doping has been, however, known for a long time as organic charge-transfer (CT) salts. Tetrathiafulvalene (TTF) and 7,7,8,8-tetracyano-*p*-quinodimethane (TCNQ) are respectively a traditional organic donor and an acceptor, and the combined organic CT complex, (TTF)(TCNQ), shows high conductivity. Similarly, other TTF derivatives form the conducting CT complexes with TCNQ.

Single crystals of TTF and TCNQ exhibit excellent transistor properties, while these small molecules ordinarily do not form good thin-film transistors due to the high vapor pressures. However, other TTF derivatives show excellent transistor characteristics in the thin films. Recently, we have reported that

tetramethyltetrathiafulvalene (TMTTF) forms good thin films and exhibits high transistor performance when evaporated under low vacuum. In addition, TMTTF also forms a high conducting CT complex with TCNQ. If the same organic molecule works not only as an active layer in organic transistors but also as electrodes by forming a conductive CT complex, we can construct organic transistors from a single material. A method has been developed, where organic semiconductor films are partly changed to conductive carbon by laser irradiation, and they are used as the electrodes of organic transistors. This type of transistor is called a "self-contact" organic transistor, because the electrodes are constructed from the same organic material as the active layer.

In this chapter, self-contact organic thin-film transistors with chemically doped electrodes are described. In this method, either vacuum deposition or solution process can be applied to construct conducting parts, but this chapter describes the vacuum deposition method because this method is comparatively simple due to the absence of the solvent effect. As the active layer, TMTTF is chosen, and TCNQ is the dopant. When TCNQ is vacuum evaporated on a TMTTF film, the conducting CT complex (TMTTF)(TCNQ) is formed. We have fabricated transistors with various electrodes in comparison with the self-contact transistor. Contact resistance and charge injection are discussed from the standpoint of the energy levels.

3.2 Experimental

Figure 3-1 shows the illustration of the self-contact transistors using chemical doping. TMTTF was purified by sublimation under the vacuum of 10^{-4} Pa. The typical sublimation temperature was 120°C for TMTTF. As a surface treatment, polystyrene ($\varepsilon = 2.5$ and 100 nm thickness) was spin-coated (3000 rpm for 30 s) from a 20 mg/ml toluene solution on a highly doped *n*-type silicon wafer with a thermally grown silicon dioxide layer of 300 nm thickness, where the resulting overall capacitance of the gate dielectrics was 9.0 nF/cm^2. TMTTF was evaporated under the vacuum of 10^{-3} Pa. The top-contact transistors were fabricated by evaporating Au, (TTF)(TCNQ), and (TMTTF)(TCNQ) through a metal mask (channel length L = 50-200 μm and channel width W = 1000 μm) under a similar order of low vacuum. The temperatures of the alumina crucibles were 130°C for (TTF)(TCNQ) and 100°C for (TMTTF)(TCNQ). (TTF)(TCNQ) and (TMTTF)(TCNQ) were prepared by mixing the hot acetonitrile solutions of the component molecules. The self-contact transistor was fabricated in a similar way by evaporating TCNQ at 95°C through a metal mask on a TMTTF film, followed by annealing at 80°C for 2 h under Ar atmosphere.

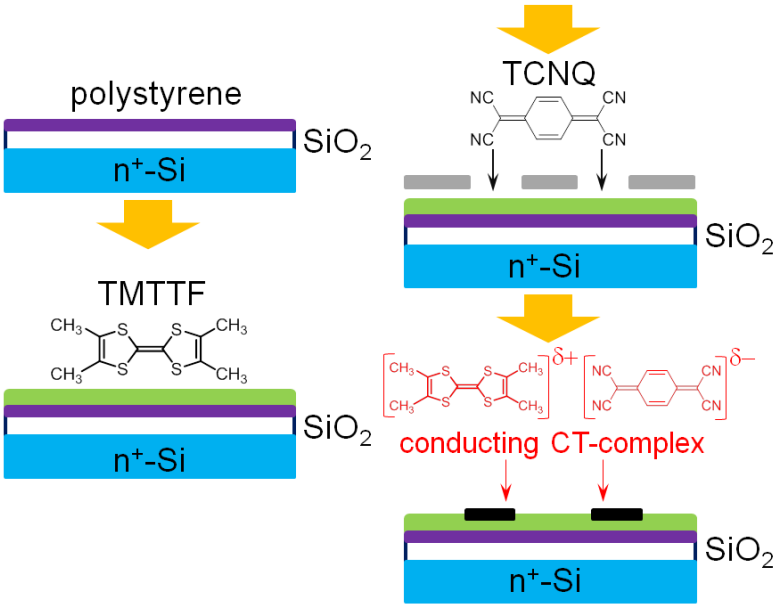

Figure 3-1. Schematic image of the self-contact organic transistors fabricated by vacuum deposition.

3.3 Thin-film properties

When TCNQ is vacuum deposited through a metal mask, the color of the TMTTF film darkens as shown in Figure 3-2(a) due to the formation of the CT complex. AFM images of the evaporated thin films are also shown in Figure 3-2. Thin films of TMTTF (Figure 3-2(b)) and TCNQ (Figure 3-2(c)) are composed of grains as large as 4 μm, while (TMTTF)(TCNQ) evaporated from a single crucible shows needle-like grains (Figure 3-2(d)). When TCNQ is evaporated on a TMTTF film, the resulting film (Figure 3-2(e)) is similar to the (TMTTF)(TCNQ) film (Figure 3-2(f)). It has been also reported that when BEDT-TTF is deposited on a TCNQ layer, after annealing, the crystals of the CT complex start to grow from the interface region and extend even above the BEDT-TTF layer.[23] Such a CT complex is expected to be conducting enough to work as source and drain (S/D) electrodes of a self-contact transistor.

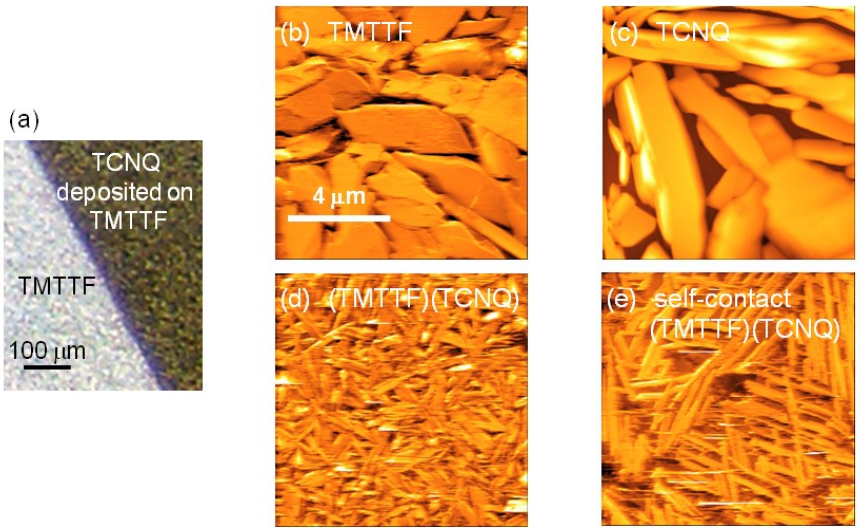

Figure 3-2. (a) Optical microscopic image of an interface of TMTTF and (TMTTF)(TCNQ). AFM images of (b) TMTTF, (c) TCNQ, and (d) (TMTTF)(TCNQ) films, together with (e) a TMTTF film after TCNQ evaporation.

The x-ray diffractions (XRD) of TMTTF, (TMTTF)(TCNQ), and TCNQ-deposited TMTTF films exhibit peaks approximately at the same positions of *d* = 6.3-6.5 Å (Figure 3-3(a)). Since the *d*-values of TMTTF and (TMTTF)(TCNQ) are approximately the same, we cannot distinguish these phases by using the XRD measurement. The thin-film phase of TMTTF is different from the single-crystal phase,[24,25] and the XRD of the present TMTTF film coincides with that of the reported thin-film phase,[24] where the molecular short axis of TMTTF is oriented perpendicular to the substrate (Figure 3-3(b)). This is neither the usual tail-on nor the face-on arrangement, but a "side-on" arrangement. In contrast to the present observation, the flat plane of the plate-like single-crystal phase is basically perpendicular to the molecular long axis (*c* = 7.8 Å).[25]

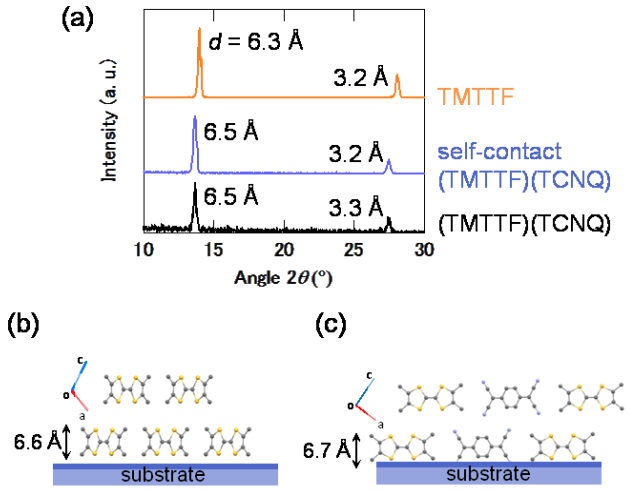

Figure 3-3. (a) X-ray diffraction patterns of TMTTF and (TMTTF)(TCNQ) and doped (TMTTF)(TCNQ) films. The expected molecular arrangements are depicted in the (b) TMTTF and (c) (TMTTF)(TCNQ).

In addition to the solution grown (TMTTF)(TCNQ),[18] $(TMTTF)_{1.3}(TCNQ)_2$ and $(TMTTF)_{1.66}(TCNQ)_2$ have been prepared from the vapor phase.[26,27] All these phases are composed of TMTTF and TCNQ columns, but since the TMTTF molecule is slightly longer than the TCNQ molecule along the molecular long axis, a coexisting layer of tail-on arrangement of TMTTF and TCNQ is impossible in contrast to (TTF)(TCNQ).[28] This is probably a reason that the tail-on geometry is not realized in (TMTTF)(TCNQ). Then misfit occurs along the molecular long axis, and the composition deviates from 1:1, so that TMTTF deficient phases are generated. If the molecular short axes, that are approximately the same for TMTTF and TCNQ, are perpendicular to the substrate, the coexisting layer is possible. Actually, $(\boldsymbol{a} - \boldsymbol{c})/4$ of (TMTTF)(TCNQ) crystal (Figure 3-3(c)) corresponds to the molecular short axes, which are also equal to the observed *d* value (6.7 Å) of the thin film.[19] We cannot exclude the possibility of the existence of $(TMTTF)_{1.3}(TCNQ)_2$ and $(TMTTF)_{1.66}(TCNQ)_2$, where the corresponding lattice constants are about the same,[26,27]

but we will simply designate the CT complex as (TMTTF)(TCNQ). The facile TCNQ doping is ascribed to such a side-on molecular arrangement, which is common to TMTTF and (TMTTF)(TCNQ) thin films.

3.4 Transistor characteristics

The transistor characteristics are shown in Figure 3-4. The maximum and average of the apparent mobilities are estimated together with the on-off ratio and the threshold voltage V_{th} as listed in Table 3-1. Organic transistors using CT salts exhibit higher performance than the ordinary Au transistors. Since the TMTTF film is formed only under relatively low vacuum, the evaporation of Au on the TMTTF film has been done under similar low vacuum. This may, however, give a slight damage on the TMTTF film. The (TTF)(TCNQ) film is fabricated at a comparatively low temperature, and this is, at least partly, the reason that the (TTF)(TCNQ) contact affords much improved performance. The mobility of the self-contact transistor is in the same order as the (TMTTF)(TCNQ) and (TTF)(TCNQ) top-contact transistors.

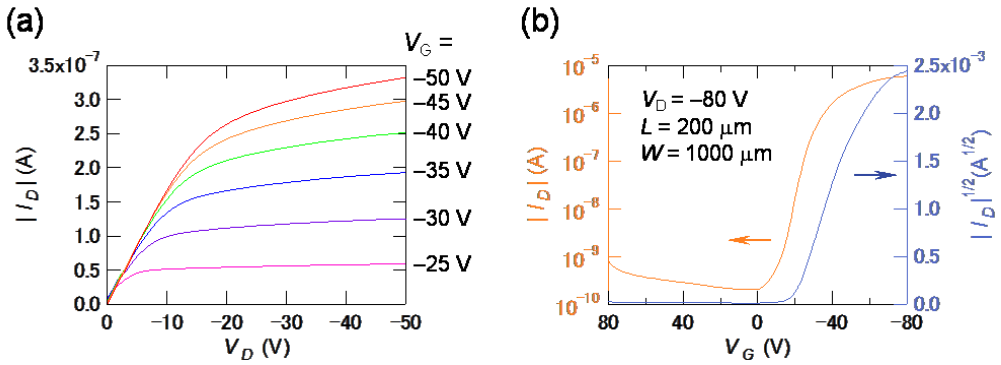

Figure 3-4. (a) Output, and (b) transfer characteristics of a self-contact transistor based on TMTTF.

Table 3-1. Maximum mobility μ_{max}, average mobility μ_{av}, on/off ratio, and threshold voltage V_{th} in TMTTF-based transistors.

Contact		μ_{max} (cm^2 / V s)	μ_{av} [a] (cm^2 / V s)	On/off [a]	V_{th} [a] (V)
Au	Top	0.11	0.053	3 x 10^4	–30
Au	Bottom	1.5 x 10^{-3}	2.5 x 10^{-4}	60	65
(TTF)(TCNQ)	Top	0.68	0.27	2 x 10^4	-13
(TMTTF)(TCNQ)	Top	0.39	0.11	1 x 10^4	–17
Self-contact (TMTTF)(TCNQ)	Top	0.53	0.14	4 x 10^4	–6.5

[a] μ_{av}, on/off ratio and V_{th} are average of 24 transistors.

Contact resistance R_cW is estimated from the transfer-line method in the linear region (Figure 3-5). These plots afford R_cW = 3600 kΩ cm for the Au top-contact transistors, whereas this value is reduced to R_cW = 200 kΩ cm for the (TTF)(TCNQ) transistor, and R_cW = 520 kΩ cm for the (TMTTF)(TCNQ) transistor. The self-contact transistor shows even lower contact resistance (R_cW = 80 kΩ cm), indicating the significantly reduced contact resistance at the organic/organic interface. The different gradients, however, indicate somewhat different mobilities in the channel region.

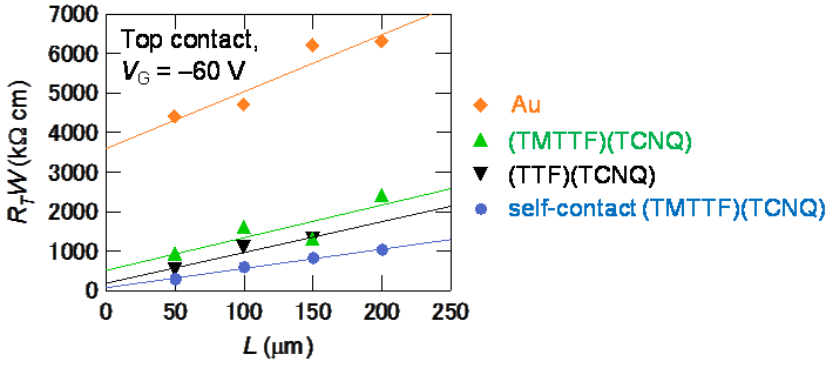

Figure 3-5. Channel length dependence of the total resistance R_T normalized with respect to the channel width W for the top-contact transistors.

(TMTTF)(TCNQ) is highly conducting,[19] and the sheet resistance of the evaporated (TMTTF)(TCNQ) film is 220 kΩ/□. However, the sheet resistance of the (TMTTF)(TCNQ) part in the self-contact transistor is as low as 50 kΩ/□. Since the film thicknesses of the (TMTTF)(TCNQ) film and the TCNQ-deposited TMTTF film are 65 and 200 nm, respectively, the conductivities are estimated to be σ = 0.7 and 1 S/cm. These values are not much smaller than 8 S/cm of the evaporated (TTF)(TCNQ) film, though the molecular arrangements are different.[6] Solution grown (TMTTF)(TCNQ) crystals show σ = 350 S/cm,[19] while $(TMTTF)_{1.3}(TCNQ)_2$ and $(TMTTF)_{1.66}(TCNQ)_2$ exhibit respectively high conductivities of σ = 50 and 10 S/cm as well.[26,27] High conductivity is expected even if there is some TMTTF deficiency. As shown in Fig. 4, the ionization potential of TMTTF (4.71 eV) is considerably different from the Au work function (5.1 eV), but are close to the Fermi levels of (TMTTF)(TCNQ) and (TTF)(TCNQ), which are expected to be located in between the highest occupied molecular orbital level of donors (4.78eV for TTF) and lowest unoccupied molecular orbital level of TCNQ (4.62 eV).[7,25,29] In general, more smooth hole injection is expected in the self-contact transistors, because the contact and the

active layer are composed of the same molecule. This is obvious from the remarkably low contact resistance.

3.5 Conclusion

In conclusion, we have investigated hole injection from several CT salts to TMTTF in organic transistors. When an organic molecule works as a good organic semiconductor, and forms highly conducting and stable CT salts at the same time, we can construct the self-contact transistors. As far as these conditions are fulfilled, the present technique is applicable to other materials including solution-processed materials, n-type semiconductors, and polymers. The present self-contact transistor has exhibited obviously higher performance than the ordinary transistors. This partly comes from the reduction of the heat damage at the time of evaporation for electrodes on the TMTTF films, but smooth carrier injection from the same kind of molecule is most important. In a sense, this is an organic analog of the conventional silicon technology, where chemical doping is extensively used for making the conducting part.

3.6 Reference

1 S. M. Sze, *Semiconductor Devices, Physics and Technology*, 2nd Ed. (John Wiley, New York, 2002).

2 Z. Bao and J. Locklin, *Organic Field-Effect Transistors* (CRC Press, New York, 2007).

3 T. Mori, *Chem. Lett.* **40**, 428 (2011).

4 L. B. Coleman, M. J. Cohen, D. J. Sandman, F. G. Yamagishi, A. F. Garito, and A. J. Heeger, *Solid State Commun.* **12**, 1125 (1973).

5 Y. Takahashi, T. Hasegawa, Y. Abe, Y. Tokura, K. Nishimura, and G. Saito, *Appl. Phys. Lett.* **86**, 063504 (2005).

6 K. Shibata, H. Wada, K. Ishikawa, H. Takezoe, and T. Mori, *Appl. Phys. Lett.* **90**, 193509 (2007).

7 T. Kadoya, D. de Caro, K. Jakob, C. Faulmann, L. Valade, and T. Mori, *J. Mater. Chem.* **21**, 18421 (2011).

8 R. Pfattner, M. M.-Torrent, C. Moreno, J. Puigdollers, R. Aleubilla, I. Bilotti, E. Venuti, A. Brillante, V. Laukhin, J. Vesiana, and C. Rovira, *J. Mater. Chem.* **22**, 16011 (2012).

9 H. Alves, A. S. Molinari, H. Xie, and A. F. Morpurgo, *Nat. Mater.* **7**, 574 (2008).

10 Y. Takahashi, Y. Nakagawa, K. Hayakawa, T. Inabe, and T. Naito, *Appl. Phys. Lett.* **101**, 103303 (2012).

11 H. Jiang, X. Yang, Z. Cui, Y. Liu, H. Li, W. Hu, Y. Liu, and D. Zhu, *Appl. Phys. Lett.* **91**, 123505 (2007).

12 E. Menard, V. Podzorov, S.-H. Hur, A. Gaur, M. E. Gershenson, and J. A. Rogers, *Adv. Mater.* **16**, 2097 (2004).

13 M. Yamagishi, Y. Tominari, T. Uemura, and J. Takaya, *Appl. Phys. Lett.* **94**, 053305 (2009).

14 A. R. Brown, D. M. de Leeuw, E. J. Lous, and E. E. Havinga, *Synth. Met.* **66**, 257 (1994).

15 M. Sakai, M. Izuoka, M. Nakamura, and K. Kudo, *J. Appl. Phys.* **97**, 053509 (2005).

16 T. Takahashi, S. Tamura, Y. Akiyama, T. Kadoya, T. Kawamoto, and T. Mori, *Appl. Phys. Express* **5**, 061601 (2012).

17 T. Kato, C. Origuchi, M. Shinoda, and C. Adachi, *Jpn. J. Appl. Phys.* **50**, 050202 (2011).

18 J. Inoue, H. Wada, and T. Mori, *Jpn. J. Appl. Phys.* **49**, 071605 (2010).

19 T. E. Phillips, T. J. Kistenmacher, A. N. Bloch, J. P. Ferrari, and D. O. Cowan, *Acta Crystallogr. Sect. B* **33**, 422 (1977).

20 M.-H. Yoon, H. Yan, A. Facchetti, and T. J. Marks, *J. Am. Chem. Soc.* **127**, 10388 (2005).

21 K.-J. Baeg, Y.-Y. Noh, J. Ghim, B. Lim, and D.-Y. Kim, *Adv. Funct. Mater.* **18**, 3678 (2008).

22 J. P. Ferraris, T. O. Poehler, A. N. Bloch, and D. O. Cowan, *Tetrahedron Lett.* **14**, 2553 (1973).

23 V. Solovyeva, K. Keller, and M. Huth, *Thin Solid Films* **517**, 6671 (2009).

24 S. Molas, J. Caro, J. Santiso, A. Figueras, J. Fraxedas, C. Meziere, M. Fourmigue, and P. Batail, *J. Cryst. Growth* **218**, 399 (2000).

25 A. S. Batsanov, M. R. Bryce, A. Chesney, J. A. K. Howard, D. E. John, A. J. Moore, C. L. Wood, H. Gershtenman, J. Y. Becker, V. Y. Khodorkovsky, A. Ellern, J. Bernstein, I. F. Perepichka, V. Rotello, M. Gray, and A. O. Cuello, *J. Mater. Chem.*

11, 2181 (2001).

26 T. J. Kistenmacher, T. E. Phillips, D. O. Cowan, John. P. Ferrarist, and A. Bloch, *Acta Crystallogr. Sect. B* **32**, 539 (1976).

27 E. Ehewnfreund, S. K. Khanna, A. F. Garito, and A. J. Heeger, *Solid State Commun.* **22**, 139 (1977).

28 T. J. Kistenmacher, T. E. Phillips, and D. O. Cowan, *Acta Crystallogr. Sect. B* **30**, 763 (1974).

29 Y. Takahashi, T. Hasegawa, Y. Abe, Y. Tokura, and G. Saito, *Appl. Phys. Lett.* **88**, 073504 (2006).

Chapter 4

Inkjet-Printed Self-Contact Organic Transistors

4.1 Introduction

Chemical doping is a conventional tool to construct a conducting part in silicon technology but usually not used in organic devices. In general, p-channel and n-channel organic semiconductors are regarded as an electron donor and an electron acceptor, respectively, and these molecules potentially constitute conducting CT complexes with various counter ions. However, organic semiconductors are basically used as an intrinsic form, *namely* as a single-component material, and this is one of the most important characteristics of organic electronic devices. This is partly because representative organic semiconductors do not form stable and highly conducting charge-transfer (CT) complexes.

In organic transistors, active layers are also composed of single-component organic semiconductors, whereas the performance is not solely governed by the inherent properties of the organic semiconductors, but largely influenced by the contact effect between the metal electrode and the organic active layer. In order to reduce the contact resistance, there are several remedies such as insertion of a buffer layer,[1–5] and thiol treatment of the Au electrode.[6,7] In this connection, conducting organic CT complexes

have been used as the electrode material, and proved to significantly reduce the contact resistance.[8–12] Recently, solution-processible silver and gold nanoparticles have been used widely, and the channel length as small as 4.5 μm has been achieved by the use of laser ablation and sintering.[13–16] Analogously, carbon electrodes fabricated by laser sintering have achieved low contact resistance together with high resolution and transparency.[17] Since laser sintering converts many organic compounds to conducting carbon, organic transistors are constructed by selectively transforming thin films of organic semiconductors to conducting carbon by laser irradiation.[18] Such devices are called "self-contact" organic transistors, because the contact part originates in the organic semiconductor. This is an ultimately easy way to fabricate organic transistors because the active layer and the source/drain (S/D) contacts are both made from a single organic film. However, this method is not applicable to a flexible organic substrate because the laser process damages the substrate.

As shown in chapter 3, I have recently developed another type of self-contact organic transistors by selectively transforming tetramethyltetrathiafulvalene (TMTTF) to a conducting CT complex by evaporating 7,7,8,8-tetracyano-*p*-quinodimethane (TCNQ).[19] Here TMTTF works as an excellent p-channel organic semiconductor, whereas (TMTTF)(TCNQ) is a highly conducting organic metal. By using (TMTTF)(TCNQ) as the electrode, smooth carrier injection is realized from the electrode to the active layer TMTTF.

In the present chapter, self-contact organic transistors are fabricated using a solution process, *namely* inkjet printing a solution of counter ions. Inkjet printing has attracted considerable attention as a low-cost, large area, and highly selective patterning tool for organic electronics.[20–26] In addition to my previous p-channel transistors, I

have achieved n-channel transistors. Figure 4-1(a) illustrates self-contact organic transistors using inkjet printing.

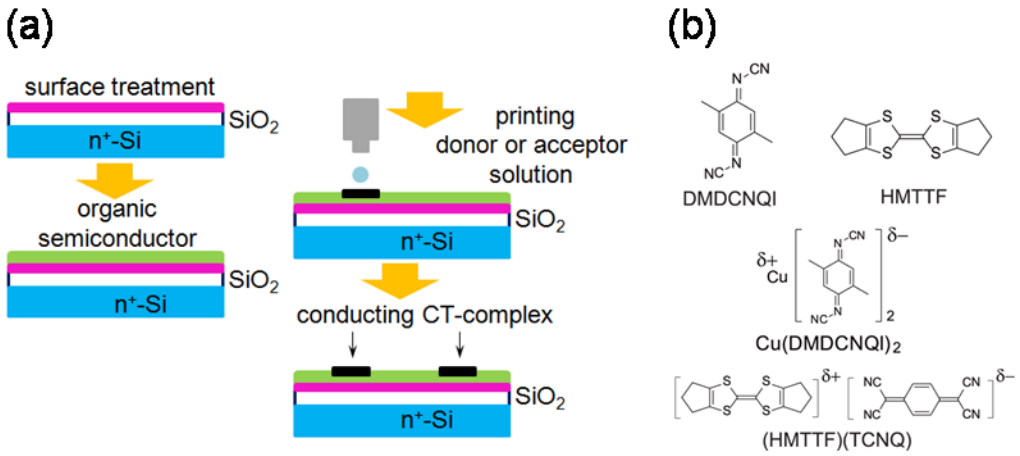

Figure 4-1. (a) Schematic image of self-contact organic transistors fabricated by inkjet printing. (b) Component molecules of organic semiconductors and conductors.

Here, dimethyldicyanoquinonediimine (DMDCNQI) is used as an n-channel material[27,28] and hexamethylenetetrathiafulvalene (HMTTF) as a p-channel organic semiconductor (Figure 4-1(b)).[29,30,32] First, an organic semiconductor film of DMDCNQI or HMTTF is vacuum evaporated on the substrate. Then a CuI or TCNQ solution is selectively printed on the semiconductor film. DMDCNQI is reduced by the CuI solution to the highly conducting complex, $Cu(DMDCNQI)_2$, according to the following reaction.[33]

$$2DMDCNQI + CuI \rightarrow Cu(DMDCNQI)_2 + 1/2\ I_2$$

HMTTF is also converted to the TCNQ complex.[32,34] After the conducting CT complexes are formed, these parts are used as the S/D electrodes in an organic transistor. Advantages of these self-contact transistors are discussed from the viewpoint of the energy-level engineering.

4.2 Experimental

DMDCNQI/Cu(DMDCNQI)$_2$ transistors

Transistors were fabricated onto an n-doped Si substrate with a thermally grown SiO_2 dielectric layer (300 nm, C = 13 nF cm^{-2}). DMDCNQI was purified by sublimation.[27] After octadecyltrimethoxysilane treatment,[35] DMDCNQI was vacuum evaporated under the vacuum of 10^{-3} Pa.[28] The film thickness of DMDCNQI was about 500–600 nm. A 1 wt% CuI solution of dehydrated acetonitrile (AN)/dimethylsulfoxide (DMSO) (volume ratio = 1:1 to 1:2) was ejected on the DMDCNQI film with a velocity of ~ 4 m s^{-1} (Figure 2a) using a piezoelectric inkjet printer head (Microjet JHB-1000). In the typical pattering method, the dots were successively deposited with an interval of 100 μm. After 15 min, the CuI printing was repeated in the reverse direction (Figure 4-2).

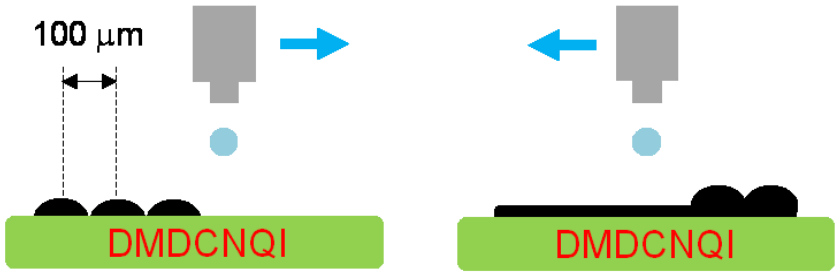

Figure 4-2. Patterning process of CuI solution on DMDCNQI films.

The electrode pattern had a width of about 150 μm. The channel width W = 950 - 1000 μm and length L = 100 - 200 μm were measured by an optical microscope (Figure 2c). Channel length was defined at the minimum; this method does not overestimate the mobility. The remaining solvent and iodine were removed by evacuation in a desiccator (≅1 Pa) over a period of 12 h. The transistor characteristics were measured at first in vacuum (10^{-3} Pa), then in the ambient conditions by using a

Keithley 4200 semiconductor parameter analyzer. The mobility was evaluated in the saturated region. Sheet resistance of the resulting self-contact region is measured by the two-probe method. Micro area X-ray diffraction (MAXRD) measurements of the thin films were carried out by Bruker AXS D8 DISCOVER μHR. Atomic force microscopy (AFM) images were obtained with a Seiko Instruments SPA-300 and SPI3800 probe system by using an Si_3N_4 cantilever. Electrode thickness profiles were measured by KOSAKA ET-200. Scanning electron microscopy (SEM) images were taken with a HITACHI FE-SEM S-4700.

HMTTF/(HMTTF)(TCNQ) transistors

HMTTF transistors were prepared similarly to the DMDCNQI transistors. As for the surface treatment, polystylene (ε = 2.5 and 100 nm) in toluene was spin-coated, where the resulting total capacitance of the gate dielectrics was 9.0 nF cm^{-2}.[19] HMTTF was purified by sublimation and vacuum evaporated up to the thickness of about 200 nm under 10^{-3} Pa. A 0.5 wt% TCNQ solution in 1:1 AN and DMSO was ejected repeatedly as following. The initial dots were deposited with an interval of 100 μm, and then these dots are interconnected by the second deposition (W = 700-800 μm and L = 100 - 200 μm, Figure 4-3), then annealed at 60 °C for 12 h in vacuum (10^{-3} Pa).

As another way, a 0.5 wt% TCNQ solution in 1:2 chlorobenzene (CB) and DMSO was used. Then, the substrate was dried in vacuum (≅1 Pa) over the period of 12 h. Raman spectra were recorded on a JASCO NRS-2100 spectrometer. For comparison, ordinary Au-top-contact transistors were fabricated. The resulting transistor characteristics were measured similarly to the DMDCNQI transistors.

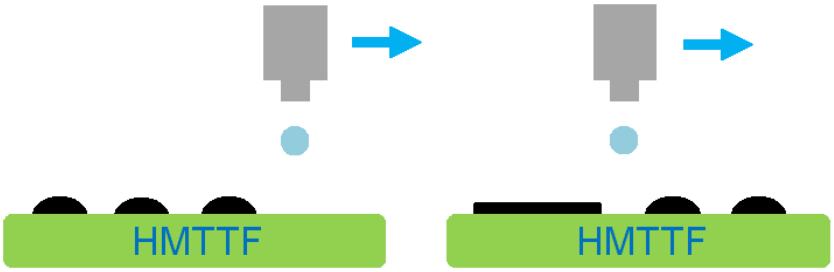

Figure 4-3. Patterning process of a TCNQ solution on HMTTF films.

4.3 Thin-film properties

Micro area X-ray diffraction (MAXRD) patterns are shown in Figure 4-4(a). The observed *d*-value of 8.1 Å corresponds to half the crystallographic *a* axis of the DMDCNQI single crystal.[36] The DMDCNQI molecular planes are standing perpendicular to the substrate, and forming a two-dimensional brickwork structure. The atomic force microscopy (AFM) images in Figure 4-4(b) shows block-like grains of the DMDCNQI film. In the electrode region (Figure 4-4(c)), additional peaks are observed in the MAXRD; the *d*-value of 10.8 Å corresponds to the crystallographic *a* axis of the single-crystal $Cu(DMDCNQI)_2$.[37] In Figure 4-4(d), the surface of $Cu(DMDCNQI)_2$ is not so smooth, and needle-like crystals are observed. From these results, formation of $Cu(DMDCNQI)_2$ on the DMDCNQI film is confirmed.

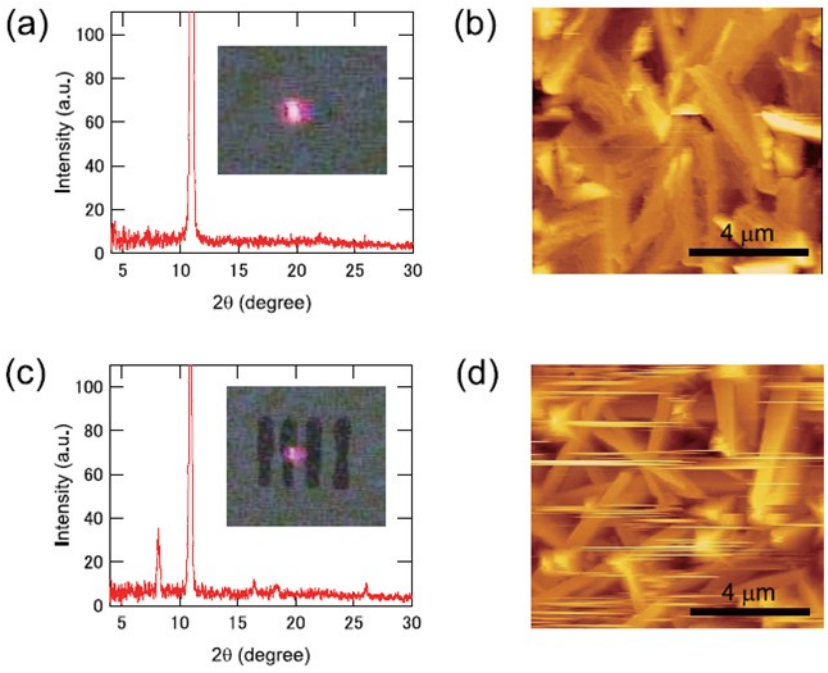

Figure 4-4. (a) MAXRD pattern and (b) AFM image of the DMDCNQI film. (c) MAXRD pattern and (d) AFM image of the $Cu(DMDCNQI)_2$ region after printing a 1 wt% CuI solution of 1:1 AN/ DMSO three times. The insets of (a) and (c) show the optical images of the sample, where the bright spots are X-ray irradiated regions.

The solvent of the ink is important for patterning the CT complex. It has been known that high boiling point and large surface energy are essential for the ink solvent.[38] In case of the DMDCNQI transistors, when CuI is dissolved in pure AN, the ejected droplets spread widely on the substrate and the patterning is not successful. On the other hand, when the ratio of DMSO is too large, the reaction is very sluggish, and conductivity of the electrode is low. The optimal ratio is AN/DMSO = 1:1 to 1:2. DMDCNQI readily reacts with CuI to form the complex, and we can use the device after drying the solvent. At the same time, the formed iodine is removed completely. The rapid reaction is partly because DMDCNQI dissolves in the ink-jet solvent, AN.

(HMTTF)(TCNQ) does not show clear XRD peaks, but the formation of the CT

complex is confirmed by Raman spectroscopy.[31] Figure 4-5 shows Raman spectra of HMTTF and (HMTTF)(TCNQ) films. The neutral HMTTF film shows a ν_3 C = C stretching mode at 1541 cm^{-1}.[39] After ink-jet printing, this peak shifts to a lower wave number owing to the complex formation. As a result, new peaks appear at 1459 and 1551 cm^{-1}, corresponding to the ν_3 and ν_2 modes of the C = C stretching of HMTTF, as well as at 1413 and 1606 cm^{-1} according to the ν_4 and ν_3 modes of the C = C stretching of TCNQ in (HMTTF)(TCNQ).[39]

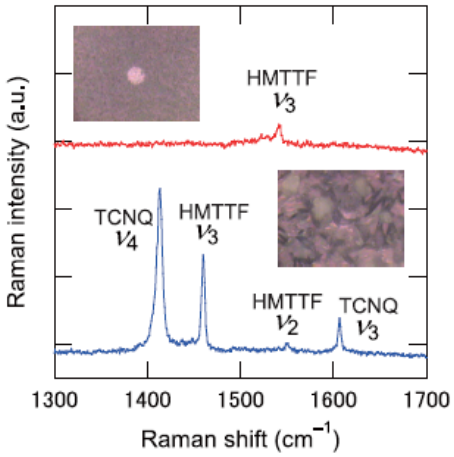

Figure 4-5. Raman spectra of an HMTTF self-contact transistor. The red curve corresponds to the neutral HMTTF film and the blue curve is from the (HMTTF)(TCNQ) region. The insets show the optical images of the HMTTF and (HMTTF)(TCNQ) regions, where the bright spot of the former is the laser irradiated region.

Figure 4-6(a) demonstrates that the sheet resistance R_s decreases with increasing the printing times N. Height profiles are shown in Figures 4-6(b) and 4-6(c). After repeated printing, the plateaus of the electrode parts become gradually clear. The initial printing leads to unlinked regions, but additional printing improves the connectivity within the electrode. The reaction of HMTTF does not proceed smoothly owing to the low solubility in the ink-jet solvent, to which the relatively high R_s and no

XRD peaks are attributed. In this case, annealing is necessary to attain the sufficient complex formation.

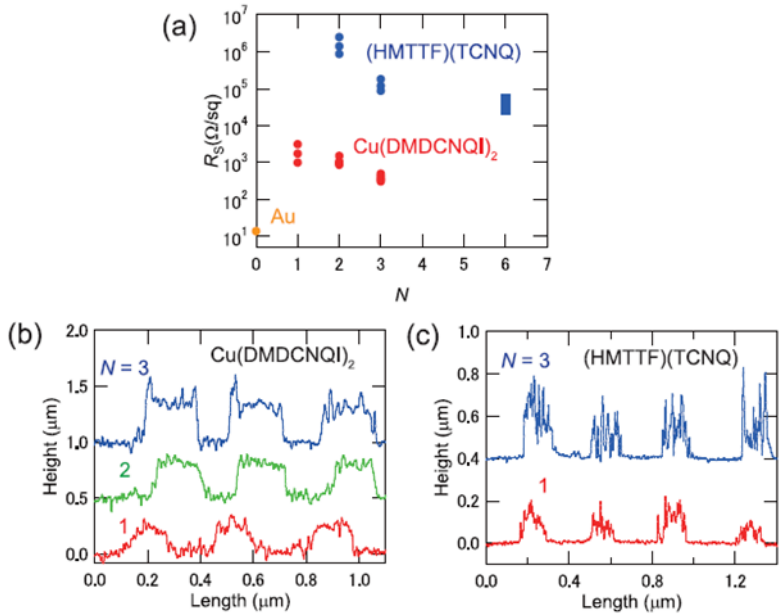

Figure 4-6. (a) Sheet resistance of electrodes as a function of printing times. The red circles for $Cu(DMDCNQI)_2$, blue circles for (HMTTF)(TCNQ) from AN/DMSO, blue squares for (HMTTF)(TCNQ) from CB/DMSO, and the orange circle for an Au film. Height profiles of (b) $Cu(DMDCNQI)_2$ and (c) (HMTTF)(TCNQ) films after the repeated inkjet printing.

4.4 Transistor characteristics

Transistor characteristics are shown in Figure 4-6 and Table 1. The self-contact transistors show as high performance as the ordinary Au-top-contact transistors. In particular, the printed HMTTF self-contact transistors realize excellent mobilities μ around 1 $cm^2\ V^{-1}\ s^{-1}$ together with the small threshold voltage, V_{th}, and the small hysteresis. It is noteworthy that these transistors exhibit excellent performance even in air similarly to in vacuum (Table 1).

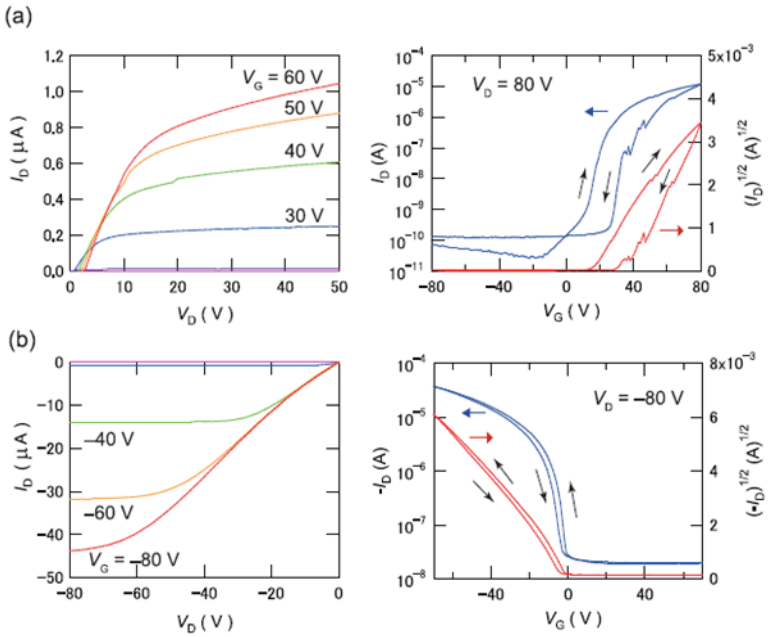

Figure 4-7. Output and transfer characteristics of self-contact organic transistors measured in vacuum. (a) DMDCNQI and (b) HMTTF.

Table 1. Transistor characteristics of DMDCNQI and HMTTF transistors.

Active layer	Contact	Solvent[a]	Condition	μ (cm^2V^{-1} s^{-1})	V_{th} (V)	on/off	$R_C W^{a,b}$ (kΩ cm)
DMDCNQI	Au TC		vacuum	0.045–0.1	16 – 28	89 – 400 x 10^3	130 (60 V)
			air	0.043–0.1	12 – 41	7 – 200 x 10^3	
	$Cu(DMDCNQI)_2$	AN/DMSO	vacuum	0.048–0.078	4 – 25	40 – 350 x 10^3	235 (60 V)
		(N = 2)					
HMTTF	Au TC		vacuum	0.75 – 0.94	–7 – 0	4 – 9.4 x 10^3	3 (–80 V)
			air	0.82 – 1.76	–4 – +3	0.2 – 1.6 x 10^3	
	(HMTTF)(TCNQ)	AN/DMSO	vacuum	0.46 – 1.0	–11 – 0	0.7 – 1.4 x 10^3	6 (–80 V)
		(N = 3)	air	0.6 – 1.6	–9 – +8	0.1 – 0.5 x 10^3	
		AN/DMSO	vacuum	0.8 – 1.1	–14 – –12	0.4 – 0.5 x 10^3	7 (–80 V)
		(N = 4)					
		CB/DMSO	vacuum	0.8 – 0.9	–6 – +3	0.3 – 1 x 10^3	28 (–80 V, N = 4)
		(N = 2)	air	1.2 – 1.9	–2 – +8	0.2 – 0.3 x 10^3	

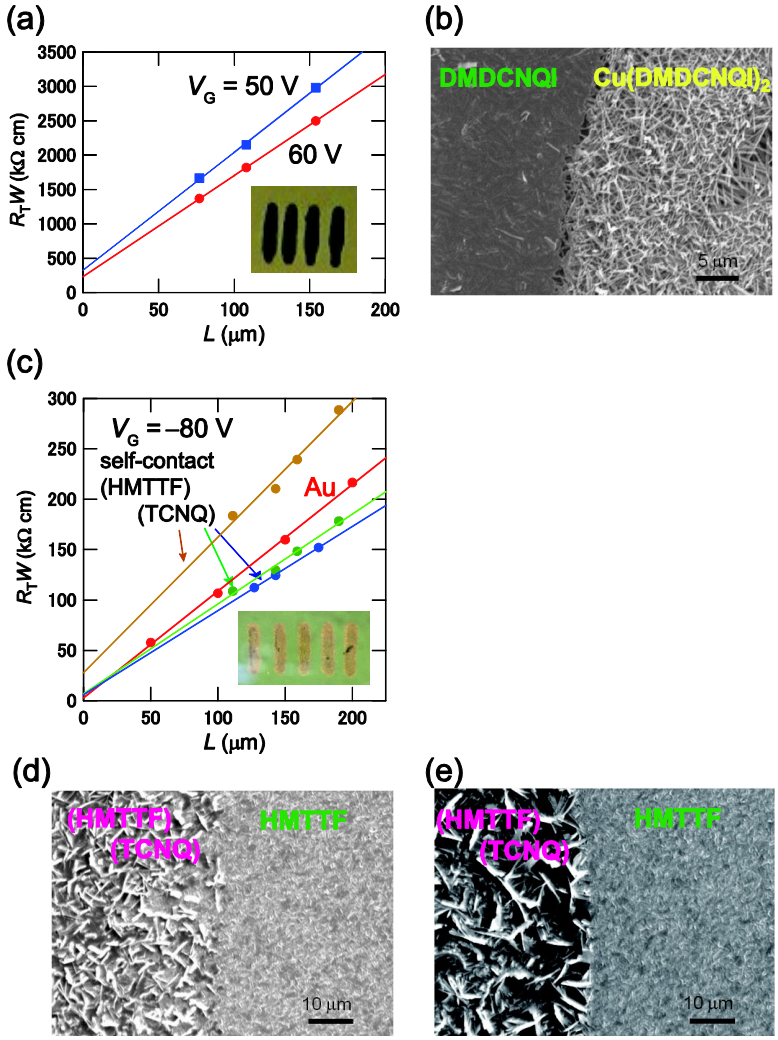

Figure 4-8. (a) Estimation of the contact resistance by the transfer-line method, and (b) a SEM image of the electrode/semiconductor interface region in a DMDCNQI self-contact transistor. (c) Transfer-line method and a SEM image for HMTTF self-contact transistors from (d) CB/DMSO and (e) AN/DMSO. The insets of (a) and (c) show the optical images of the device regions.

Figure 4-8 shows contact resistance and scanning electron microscopy (SEM) images at the electrode/semiconductor interface. Although the electrode edges are not perfectly straight, the L values are sufficiently determined to carry out the transfer-line method. For DMDCNQI, the obtained contact resistance, 235 kΩ cm, is larger than 130 kΩ cm of similarly prepared Au-top-contact transistors. A small gap is potentially

formed between the CT complex and the active layer. The (HMTTF)(TCNQ)/HMTTF interface is more smoothly connected, and the resulting contact resistance 6 kΩ cm is in the same order as 3 kΩ cm in the Au top-contact transistors (Table 1). In the case of HMTTF, the chemical reaction is confined in the upper surface of the semiconductor film owing to the comparatively sluggish complex formation, and the real top-contact geometry is achieved. Then the carrier injection occurs in the longitudinal direction from the electrode to the semiconductor, and the current flows in the laterally connected organic semiconductor. In contrast, the rapid reaction of DMDCNQI with CuI results in the complex formation penetrating down to the deep region, and leads to the relatively poor lateral connectivity across the semiconductor/electrode interface regions (Figure 7b). The reaction rate is also seriously influenced by the solubility of the organic semiconductor in the ink-jet solvent. The rapid reaction of DMDCNQI is associated with the good solubility of DMDCNQI in AN, whereas the slow reaction of HMTTF is related to the poor solubility in AN and DMSO. HMTTF shows better solubility in CB than AN, so that the combination of CB/DMSO shows larger contact resistance than AN/DMSO (Table 1). This is related to the better morphological connection between the electrode and the semiconductor (Figure 7e). The dopant (TCNQ), however, has to show a good solubility in the ink-jet solvent. An appropriately slow reaction rate is preferable for realizing the well-defined top-contact geometry.

4.5 Energy-level engineering

Energy-level matching between the inorganic-metal electrode and the organic semiconductor is not simple because the interfacial potential usually makes the Schottky barrier larger than the naive energy level difference.[40] However, the present method guarantees that the Fermi level of the electrode appears close to the energy level of the active layer, because the electrode and the active layer are composed of the same molecule. In addition, the interfacial polarization is unimportant in the organic/organic interface.[12,42] After chemical doping, the CT complex has a partially-filled energy band. $Cu(DMDCNQI)_2$ is an anion-radical salt, where the electron transport is maintained by the organic acceptor. Since Cu is $Cu^{4/3+}$, and DMDCNQI has 2/3− charge,[41,42] the LUMO level of DMDCNQI is one-third filled. When the band center of the $Cu(DMDCNQI)_2$ band is located at the same position as the original LUMO level of DMDCNQI (4.65 eV), after the band formation with the band width of 0.8 eV,[41,42] the Fermi level is pushed down by approximately 0.1 eV from the original LUMO level. Similar interpretation is applicable to the cation-radical salts. On the other hand, (HMTTF)(TCNQ) is a donor-acceptor complex, in which the energy bands come from both the donor and the acceptor molecules. The bandwidths of HMTTF and TCNQ are 0.3 eV and 0.4 eV, respectively.[43] Upon band formation, the Fermi level is expected to be located in between HOMO (4.60 eV) of HMTTF and LUMO (4.58 eV) of TCNQ.[44–47] As a consequence, the Fermi level is located very close to the energy level of the active layer (Figure 4-9). In contrast, the energy level of the standard electrode material, Au, appears around 5.1 eV.[48] Electrical conductivity of the bulk CT complex is considerably lower than that of Au and this is responsible for the comparatively high sheet resistance (Figure 5a). Nonetheless, the contact resistance

and the mobility are nearly the same in the self-contact transistors. These results indicate that efficient carrier injection is achieved due to approximately the same energy levels. The present "self-contact" technique is a method that automatically guarantees a close energy-level alignment at the electrode/semiconductor interface, and provides an ideal semiconductor-specific electrode.

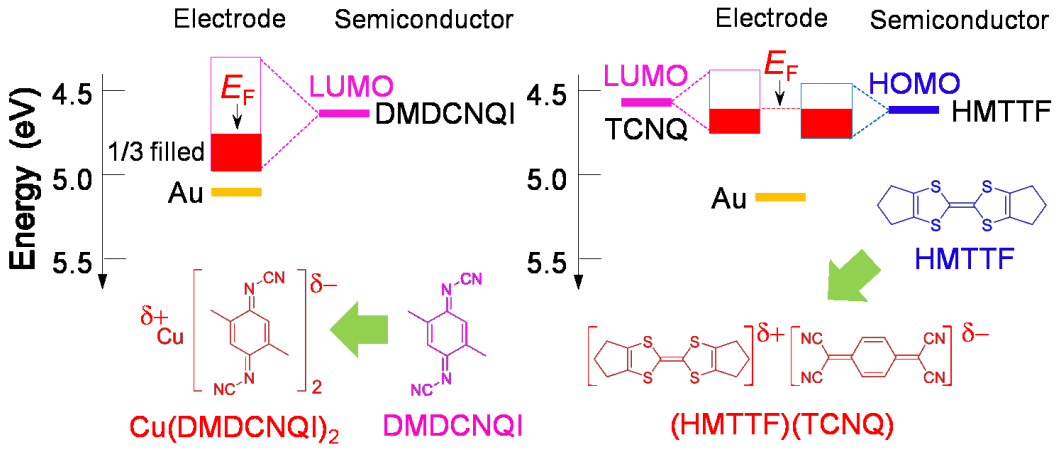

Figure 4-9. Energy-level engineering in self-contact (a) DMDCNQI and (b) HMTTF transistors.

Among the chemically doped polymers, poly(3,4-ethylenedioxythiophene):poly (styrenesulfonate) PEDOT:PSS has been used widely, but unfortunately PEDOT does not work as a good organic semiconductor. When a single organic molecule forms the active layer of an organic device and a highly conducting and stable CT complex working as the electrode parts at the same time, we can construct self-contact transistors. As far as these requirements are fulfilled, the present self-contact technique is widely applicable in other materials, even in solution-processed polymers. This is a promising strategy to use the method of conventional silicon technology in organic electronics.

4.6 Conclusion

In conclusion, a pattern of a conducting CT complex is formed on an organic semiconductor film by selective chemical doping, using ink-jet printing. In addition to the HMTTF-based p-channel transistors, we have realized n-channel self-contact transistors by using DMDCNQI. So fabricated n- and p-channel self-contact transistors maintain comparable performance to the ordinary metal-electrode transistors. In the printing process, choice of the ink-jet solvent is important. The solvent should be a good solvent of the dopant but a poor solvent of the active layer, because once the active layer dissolves, the rapid reaction results in a disordered electrode/semiconductor interface. By the chemical doping, we can obtain the semiconductor-specific electrode, whose Fermi level is inherently located very close to the energy level of the active layer. Such energy-level engineering realizes smooth charge carrier injection and high-performance organic transistors without using inorganic metal electrodes.

4.7 References

1 K. Tsukagoshi, I. Yagi, K. Shigeto, K. Yanagisawa, J. Tanabe, and Y. Aoyagi, *Appl. Phys. Lett.* **87**, 183502, (2005).

2 C. Vanoni, S. Tsujino, and T. A. Jung, *Appl. Phys. Lett.* **90**, 193119, (2007).

3 T. Minari, T. Miyadera, K. Tsukagoshi, Y. Aoyagi, and H. Ito, *Appl. Phys. Lett.* **91**, 053508, (2007).

4 C.-a. Di, G. Yu, Y. Liu, X. Xu, D. Wei, Y. Song, Y. Sun, Y. Wang, D. Zhu, J. Liu, X. Liu, and D. Wu, *J. Am. Chem. Soc.* **128**, 16418, (2006).

5 C.-a. Di, G. Yu, Y. Liu, Y. Guo, Y. Wang, W. Wu, and D. Zhu, *Adv. Mater.* **20**, 1286, (2008).

6 I. Kymissis, C. D. Dimitrakopoulos, and S. Purushothaman, *IEEE Trans. Electron Devices* **48**, 1060, (2001).

7 C. Bock, D. V. Pham, U. Kunze, D. Käfer, G. Witte, Ch. Wöll, *J. Appl. Phys.* **100**, 114517, (2006).

8 Y. Takahashi, T. Hasegawa, Y. Abe, Y. Tokura, K. Nishimura, and G. Saito, T *Appl. Phys. Lett.* **86**, 063504, (2005).

9 M. Hiraoka, T. Hasegawa, T. Yamada, Y. Takahashi, S. Horiuchi, and Y. Tokura, *Adv. Mater.* **19**, 3248, (2007).

10 M. Hiraoka, T. Hasegawa, Y. Abe, T. Yamada, Y. Tokura, H. Yamochi, G. Saito, T. Akutagawa, and T. Nakamura, *Appl. Phys. Lett.* **89**, 173504, (2006).

11 K. Shibata, H. Wada, K. Ishikawa, H. Takezoe, and T. Mori, *Appl. Phys. Lett.* **90**, 193509, (2007).

12 K. Shibata, K. Ishikawa, H. Takezoe, H. Wada, and T. Mori, *Appl. Phys. Lett.* **92**, 023305, (2008).

13 S. H. Ko, J. Chung, H. Pan, C. P. Grigoroloulos, and D. Poulikakos, *Sens.Actuators B* **134**, 161, (2007).

14 D. Kim, S. Jeong, S. Lee, B. K. Park, and J. Moon, *Thin Solid Films* **515**, 7692, (2007).

15 S. Gamerith, A. Klug, H. Scheiber, U. Scherf, E. Moderegger, and E. J. W. List, *Adv. Funct. Mater.* **17**, 3111, (2007).

16 S. H. Ko, H. Pan, C. P. Grigoropoulos, J. M. J. Fréchet, C. K. Luscombe, and D. Poulikakos, *Appl. Phys. A* (Berlin) **92**, 579, (2008).

17 H. Wada and T. Mori, *Appl. Phys. Lett.* **95**, 253307, (2009).

18 J. Inoue, H. Wada, and T. Mori, *Jpn. J. Appl. Phys.* **49**, 071605, (2010).

19 S. Tamura, T. Kadoya, T. Kawamoto, and T. Mori, *Appl. Phys. Lett.* **102**, 063305, (2013).

20 Y. Noguchi, T. Sekitani, and T. Someya, *Appl. Phys. Lett.* **89**, 253507, (2006).

21 Y. -H. Kim, B. Yoo, J. E. Anthony, and S. K. Park, *Adv. Mater.* **24**, 497 (2012).

22 H. Sirringhaus, T. Kawase, R. H. Friend, T. Shimoda, M. Inbasekaran, W. Wu, and E. P. Woo, *Science* **290**, 2123, (2000).

23 T. Kawase, T. Shimoda, C. Newsome, H. Sirrnghaus, and R. H. Friend, *Thin Solid Films*, **438-439**, 279, (2003).

24 Z. Bao, J. A. Rogers, and H. E. Katz, *J. Mater. Chem.* **9**, 1895, (1999).

25 P. Calvert, *Chem. Mater*. **13**, 3299, (2001).

26 H. Minemawari, Y. Toshikazu, H. Matui, J. Tsutsumi, S. Haas, R. Chiba, R. Kumai, and T. Hasegawa, *Nature* **475**, 364, (2011).

27 H. Wada, K. Shibata, Y. Bando, and T. Mori, *J. Mater. Chem.* **18**, 4165, (2008).

28 T. Takahashi, S. Tamura, Y. Akiyama, T. Kadoya, T. Kawamoto, and T. Mori, *Appl. Phys. Express* **5**, 061601, (2012).

29 Y. Takahashi, T. Hasegawa, S. Horiuchi, R. Kumai, Y. Tokura, and G. Saito, *Chem. Mater.* **19**, 6382, (2007).

30 T. Yamada, R. Kumai, Y. Takahashi, and T. Hasegawa, *J. Mater. Chem.* **20**, 5810, (2010).

31 A. Aumüller, P. Erk, G. Klebe, S. Hünig, J. U. Von. Schütz, and H. P. Werner, *Angew. Chem. Int. Ed. Engl.* **25**, 740, (1986).

32 S. Tamura, T. Kadoya, and T. Mori, *Appl. Phys. Lett.* **105**, 023301, (2014).

33 T. Mori, H. Inokuchi, A. Kobayashi, R. Kato, and H. Kobayashi, *Phys. Rev. B* **38**, 5913, (1988).

34 R. L. Greene, J. J. Mayerle, R. R. Schumaker, G. Castro, P. M. Chaikin, S. Etemad, and S. J. LaPlaca, *Solid State Commun.* **20**, 943, (1976).

35 Y. Ito, A. A. Virkar, S. Mannsfeld, J. H. Oh, M. Toney, J. Locklin, and Z. Bao, *J. Am. Chem. Soc.* **131**, 9396, (2009).

36 A. Aumüller, P. Erk, S. Hünig, E. Hädicke, K. Peters, and H. G. von Schnering, *Chem. Ber.* **124**, 2001, (1991).

37 R. Kato, H. Kobayashi, and A. Kobayashi, *J. Am. Chem. Soc.* **111**, 5224, (1989).

38 J. A. Lim, W. H. Lee, H. S. Lee, J. H. Lee, Y. D. Park, and K. Cho, *Adv. Func. Mater*. **18**, 229, (2008).

39 S. Matsuzaki, Z. S. Li, and M. Sano, *Synth. Metal* **38**, 269, (1990).

40 H. Ishii, K. Sugiyama, E. Ito, and K. Seki, *Adv. Mater*. **11**, 605, (1999).

41 H. Kojima, H. Kojima, Z. Zhang, K. R. Dunbar, and T. Mori, *J. Mater. Chem. C* **1**, 1781, (2013).

42 T. Kadoya, D. de Caro, K. Jakob, C. Faulmann, L. Valade, and T. Mori, *J. Mater. Chem.* **21,** 18421, (2011).

43 Y. Ji-min, *Solid State Commun.* **84**, 895, (1992).

44 H. Meng, J. Zheng, A. J. Lovinger, B. -C. Wang, P. G. V. Patten, and Z. Bao, *Chem. Mater.* **15**, 1778, (2003).

45 K. Seki, *Mol. Cryst. Liq. Cryst.* **171**, 255, (1989).

46 G. Saito and J. P. Ferraris, *Bull. Chem. Soc. Jpn.* **53**, 2141, (1980).

47 Y. Takahashi, T. Hasegawa, Y. Abe, Y. Tokura and G. Saito, *Appl. Phys. Lett.* **88**, 073504, (2006).

48 H. B. Michaelson, *J. Appl. Phys.* **48**, 4729, (1977).

Chapter 5

A Highly Conducting Organic Charge-Transfer Complex $(BTBT)_2PF_6$

5.1 Introduction

In 2007, Takimiya *et al.* reported excellent organic field-effect transistors (OFETs) based on [1]benzothieno[3,2-*b*][1]benzothiophenes (BTBT) (Figure 5-1(a)).[1] Since then, considerable attention has been devoted to the BTBT series materials. In particular, very high mobility of 31 $cm^2 V^{-1} s^{-1}$ has been attained in the printed thin-film transistors using C_8-BTBT.[2] BTBT has a large ionization potential, and the resulting low-lying highest occupied molecular orbital (HOMO) level (5.7 eV, Figure 5-1(b)), which is significantly lower than those of representative organic semiconductors such as pentacene (4.85 eV),[3] is considered to be important to achieve the stable transistor performance, because it is resistive to air oxidation.

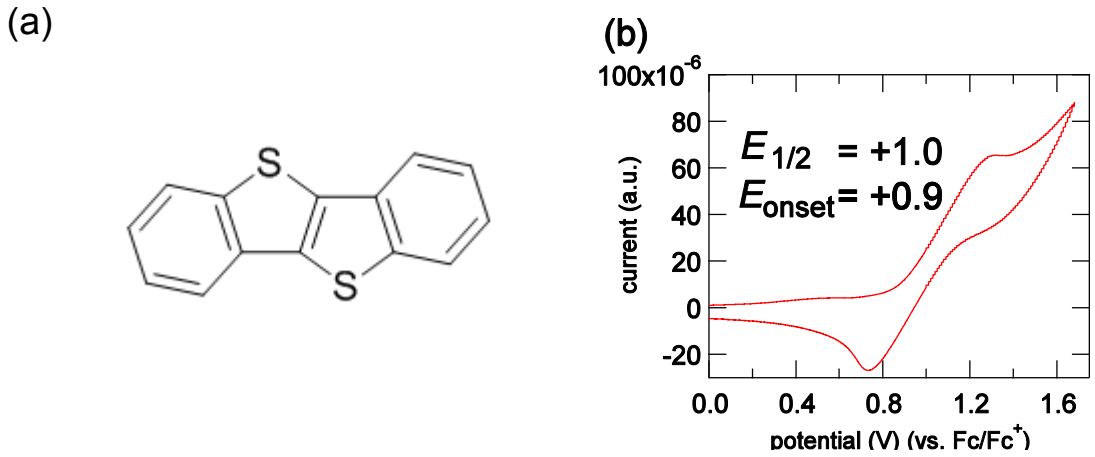

Figure 5-1. (a) Molecular structure of BTBT. (b) Cyclic voltammorgram of BTBT.

As well as the field effect in transistors, chemical doping is another way to generate carriers in organic materials, and bulk high conductivity has been realized in organic charge-transfer (CT) complexes.[4] Representative organic donors such as tetrathiafulvalene (TTF) have an even higher HOMO level (4.78 eV), and electron acceptors like 7,7,8,8-tetracyano-*p*-quinodimethane (TCNQ) has the lowest unoccupied molecular orbital (LUMO) level near the position (4.64 eV).[5] As a result, the Fermi level of conventional organic metals is located in a surprisingly limited range of 4.8 $\pm$ 0.2 eV.[6]

In organic transistors, energy-level engineering is important, and appropriate selection of metal electrodes not only reduces the Schottky barrier but also even changes the carrier polarity. For instance, a Ca contact (2.87 eV)[7] injects electrons to the LUMO of pentacene (3.2 eV),[3] and electron transport is achieved in a pentacene transistor.[8] However, energy-level alignment at the interface between a metal electrode and an organic semiconductor is not so simple, and an additional interfacial potential appears usually in an unfavorable direction to increase the Schottky barrier.[9]

In this connection, we have used an organic CT complex, (TTF)(TCNQ), as electrodes in organic transistors,[10] and succeeded in significantly reducing the contact resistance owing to the preferable organic-organic interface.[11] As shown in Chapters 3 and 4, I have developed a new type of "self-contact" organic transistors, where by chemical doping, an organic semiconductor is selectively transformed to a conducting CT complex and used as the electrodes.[12] Chemical doping is a conventional method in silicon technology, but it is characteristic of organic electronics that basically a single-component organic semiconductor is used as a unipolar carrier-transporting material. On the contrary, if an organic molecule works as an organic semiconductor as well as a high-conducting CT complex at the same time, we can use it in such self-contact organic transistors in addition to other new applications. However, representative organic semiconductors such as pentacene do not form a highly conducting and stable CT complex. This is my motivation to investigate CT complexes derived from organic transistor materials, in particular BTBT. I have found that $(BTBT)_2PF_6$ is stable enough and shows very high conductivity even at room temperature. A highly conducting CT complex with a deep Fermi level has a tremendous importance in designing organic electronics, particularly in self-contact organic transistors. From the viewpoint of organic conductors, most organic superconductors have been based on TTF derivatives, but recently superconductivity has been reported in alkali-doped picene and phenanthrene.[13] It is therefore of interest to explore conducting CT complexes based on donors and acceptors with new skeletons. In this chapter, the structural, conducting, magnetic, and optical properties of $(BTBT)_2PF_6$ are described.

5.2 Experimental

BTBT was prepared according to the previous report.[14] Rod-like black crystals of the PF_6 salt were grown by electrochemical oxidation of BTBT (2–5 mg) in dehydrated dichloromethane using tetrabutyl ammonium hexafluorophoshate as a supporting electrolyte (14–20 mg) under a constant current of 5 μA at 20 ^oC for 2–3 days. Low-temperature electrochemical oxidation (~ −10 °C) is effective to improve the crystal quality of weak electron donors such as BTBT. The X-ray diffraction data of the PF_6 salt were collected by using a Rigaku AFC-7R diffractometer with graphite monochromated Mo Kα radiation (0.71069 Å). The crystal structures were solved by the direct method (SIR2008[15]) and refined by full-matrix least squares on F^2 (SHELXL-97[16]). X-ray photographs were taken on a Rigaku R-AXIS RAPID-II diffractometer using CuKα radiation (λ = 1.54187 Å) monochromated by confocal mirror (Rigaku VariMax). Cyclic voltammograms (CVs) were measured in dichloromethane containing tetrabutylammonium hexafluorophospate as a supporting electrolyte at a scan speed of 0.1 V/s. Counter and working electrodes were made of Pt and glassy carbon, respectively, and the reference electrode was Ag/AgCl. The potentials were calibrated with the standard ferrocene/ferrocenium redox couple. For other organic materials, the energy levels were estimated from the redox potentials *vs*. SCE by adding 4.44 eV[17]

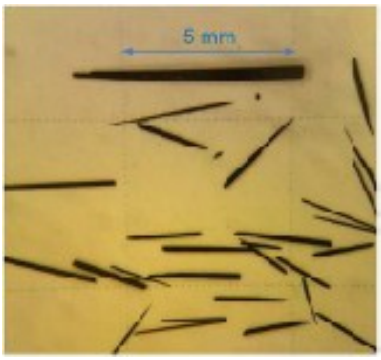

Figure 5-2. Optical images of single crystals of $(BTBT)_2PF_6$

5.3 Crystal structure

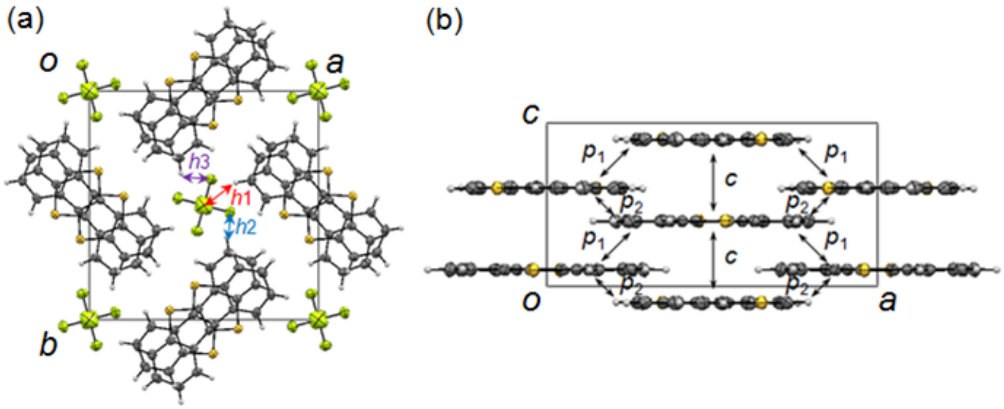

Figure 5-3. Crystal structure of $(BTBT)_2PF_6$ (a) viewed along the *c* axis, with F-H short contacts: 2.57 Å for *h*1, 2.51 Å for *h*2, and 2.60 Å for *h*3. (b) Donor arrangement as well as the transfer integrals between the neighboring donor molecules: $c = -87$, $p1 = -1.4$, and $p2 = -0.12$ meV.

The molecular packing and the intermolecular interactions are depicted in Figure 5-3. The crystal belongs to a highly symmetrical tetragonal space group $P\text{-}42_1c$ (no. 114, Table 5-1). The crystallographically independent units consist of half the donor molecule and quarter the anion, so that the composition is 2:1. The donor molecules are planar, and form stacks along the *c* axis. The nearby stacks are arranged in a

windmill manner, where the molecules are perpendicular to each other.[18] Short F-H contacts exist between donor hydrogen and anion fluorine atoms in Figure 5-3(a). The interplanar spacing in the stack is 3.37 Å, but the molecules are alternately arranged with respect to the sulfur position. The molecules are, however, related to each other by a *c*-glide plane, and the intrastack transfer is uniform as designated as *c* in Figure 5-3(b). The interstack interactions are expected to be small ($c / p_1 = 60$). The energy bands and the Fermi surface are calculated on the basis of the tight-binding approximation with the intermolecular overlap integrals of HOMO obtained from the MOPAC, AM1 molecular orbital calculation.[19] The HOMO forms a one-dimensional band with the bandwidth of 0.35 eV with open Fermi surface (Figure 5-4).

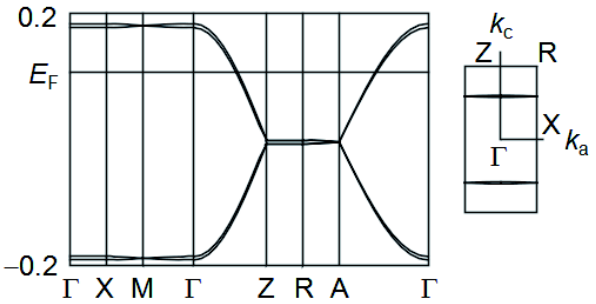

Figure 5-4. Energy band structure and the Fermi surface of $(BTBT)_2PF_6$. M: (π/a, π/a, 0), R: (0, π/a, π/c), and A: (π/a, π/a, π/c).

5.4 Transport properties

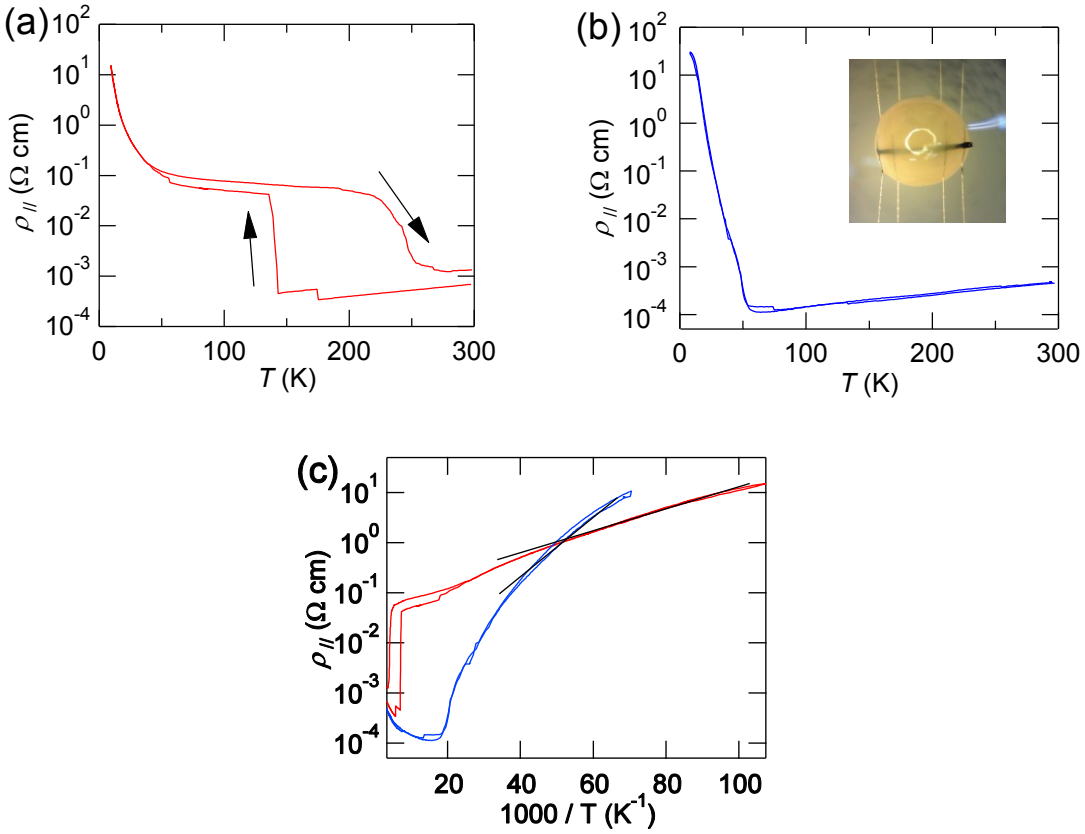

Figure 5-5. Temperature dependence of the resistivity along the *c* axis without (a) and with Apiezon N grease (b). The inset shows the optical image of the sample coated by Apiezon N grease. (c) Arrhenius plots of $(BTBT)_2PF_6$. Red curve presents the result for a free sample, and the blue curve shows the result for an Apiezon coated sample.

Figure 5-5 shows temperature dependence of the resistivity measured by the four-probe method. The current is applied along the crystal long axis, which is along the molecular stacking axis (//*c*). Electrical conductivity at room temperature is as high as 1500 S cm^{-1}. Drift mobility μ is evaluated from the following equation,

$$\mu = \frac{\sigma}{ne}$$

where σ is the electrical conductivity, n is the carrier number in a unit cell, and e is the

elementary charge. $(BTBT)_2PF_6$ has the 2:1 composition, so one BTBT molecule has 0.5+ charge because PF_6 has 1– charge. According to Figure 5-3(a), a unit cell includes four BTBT molecules. From these, the drift mobility at room temperature is,

$$\mu = \frac{\sigma}{ne}$$

$$= \frac{1500\ \mathrm{S/cm}}{4 \times 0.5 \times \frac{1}{1225 \times 10^{-24}\ \mathrm{cm}^3} \times \left(1.6 \times 10^{-19}\ \mathrm{C}\right)}$$

$$= 5.7\ \mathrm{cm}^2/\mathrm{Vs}$$

This value does not conflict with the reported high field-effect mobility,[1,20] though it is not possible to directly compare the mobility of CT complexes with the field-effect mobility of the neutral molecule. High room-temperature conductivity exceeding 1000 S cm^{-1} has been reported in several organic CT complexes,[21] but mostly achieved by the use of strong electron donors and acceptors containing selenium and tellurium atoms, which largely enhance the intermolecular interaction.[22] The transverse conductivity is estimated to be 40 S cm^{-1} at room temperature, so the longitudinal / transverse conductivity ratio is about 40.

This salt exhibits a metallic conductivity below room temperature and undergoes a resistivity jump around 150 K (Figure 5-6). Large hysteresis is observed between the cooling and heating runs, so that the change from the high-conducting state to the low-conducting state is considered to be first order. Below 150 K, this material still shows conductivity exceeding 10 S cm^{-1} and nearly flat temperature dependence. The resistivity starts to increase below 60 K, where the activation energy is as small as 57 K. The resistivity jump is, however, suppressed by coating the crystal with Apiezon N grease, because this method is reported to generate a pressure of about 0.3 kbar.[23] As a result, the high-conducting state is stabilized down to 60 K, and the conductivity

amounts to 8900 S cm^{-1} at 60 K. The resistivity starts to increase below 60 K with the activation energy of 140 K, where practically no hysteresis is observed. The low-temperature activation energy is still smaller than 225 K of (TTF)(TCNQ),[24] though the transition temperatures are approximately the same. The resistivity jump at 150 K is very sensitive to the pressure, but the insulating state below 60 K is unaffected, in which the resistivity increases to about the same value as the non grease case. When the resistivity is measured again immediately after the first temperature cycle, the resistivity increases gradually from much higher temperatures as shown in Figure 5-6(a). However, when the resistivity is measured one month after the first measurement, the resistivity jumps approximately at the same temperature as the first measurement (Figure 5-6(b)). The present observation suggests that after the largely hysteretic resistivity jump, the relaxation occurs during several weeks.

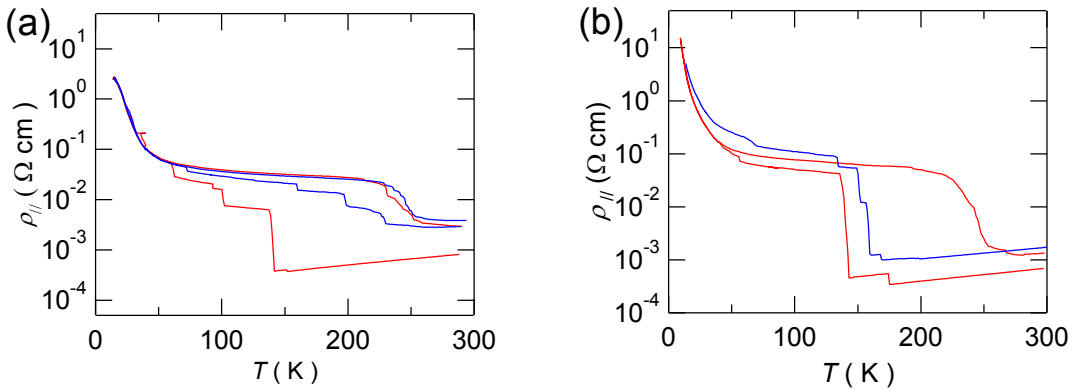

Figure 5-6. Temperature dependence of the resistivity, (a) immediately after and (b) one month after the first measurement. Red curve is the first and blue curve is the second measurement.

To clarify the origin of the resistivity jump, low-temperature X-ray crystal structure analysis is carried out (Figure 5-7). However, all lattice constants are

perfectly continuous down to 100 K, and the 100 K structure is the same as the room-temperature structure (Table 5-1). At 110 K, no extra spots or diffusive lines are detected (Figure 5-7(c)), and the crystal structure is analyzed under the same tetragonal space group $P\text{-}42_1c$ (no. 114). An attempt to analyze the low-temperature structure under the reduced symmetry ($P\text{-}4$) has not improved the result. Accordingly, the structural change associated with the resistivity jump is, if any, small.

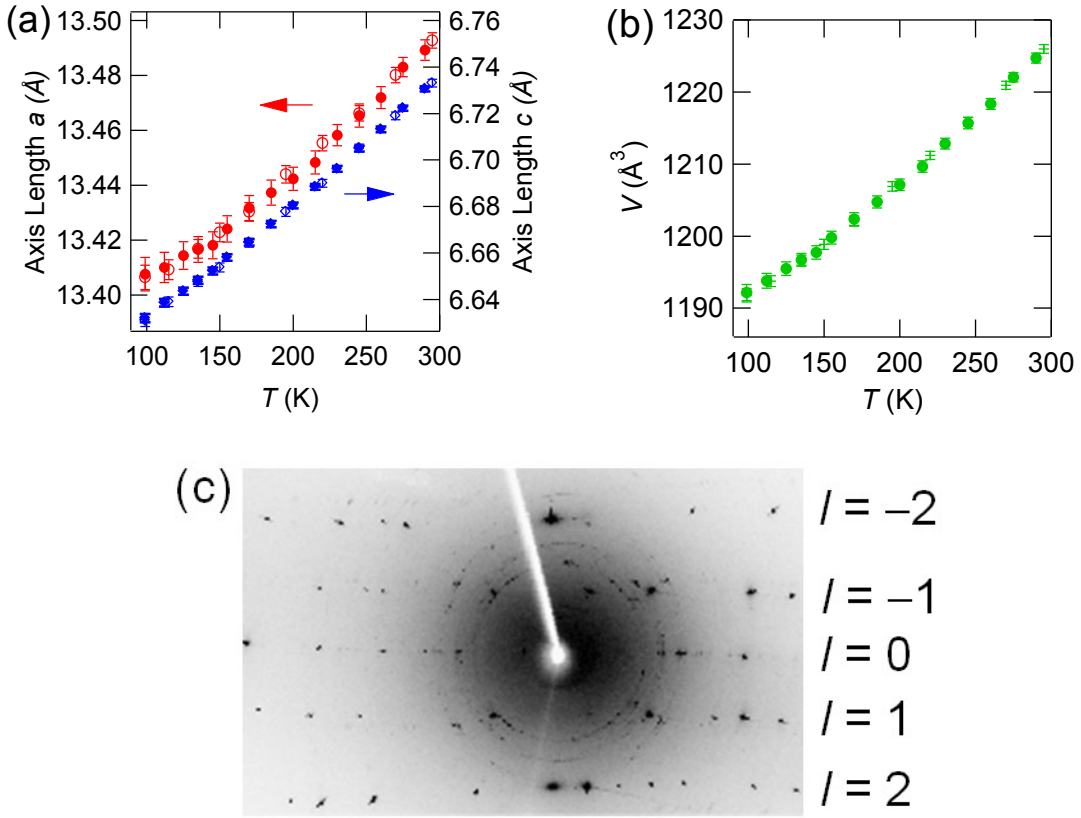

Figure 5-7. (a) Temperature dependence of the lattice constants a (red circles), c (blue diamonds) and (b) volume (green circles). Closed symbols are from the cooling run, and the open symbols are from the heating run. (c) X-ray photograph of $(BTBT)_2PF_6$ at 110 K.

Table 5-1. Crystallographic data of $(BTBT)_2PF_6$ at 298 K and 100 K

formula	$C_{28}H_{16}S_4PF_6$	$C_{28}H_{16}S_4PF_6$
crystal size	$0.12 \times 0.12 \times 0.25$ mm^3	$0.12 \times 0.12 \times 0.25$ mm^3
T (K)	298	100
crystal system	tetragonal	tetragonal
space group	P-42_1c	P-42_1c
a (Å)	13.490(2)	13.407(5)
c (Å)	6.734(2)	6.638(6)
V (Å^3)	1225.4(4)	1193(2)
Z	2	2
D_{calc} (g cm^{-3})	1.695	1.741
independent reflections	1120	1065
observed reflections [$I > 2\sigma(I)$]	718	863
$R1$; $wR2$ [$I > 2\sigma(I)$]	0.0392; 0.1368	0.0438; 0.1291
GOF	0.854	0.951

Figure 5-8 shows pressure dependence of the resistivity measured using a clamp cell. The resistivity jumps around 1 kbar at room temperature, where the resistivity increases by one to two orders. This pressure-induced resistivity jump looks like the temperature-induced resistivity jump at 150 K. When reducing the pressure, the resistivity decreases gradually but does not entirely return to the original value. We can repeat the jump and recovery of the resistivity. After the first resistivity jump, the resistivity jump tends to occur at lower pressures. The pressure-induced insulating state reminds us $Cu(DMDCNQI)_2$ (DMDCNQI: dimethyldicyanoquinonediimine),[25]

where the Jahn-Teller distortion around Cu is the origin of the insulating state. After the pressure-induced resistivity jump at room temperature, the sample does not show metallic conductivity, but exhibits slowly increasing behavior, which is followed by a semiconducting region below 50 K (Figure 5-5(a)). The gradual increase resembles the ambient-pressure flat region between 150 K and 50 K, where the observed resistivity of 0.02 Ω cm is somewhat smaller than the ambient-pressure flat resistivity (0.1 Ω cm) owing to the applied pressure. The start of the insulating region is gradually lowered by pressure, and the activation energy decreases linearly with the pressure (Figure 5-8(c)). It is expected that the insulating state below 60 K will be suppressed when more than 12 kbar is applied.

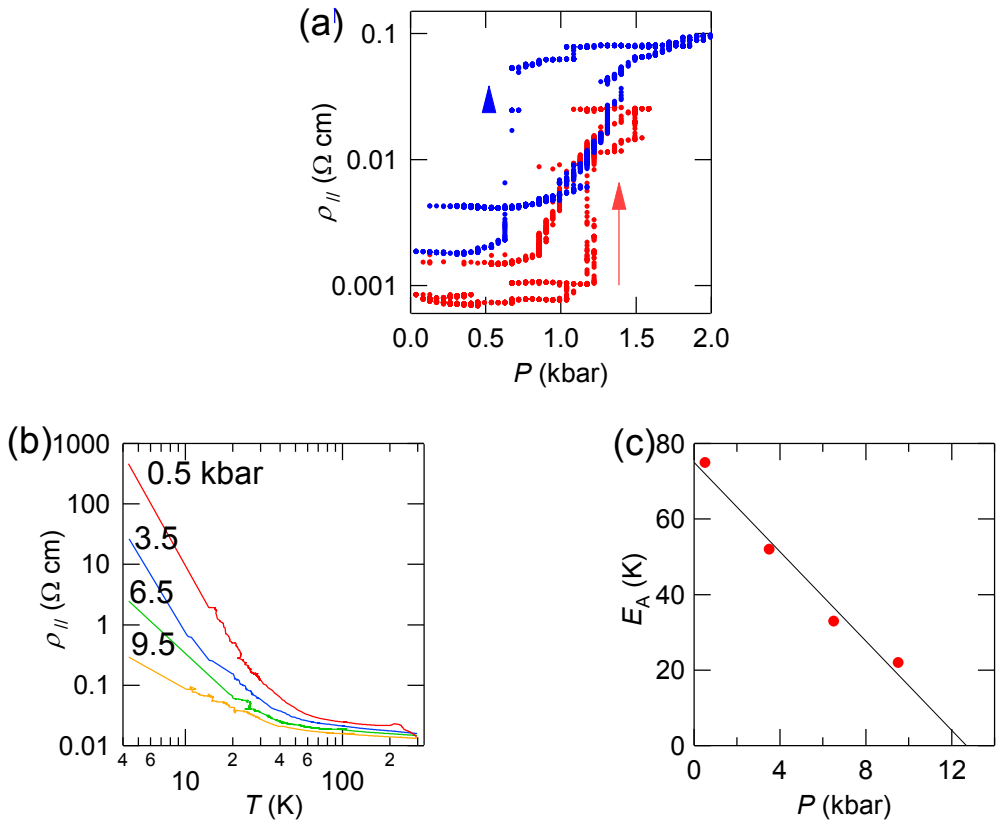

Figure 5-8. (a) Pressure dependence of the resistivity at room temperature. (b) Temperature dependence of the resistivity under pressure. The low-temperature pressure values are reduced by 3 kbar from the room-temperature values. (c) Activation energy plotted as a function of the low-temperature pressure.

5.5 Electron spin resonance (ESR)

On account of the high conductivity, the ESR signal shows highly asymmetrical Dysonian shape depending on the field orientation and the sample size.[26] As shown in Figure 5-9, when the magnetic field is rotated from //*b* to //*c* for a relatively large sample, the asymmetry *A* / *B* varies from 3.0 for *H* // *b* to 2.5 for *H* // *c*. However, when a thin needle-like sample is rotated around the *c* axis, the lineshape is a symmetrical Lorentzian because the width of the thin needle does not exceed the skin depth.

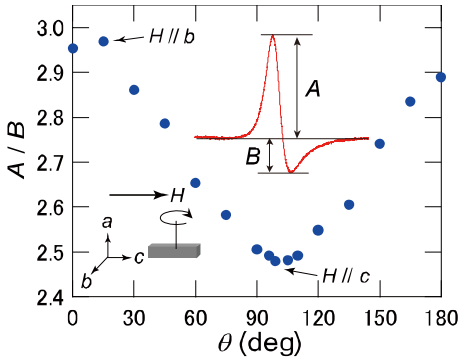

Figure 5-9. Angle dependence of ESR signal asymmetry, *A* / *B* at room temperature for a crystal with the size of 0.22 x 0.22 x 2.4 mm^3. The insets show the definition of *A* / *B* and the field directions.

In order to estimate the critical size, the skin depth is calculated from,[26]

$$d = \sqrt{\frac{2}{\mu_0 \sigma \omega}}$$

where d is the skin effect, μ_0 is the magnetic permeability in vacuum, σ is the electrical conductivity, and ω is the frequency of the micro wave. So the skin depth in the *a* axis is

$$d = \sqrt{\frac{2}{1500 \times 10^2 \text{ S/m} \times 9 \times 10^9 \text{ Hz} \times 4\pi \times 10^{-7} \text{ H/m}}}$$

$$= 0.3433 \times 10^{-4} \text{ m}$$

$$\cong 30 \text{ μm}$$

Then the skin depth in the *a* axis is estimated to be approximately 30 μm from the conductivity (//*c*). The skin depth in the *c* axis is similarly calculated to be 200 μm.

The linewidth and the *g* values of a Dysonian signal were defined as shown in Figure 5-10(a). The *A* and *B* values were directly estimated from the lineshape. Angle dependence of these parameters for the sample rotation around the *a* axis at room temperature was depicted in Figure 5-10(b). From this, the *g* values were obtained to be $g_{//c} = 2.002$ and $g_{\perp c} = 2.003$.

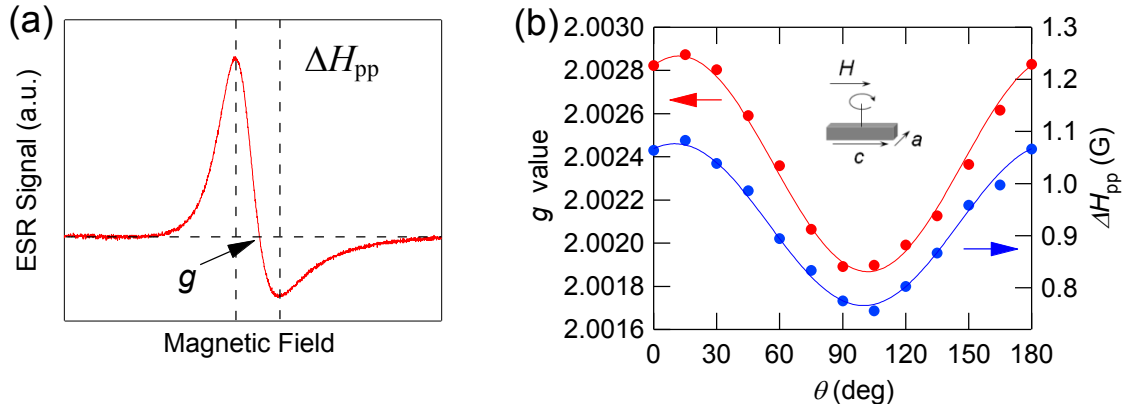

Figure 5-10. (a) Definition of the linewidth and the *g* value in a Dysonian signal. (b) Angle dependence of the *g* values and the linewidth for the sample rotation around the *a* axis.

Owing to the perpendicular molecular arrangement in the crystal, we could not directly relate these values to the *g* values of the molecule. When the sample is rotated around the *c* axis, the signal is a perfect Lorentzian (A / B ~ 1), and the *g* value does not change (2.003) reflecting the tetragonal symmetry (Figure 5-11).

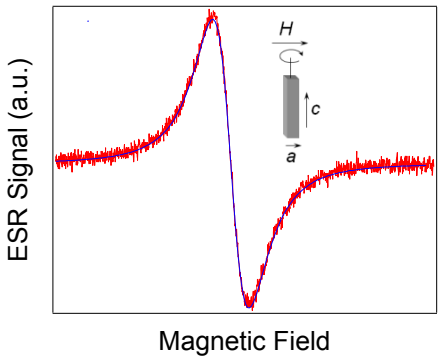

Figure 5-11. Lineshape of the ESR signal for $H \perp c$. The blue curve is a fit to the Lorentzian curve.

For H // c, the lineshape depends on the sample size; a large rod-like crystal shows a Dysonian (A / B ~ 2.5 as shown in Figure 5-11), whereas a small needle-like crystal gives a Lorentizian (A / B ≅ 1.2).

Among organic conductors, doped polyacetylene shows Dysonian,[27] whereas in several BEDT-TTF salts and the analogs, Dysonian has been observed only in the low-temperature metallic region.[28] In these single-crystal CT salts, the A / B value does not strictly fulfill the Dyson theory (A / B ≥ 2.7) at room temperature.[26] It is therefore noteworthy that a very weak electron donor such as BTBT forms high-conducting and thick enough crystals to exhibit the Dysonian lineshape.

Figure 5-12 shows the temperature dependence of the normalized spin susceptibility (χ), peak-to-peak linewidth (ΔH_{pp}), and asymmetry A / B. The spin susceptibility decreases gradually, and shows a relatively rapid drop at about 100 K (Figure 5-12(a)) and shows an increase coming from the Curie tail below 20 K. On account of the gradual decrease below 100 K, the Peierls-type distortion is a possibility of the low-temperature insulating state. However, since the Curie tail is not very large, χ is not considered to be entirely zero even after contribution from the Curie tail is subtracted. ΔH_{pp} is as narrow as 1 G around room temperature. For Lorentzian signals, ΔH_{pp} starts to increase below 150 K corresponding to the resistivity jump, but decreases below 30 K due to the Curie tail (Figure 5-12(b)). For Dysonian signals, ΔH_{pp} slightly increases below 200 K and rapidly reduces below 60 K in accord with the insulating state. This temperature dependence is reminiscent of (TTF)(TCNQ),[30] where the high-temperature broadening is ascribed to Peierls fluctuations because the spin-flip scattering increases, and the low-temperature sharpening is due to the decreasing number of available states evidenced by the decreasing spin susceptibility. In the

present case, however, the low-temperature linewidth sharpening does not obviously correspond to the decreasing spin susceptibility.

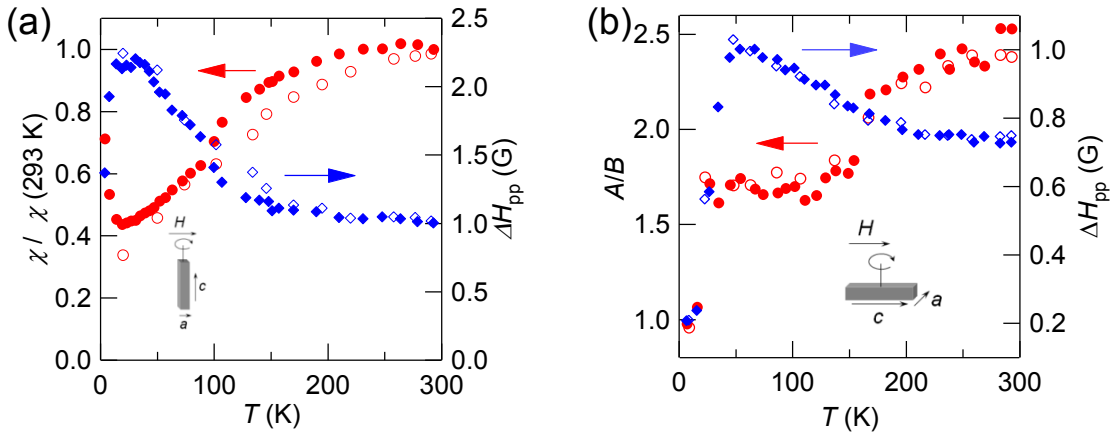

Figure 5-12. Temperature dependence of (a) the normalized spin susceptibility χ, and the linewidth ΔH_{pp} in Lorentzian. (b) The asymmetry A / B and the linewidth ΔH_{pp} in Dysonian for the field directions in the inset. The closed and open symbols are for cooling and heating runs.

The A / B value decreases gradually with decreasing the temperature but drops abruptly around the resistivity jump at 150 K (Figure 5-12(c)). After this, A / B is still as large as 1.7, but below 30 K, A / B drops to 1.0. Practically no hysteresis is observed between the cooling and heating runs. This is probably because the cooling and heating rates in the ESR measurement are much larger than the conductivity measurement. However, meaningful hysteresis has been observed in χ and ΔH_{pp} for H // a (Figure 5-12(a), (b)).

The temperature dependence of the ESR intensity (χ) does not basically depend on the field directions and the lineshape. Figure 5-13(a) is obtained by using a small needle-like crystal for H // c, where the signal is well represented by a Lorentzian. The intensity decreases gradually and finally increases owing to the Curie tail. The

linewidth is essentially the same as Figure 5-12(b). Figure 5-13(b) presents the ESR results for an Apiezon coated sample for $H \perp c$. The intensity reduces below 110 K, and the linewidth increases at the same time. The drop is slightly shifted to a lower temperature than Figure 5-12(a) and (b). This might be ascribed to imperfect suppression of the resistivity jump. Below 100 K both the intensity and the linewidth show a similar behavior to Figure 5-12.

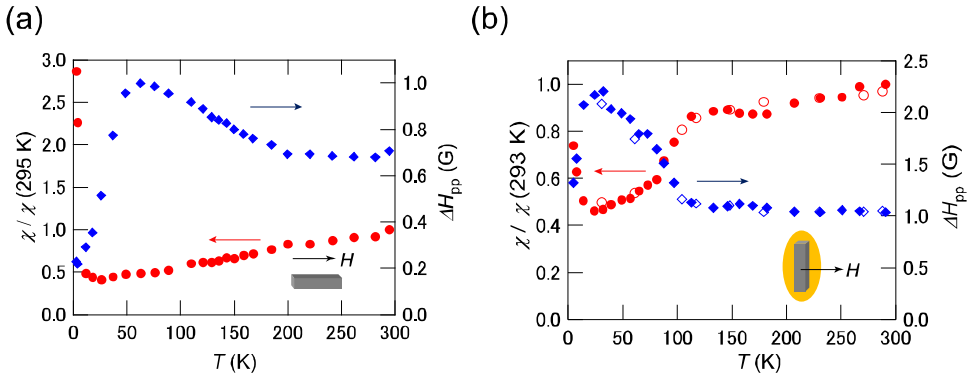

Figure 5-13. Temperature dependence of spin susceptibility χ (red circles) and linewidth ΔH_{pp} (blue diamonds) (a) for a nearly Lorentzian signal (A / $B \cong 1.2$ for H // c), and (b) for an Apiezon coated sample. The closed and open symbols are for cooling and heating runs, respectively.

5.6 Raman and infrared spectroscopy

To investigate the ground state of $(BTBT)_2PF_6$, raman and infrared (IR) spectra have been measured. Figure 5-14 represents the raman and IR spectra of the neutral and cationic BTBT calculated on the basis of Gaussion 09. Table 5-2 shows the raman-peak values for the neutral and cationic BTBT. Since HOMO spreads over the molecule, the raman shifts are relatively small compared to TTF-type molecules. The ν9 mode is suitable to investigate whether the ground state of $(BTBT)_2PF_6$ is

charge order or not, because the raman shift is large ($\Delta\omega$ = 46.66). Figure 5-15 shows the temperature dependence of the raman spectrum. There are, however, no meaningful peak shifts or splitting even at 4 K. Therefore, the low-temperature ground state is not charge order.

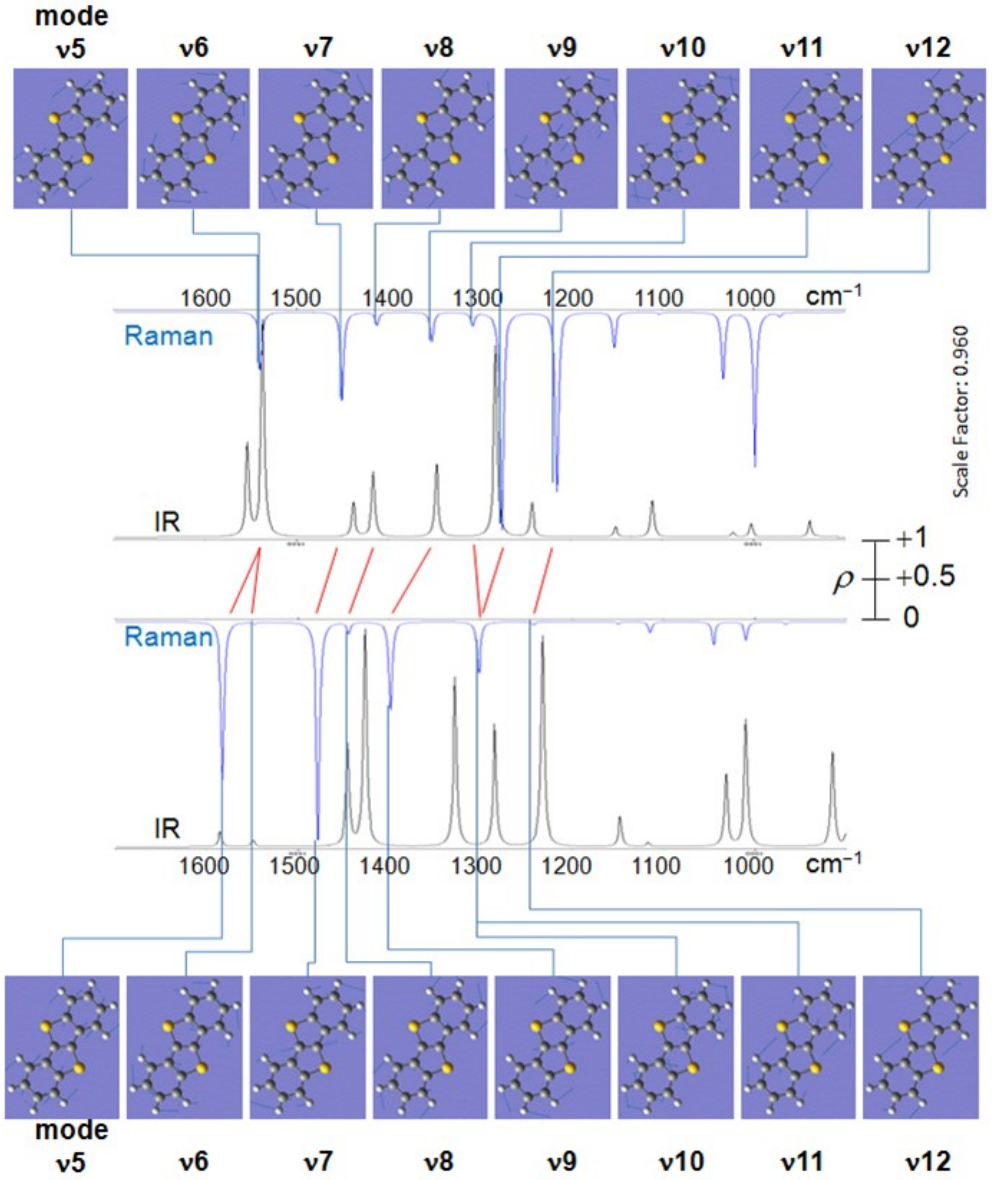

Figure 5-14. Raman shifts and IR frequency in the neutral BTBT and cationic BTBT (+1) molecules calculated by Gaussian 09. The base function is B3LYP/6-31G(d) for neutral and UB3LYP/6-31G(d) for the cation.

Table 5-2. Raman shifts of the neutral and cationic BTBT.

Mode	ν5(ag)	ν6(ag)	ν7(ag)	ν8(ag)	ν9(ag)	ν10(ag)	ν11(ag)	ν12(ag)
ω(neutral)	1582.577	1548.078	1478	1444.573	1398.656	1303.4	1301.747	1242.597
ω(cation)	1546.769	1539.523	1450.096	1412.124	1351.992	1307.213	1275.434	1215.024
Δω	35.80762	8.55494	27.90461	32.44944	46.66387	−3.81312	26.31302	27.57293
g constant	77.255	146.17	204.11	109.737	70.2318	97.8856	124.223	6.58423

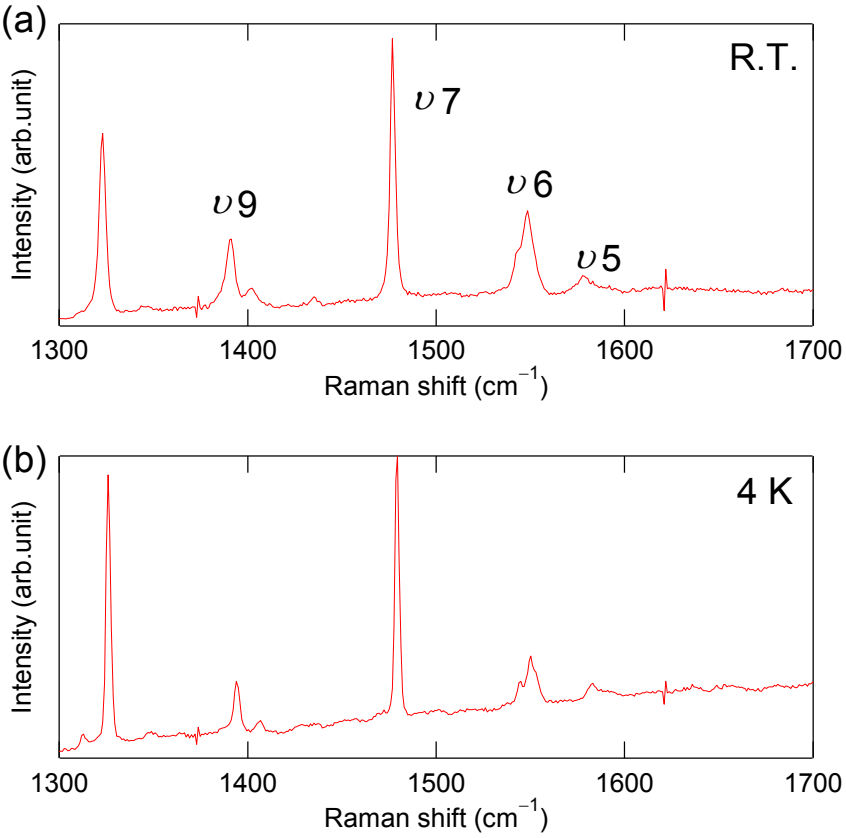

Figure 5-15. Raman spectra of $(BTBT)_2PF_6$ at (a) room temperature, and (b) 4 K.

Figure 5-16 shows the temperature dependence of the reflectance spectrum, where the electric field is parallel to the *c* axis. Although the *a*-parallel reflectance spectrum is not observed with sufficient quality, the electric state is considered to be highly one-dimensional because of the anisotropy of the conductivity. Below 8000 cm^{-1}, the reflectance increases drastically and makes a plateau. As shown in Figure 5-5, the resistivity shows a metallic behavior, but the reflectance spectra do not show the Drude edge clearly, and decrease in the low-frequency range. This result suggests that a small energy gap opens even at room temperature. Although it is possible that the spectrum is fitted to only the Lorentz model, the *c*-parallel spectrum is analyzed on the basis of the Drude-Lorentz model (Figure 5-17).

$$R = \left|\frac{\sqrt{\tilde{\epsilon}} - 1}{\sqrt{\tilde{\epsilon}} + 1}\right|^2$$

$$\tilde{\epsilon} = \epsilon_\infty - \frac{\omega_P^2}{\omega^2 + i\omega\Gamma} - \frac{\omega_{P1}^2}{(\omega^2 - \omega_1^2) + i\omega\Gamma}$$

where *R* is the reflectance, $\tilde{\epsilon}$ is the complex dielectric function, ϵ_∞ represents for the frequency-independent dielectric constant, ω_P and Γ are the plasma frequency and the relaxation rate of the charge carriers, respectively, and ω_1, Γ_1, and ω_{P1} are the parameters of the Lorentz oscillators. From the plasma frequency, the transfer integral parallel to the *c* axis is evaluated by the following equation based on the one-dimensional tight-binding approximation:

$$\omega_P^2 = \frac{4ta^2e^2\sin(\frac{\pi\rho}{2})}{\pi\epsilon_0\bar{h}^2V_m}.$$

Here, *a* is the intermolecular spacing (*a* = 3.37 Å), V_m is the volume per molecule (V_m = 1225/4 $Å^3$), ρ is the degree of charge transfer per molecule (ρ = 0.5) and ω_P = 11500 cm^{-1}.[31] The obtained transfer integral *t* is 0.34 eV and the bandwidth 4*t* is 1.35 eV.

This value is not in good agreement with the calculated one, but such a large transfer integral is consistent with the highly conductivity exceeding 1000 S/cm. The optical zero-frequency conductivity is estimated by the following equation:

$\sigma_{\mathrm{opt}}(0) = \frac{\varepsilon_0 \omega_{\mathrm{P}}^2}{\Gamma}$.

from Γ = 2300 cm^{-1} (Table 5-3).

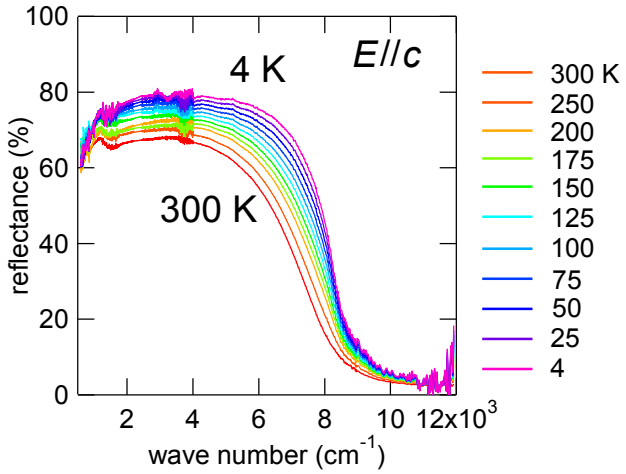

Figure 5-16. Temperature dependence of reflectance spectrum of $(BTBT)_2PF_6$.

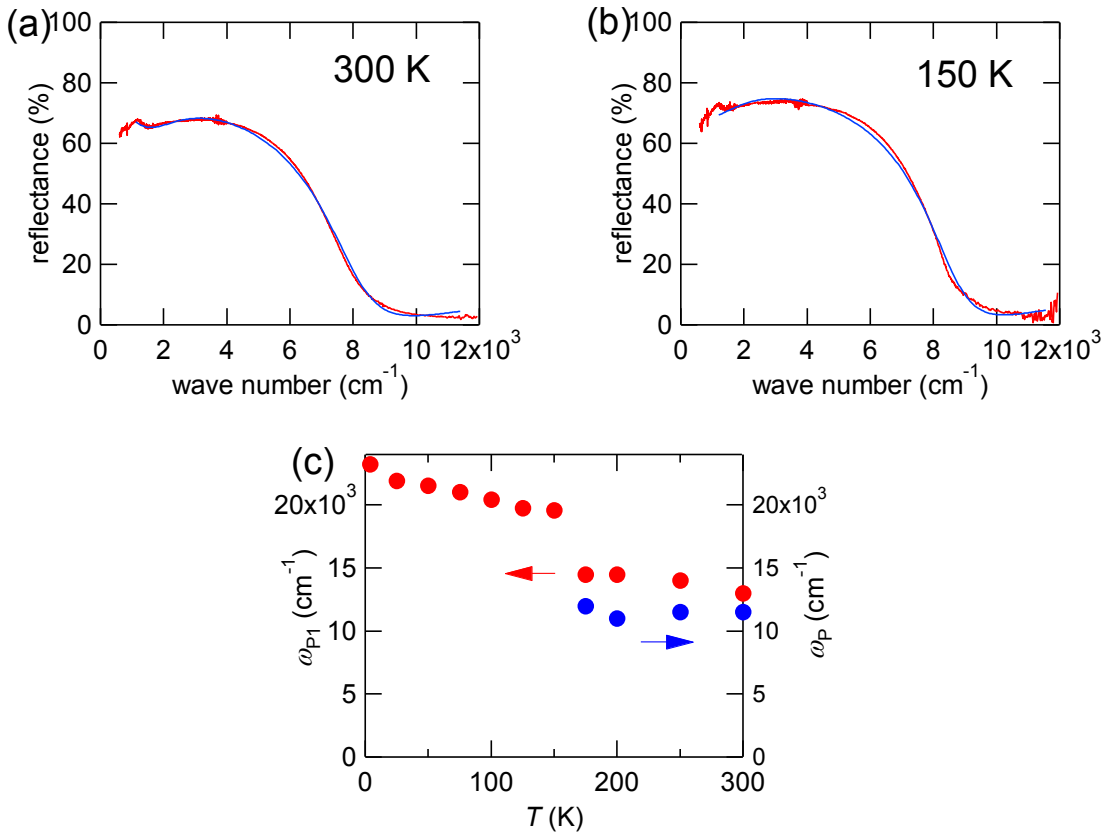

Figure 5-17. Fitting curves analyzed by the (a) Drude and Lorentz, and (b) Lorentz models. (c) Temperature dependence of ω_{P1} and ω_P.

Table 5-3. Transfer integral and electrical conductivity

t_{calc} (eV)	t_{opt} (eV)	σ_{dc} (S/cm)	σ_{opt} (S/cm)
0.087	0.34	1500	1000

Below 150 K, the spectra are not satisfactorily analyzed by the Drude-Lorentz model but well fitted to the Lorentz model (Figure 5-17(b)). Figure 5-17(c) shows temperature dependence of ω_{P1} and ω_P. The behavior of ω_{P1} is very similar to the resistivity (Figure 5-5). Figure 5-18(a) shows the temperature dependence of the

optical conductivity estimated by the Kramers-Kronig transformation. The peak around 3000 cm^{-1} is ascribed to the energy gap. The peaks from 1200 cm^{-1} to 1600 cm^{-1} are the vibronic bands, where infrared active intramolecular vibrations occur owing to the e-mv coupling. As shown in Figure 5-18(b), the spectral shapes change with decreasing the temperature, indicating that some molecular vibrations are thermally activated. For instance, the peak around 1380 cm^{-1} increases gradually, and changes drastically below 150 K (Figure 5-19). This behavior is also in good agreement with the resistivity jump. Therefore, the resistivity jump around 150 K and the insulating state below 60 K are attributed to some kind of lattice modulation like the Peierls distortion.

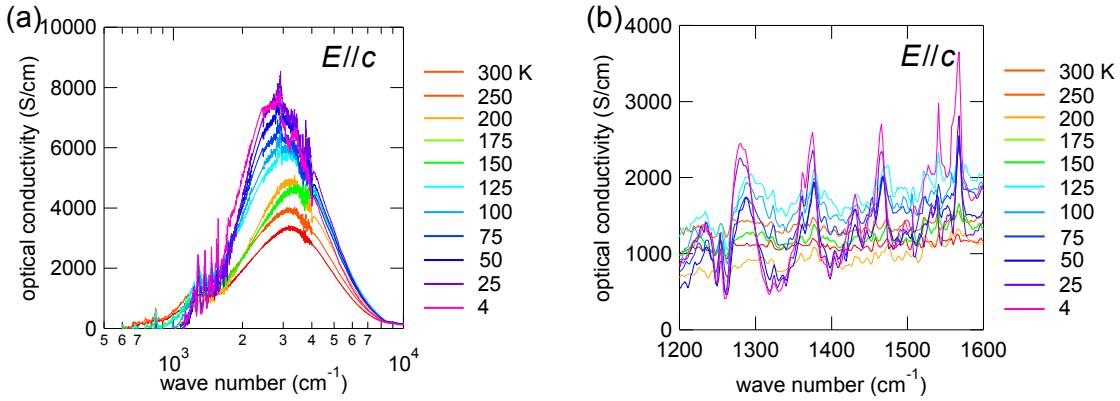

Figure 5-18. Temperature dependence of the optical conductivity in $(BTBT)_2PF_6$.

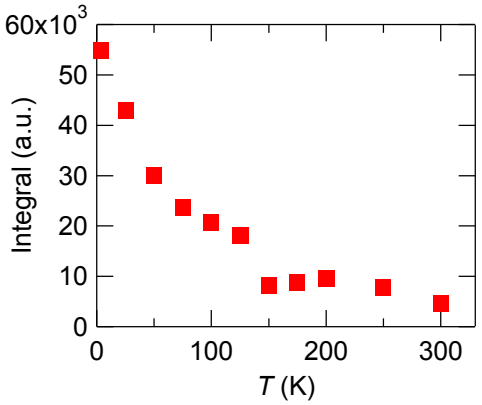

Figure 5-19. Temperature dependence of the peak intensity around 1380 cm^{-1}.

5.7 Energy levels and HOMO

Ionization potentials of the representative organic donors and work functions of inorganic metals are shown in Figure 5-20. The Fermi level of radical-cation salts are closely related to the ionization potential of the organic donor.[6] Similarly, the Fermi level of 1:1 donor-acceptor complexes such as (TTF)(TCNQ) is located in between the HOMO level of the donor and the LUMO of the acceptor.[10]

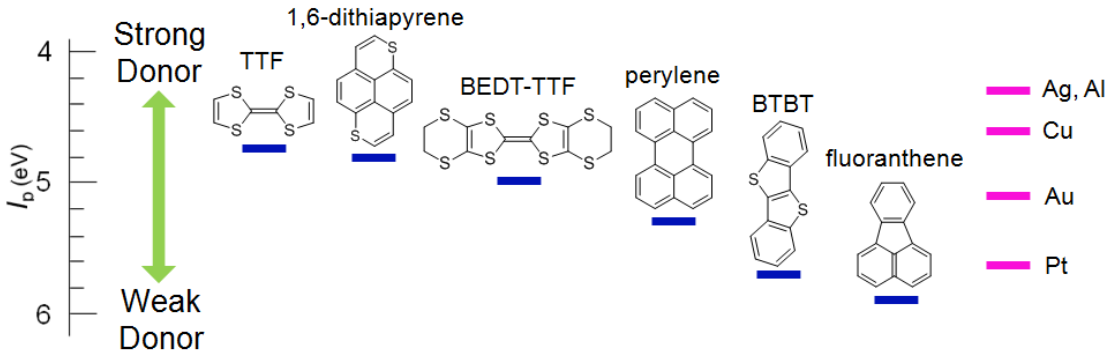

Figure 5-20. Energy levels of representative organic donors and inorganic metals.

As an example of organic donors without a TTF skeleton, 1,6-dithiapyrene (I_p = 4.8 eV) forms CT salts with TCNQ,[31] in which the conductivity is 150 S cm^{-1} and the metallic state is maintained down to 60 K.[32] Fluoranthene is an extremely weak donor (I_p = 5.9 eV)[5] and makes the CT salts with PF_6, AsF_6, and SbF_6. The room-temperature conductivity is, however, smaller than 0.05 S cm^{-1}.[33] There is a general tendency that difficulty in forming stable conducting CT salts gradually increases with increasing the ionization potential because ion-radical states of weak electron donors are chemically less stable. Perylene (I_p = 5.3 eV)[5] is a relatively weak donor and produces conducting CT salts in the form of (perylene)$_2X$ for X = PF_6, AsF_6, and metal dithiolates. These salts show high room-temperature conductivity of

50-1400 S cm^{-1},[34] but Dysonian ESR spectrum has not been reported. These salts form highly one-dimensional stacks, and undergo the Peierls transitions. As shown in Figures 5-3 and 4, $(BTBT)_2PF_6$ has one-dimensional stacks, but the ground state does not seem to be a simple non-magnetic state. Since the ionization potential of BTBT is large, the Fermi level of the BTBT salt is also expected to be as deep as Pt.[7] In addition, the HOMO population of BTBT is largely located on the sulfur atoms (Figure 5-21). Although this is the HOMO of the neutral state, large intermolecular interaction and to form an efficient carrier path is expected after the CT complex formation. Since neutral TTF-type molecules also exhibit a similar tendency that the HOMO population is located on the sulfur atoms,[35] BTBT-type molecules have an suitable electric state as an organic donors.

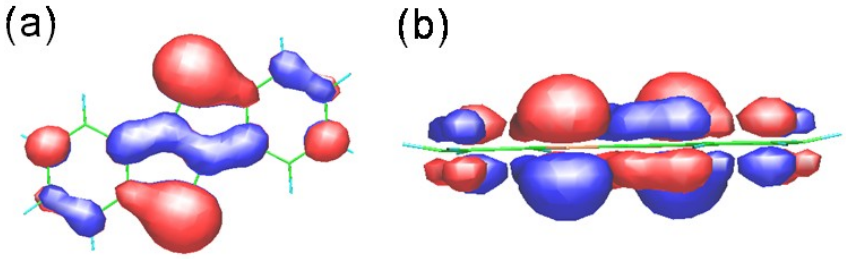

Figure 5-21. HOMO of neutral BTBT molecule calculated by MOPAC, (a) viewed perpendicular to, and (b) parallel to the molecular plane.

Even after the forty-year history of organic metals, the range of the Fermi level in conducting organic materials is still very limited.[6] The uniqueness of the present BTBT salt stems from this characteristic electronic state.

5.8 Conclusion

In conclusion, we have prepared a novel organic CT complex, $(BTBT)_2PF_6$. Although the BTBT derivatives have been well known as high-mobility organic semiconductors, BTBT is a new skeleton in organic conductors. The PF_6 salt shows remarkably high conductivity exceeding 1000 S cm^{-1} and a Dysonian ESR lineshape with significant asymmetry (A / $B \cong 3$) even at room temperature. At low temperatures, the spin susceptibility decreases but does not go down to zero. According to the optical properties, the ground state is not charge order, but attributed to the lattice modulation. These observations indicate that $(BTBT)_2PF_6$ is susceptible to some kind of lattice modulation, reflecting the highly one-dimensional electronic structure. It is, however, noteworthy that the 150 K resistivity jump has temporary and largely hysteretic nature, and the 50 K transition leads to the true ground state. It is surprising that BTBT forms a highly conducting material in spite of the very weak electron-donor ability. The present salt opens a new possibility of highly conducting CT complexes based on non-TTF molecules.

5.9 Appendix

BTBT[Ni(nmt)$_2$]

BTBT (2–5 mg) was electrochemically oxidized in dehydrated dichloromethane using tetrabutyl ammonium nickel bis(maleonitriledithiolete)metalate (Ni(nmt)$_2$) as a supporting electrolyte (14–20 mg) under a constant current of 1 μA at −10 ^{o}C for 1 week. Black rod-like crystals were grown. Figure 5-20 represents the crystal structure of BTBT[Ni(nmt)$_2$]. In contrast to the PF_6 salt, the Ni(nmt)$_2$ salt forms mix stacks along the *c* axis.

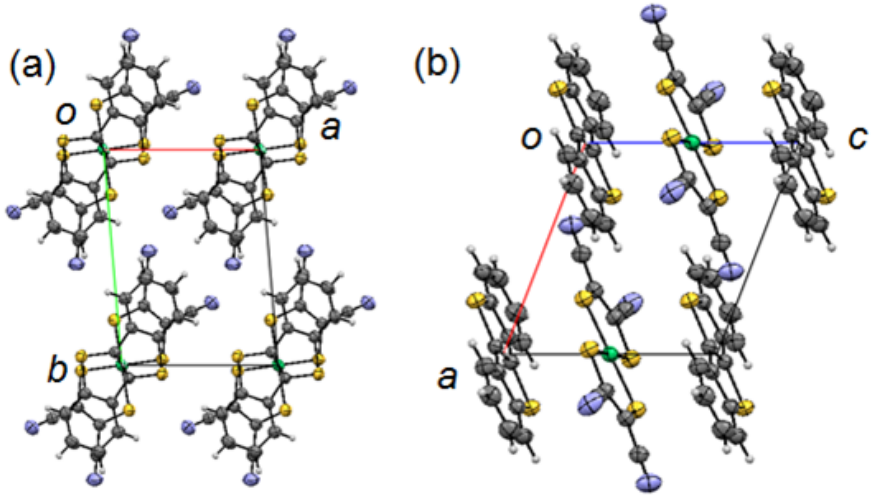

Figure 5-22. Crystal structure of BTBT[Ni(nmt)$_2$] (a) viewed along the *c* axis and (b) *b* axis.

Table 5-4. Crystallographic data of BTBT[Ni(nmt)$_2$] at 298 K.

Formula	C36H16N4NiS6
Formula weight	755.73
Shape	Black needle
Crystal System	Triclinic
Space Group	*P*-1
Z-value	1
a (Å)	7.915(3)
b (Å)	10.486(4)
c (Å)	7.610(4)
a (deg)	105.72(4)
b (deg)	113.01(3)
g (deg)	79.62(3)
V (Å ^{3})	557.7(5)
Independent Reflections	3248
D_{calc} (g/cm^3)	2.441
*R*1 [$F^2 > 2.0s$ (F^2)]	0.0434
*wR*2 [All reflections]	0.1360
GOF	0.929

5.10 References

1 (a) H. Ebata, T. Izawa, E. Miyazaki, K. Takimiya, M. Ikeda, H. Kuwabara, and T. Yui, *J. Am. Chem. Soc.* **129**, 15732 (2007). (b) T. Izawa, E. Miyazawa, and K. Takimiya, *Adv. Mater*. **20**, 3388 (2008).

2 H. Minemawari, Y. Toshikazu, H. Matui, J. Tsutsumi, S. Haas, R. Chiba, R. Kumai, and T. Hasegawa, *Nature* **475**, 364 (2011).

3 T. Yasuda, T. Goto, K. Fujita, and and T. Tsutsui, *Mol. Cryst. Liq. Cryst*. **444**, 219 (2006).

4 *Organic Superconductors, 2nd edn.*; T. Ishiguro, K. Yamaji, and G. Saito, Springer: Berlin, **2001**

5 K. Seki, *Mol. Cryst. Liq. Cryst.* **171**, 255 (1989).

6 T. Kadoya, D. de Caro, K. Jakob, C. Faulmann, L. Valade, and T. Mori, *J. Mater. Chem.* **21**, 18421 (2011).

7 H. B. Michaelson, *J. Appl. Phys.* **48**, 4729 (1977).

8 T. Yasuda, T. Goto, K. Fujita, and T. Tsutsui, *Appl. Phys. Lett*. **85***,* 2098 (2004).

9 H. Ishii, K. Sugiyama, E. Ito, and K. Seki, *Adv. Mater*. **11**, 605 (1999).

10 (a) Y. Takahashi, T. Hasegawa, Y. Abe, K. Tokura, K. Nishimura, and G. Saito, *Appl. Phys. Lett.* **86**, 063504 (2005). (b) Y. Takahashi, T. Hasegawa, Y. Abe, K. Tokura, and G. Saito, *Appl. Phys. Lett.* **88**, 073504 (2006).

11 K. Shibata, H. Wada, K. Ishikawa, H. Takezoe, and T. Mori, *Appl. Phys. Lett.* **90**, 193509 (2007).

12 (a) S. Tamura, T. Kadoya, T. Kawamoto, and T. Mori, *Appl. Phys. Lett.* **102**, 063305. (2013). (b) J. Inoue, H. Wada, and T. Mori, *Jpn. J. Appl. Phys.* **49**, 071605 (2010).

13 (a) R. Mitsuhashi, Y. Suzuki, Y. Yamanari, H. Mitamura, T. Kambe, N. Ikeda, H. Okamoto, A. Fujiwara, M. Yamaji, N. Kawasaki, Y. Maniwa, and Y. Kubozono, *Nature* **464**, 76 (2010). (b) X. F. Wang, R. H. Liu, Z. Gui, Y. L. Xie, Y. J. Yan, J. J. Ying, X. G. Luo, and X. H. Chen, *Nat. Commun*. **2**, 507 (2011). (c) M. Xue, T. Cao, D. Wang, Y. Wu, H. Yang, X. Dong, J. He, F. Li, and G. F. Chen, *Sci. Rep*. **2**, 389 (2012).

14 Y. Li, C. Nie, H. Wang, H. Li, F. Verpoort, and C. Duan, *Eur. J. Org. Chem*. **36**, 7331 (2011).

15 M. C. Burla, R. Caliandro, M. Camalli, B. Carrozzini, G. L. Cascarano, L. de Caro, C. Giacovazzo, G. Polidori, D. Siliqi, and R. Spagna, *J. Appl. Crystallogr.,* 2007, **40**, 609.

16 G. M. Sheldrick, *Acta Crystallogr., Sect. A* 2008, **64**, 112.

17 H. Meng, L. Zheng, A. J. Lovinger, B.-C Wand, P. G. V.Patten, and Z. Bao, *Chem. Mater.* **15**, 1778 (2003).

18 (a) Y. Misaki, T. Kaibuki, M. Taniguchi, K. Tanaka, T. Kawamoto, and T. Mori, *Chem. Lett.* **29**, 1274 (2000). (b) M. Fourmigué, E. W. Reinheimer, K. R. Dunbar, P. Auban-Senzier, C. Pasquier, and C. Coulon, *Dalton Trans.* 4652 (2008).

19 (a) M. J. S. Dewar, E. G. Zoebisch, E. F. Healy, and J. J. P. Stewart, *J. Am. Chem. Soc*. **107**, 3902 (1985). (b) T. Mori, A. Kobayashi, Y. Sasaki, H. Kobayashi, G. Saito, and H. Inokuchi, *Bull. Chem. Soc. Jpn.* **57**, 627 (1984).

20 M. Yamagishi, J. Soeda, T. Uemura, Y. Okada, Y. Takatsuki, T. Nishikawa, Y. Nakazawa, I. Doi, K. Takimiya, and J. Takeya, *Phys. Rev. B* **81**, 161306(R) (2010).

21 (a) A. C. Gane, P. Kathirgamanathan, and R. Rosseinsky, *J. Chem. Soc., Chem. Commun.* 378 (1981). (b) A. Kobayashi, R. Kato, H. Kobayashi, T. Mori, and H. Inokuchi, *Solid State Commun*. **64**, 45 (1987).

22 (a) K. Bechgaard, D. O. Cowan, and A. N. Bloch, *Mol. Cryst. Liq. Cryst*. **32**, 227 (1976). (b) J. M. Fabre, L. Giral, E. Dupart, C. Coulon, J. P. Manceau, and P. Delhaes, *J. Chem. Soc., Chem. Commun.* 1477 (1983). (c) M. D. Mays, R. D. McCulough, and D. O. Cowan, *Solid State Commun*. **65**, 1089 (1988). (d) G. Saito, H. Kumagai, J. Tanaka, T. Enoki, and H. Inokuchi, *Mol. Cryst. Liq. Cryst*. **120**, 337 (1985). (e) T. Jigami, T. Takimiya, T. Otsubo, and Y. Aso, *J. Org. Chem.* **63**, 8865 (1998). (f) J. A. Schlueter, Y. Orihashi, M. Kanatzidis, W. -B. Liang, and T. J. Marks, *Synth. Met.* **41-43**, 2659 (1991).

23 H. H. Wang, A. M. Kini, L. K. Montgomery, U. Geiser, K. D. Carlson, J. M. Williams, J. E. Thompson, D. M. Watkins, W. K. Kwok, U. Welp, and K. G. Vandervoort, *Chem. Mater*. **2**, 482 (1990).

24 S. Etemad, *Phys. Rev*. *B* **13**, 2254 (1976).

25 T. Mori, K. Imaeda, R. Kato, A. Kobayashi, H. Kobayashi, and H. Inokuchi, *J. Phys. Soc. Jpn.* **56**, 3429 (1987).

26 G. Feher, A.F. Kip, *Phys. Rev.* **98**, 337 (1955).

27 I. B. Goldberg, H. R. Crowe, P. R. Newman, A. J. Heeger, and A. G. MacDiarmid, *J. Chem. Phys*. **70**, 1132 (1979).

28 (a) T. Sugano, G. Saito, and K. Minoru, *Phys. Rev. B* **34**, 117 (1986). (b) S. Baudron, P. Batail, C. Coulon, R. Clérac, E. Canadell, V. Laukhin, R. Melzi, P. Wzietek, D. Jérome, P. Auban-Senzier, and S. Ravy, *J. Am. Chem. Soc.* **127**, 11785 (2005).

29 G. Waoner, *Phys. Rev.* **118**, 647 (1960).

30 Y. Tomkiewicz, *Phys. Rev*. *B* **19**, 4038 (1979).

31 K. Nakasuji, H. Kubota, T. Kotani, I. Murata, G. Saito, T. Enoki, K. Imaeda, H. Inokuchi, M. Honda, C. Katayama, and J. Tanaka, *J. Am. Chem. Soc.* **108**, 3460 (1986).

32 (a) K. Bechgaard, *Mol. Cryst. Liq. Cryst.* **81**, 125 (1985). (b) N. Thorup, G. Rindorf, C. S. Jacobsen, K. Bechgaard, I. Johannsen, and K. Mortensen, *Mol. Cryst. Liq. Cryst.* **349**, 120 (1985).

33 C. Kröhnke, V. Enkelmann, and G. Wegner, *Angew. Chem. Int. Ed. Engl.* **19**, 912 (1980).

34 (a) H. J. Keller, D. Nothe, H. Pritzkow, D. Wehe, M. Werner, P. Koch, and D. Schweitzer *Mol. Cryst. Liq. Cryst*. **62**, 181 (1980). (b) D. Schweitzer, I. Hennig, K. Bender, H. Endres, and H. J. Keller, *Mol. Cryst. Liq. Cryst*. **120**, 213 (1985). (c) V. Gama, R. T. Henriques, and M. Almeida, *Synth. Met*. **43**, 2553 (1991). (d) V. Enkelmann, *Adv. Chem*. **217**, 177 (1988).

35 H. Kojima and T. Mori, *Bull. Chem. Soc. Jpn*. **84**, 1049 (2011).

Chapter 6

Suppression of Access Resistance by Using Carbon Electrodes in Organic Transistors Based on Alkyl-Substituted Thienoacene

6.1 Introduction

Recently, considerable efforts have been devoted to the development of organic-transistor materials owing to the potential application to low-cost, large-area, and flexible electronics.[1–4] In particular, thienoacene derivatives have attracted a great deal of attention because of their high-performance and stable transistor properties.[5–11] In these high-performance organic semiconductors, well-controlled charge injection from the electrode to the organic semiconductor has tremendous importance. Contact resistance ($R_C W$) at the electrode/semiconductor interface limits the inherent characteristics of the active-layer material and reduces the device performance particularly in bottom-contact transistors with conventional metal electrodes, where W is the channel width incorporated in order to normalize the resistance. One of the attempts to reduce $R_C W$ is insertion of a buffer layer, where an organic acceptor layer is inserted between the electrode and the p-channel organic semiconductor layer.[12–14] Such a buffer layer reduces the undesirable interfacial potential to decrease $R_C W$. The morphological discontinuity is another origin of the large contact resistance.[15] A

method to eliminate the metal/organic morphological problem is thiol or fluoropolymer treatment of the electrode surface.[16-18] As another attempt, we have used a highly conducting charge-transfer (CT) complex as the electrodes, and reduced $R_C W$ of a bottom-contact transistor as low as that of a top-contact transistor.[19] Several organic CT complexes have high enough conductivity to work as electrode materials, with which we can replace inorganic metals.[20–25] In this connection, we have reported "self-contact" organic transistors; when the organic semiconductor forms a conducting organic CT complex, a part of the active layer is chemically doped and selectively transformed to the conducting CT complex, and used as the source/drain (S/D) electrodes.[26–28] In the self-contact transistors, smooth charge carrier injection is realized because both the active layer and the electrode are composed of the same organic molecule. This is another solution to reduce $R_C W$ from the standpoint of the energy-level alignment at the electrode/semiconductor interface.[28] Alternatively, conducting carbon is as useful as the CT complexes to achieve high performance and low contact resistance because of the preferable carbon/organic interface.[29]

In general, the top-contact transistors show much smaller contact resistance than the bottom-contact transistors, because the top-contact transistors are largely free from the above origins of the contact resistance. In the ordinary top-contact organic transistors, however, $R_C W$ comes from two kinds of contributions: the interface resistance (R_{int}) and the access resistance (R_{acc}).[30] R_{int} occurs in the same way from the interface between the electrode and the active layer, whereas R_{acc} comes from the longitudinal resistance of the active layer between the top contact electrode and the dielectric interface, and tends to increase proportionally to the active-layer thickness. R_{int} is reduced by using a buffer layer similarly to the bottom-contact transistors.[31–33]

In the top-contact transistors, R_{acc} is a dominant factor in determining the field-effect mobility,[34–36] and the semiconductor film has to be as thin as possible (~40 nm) in order to reduce R_{acc}. Although a considerable number of investigations have been devoted to reduce R_{int}, no effective solution has been proposed to reduce R_{acc}.

In the present chapter, we propose a method to suppress R_{acc}. As an active layer, dihexyl-substituted dibenzo[*d*,*d*']thieno[3,2-*b*;4,5-*b*']dithiophene (C_6-DBTDT) is chosen. This is one of the promising thienoacenes, which shows significantly high mobility in the usual top-contact Au transistors.[37] We have investigated the performance of C_6-DBTDT thin-film transistors by changing the semiconductor thickness and electrodes. It has been observed that remarkable morphological change derived from molecular disorder occurs near the Au electrode region, but this problem is well controlled by using carbon contact. Although the carbon-contact transistors have bottom-contact geometry and are fabricated by the solution process, the reduction of the contact resistance is significant. We demonstrate that the performance of the carbon-electrode devices does not decrease even in thick semiconductor layers; the elimination of R_{acc} is ascribed to the lateral carrier injection from the side of the thick carbon electrodes.

6.2 Experimental

The transistors were fabricated onto a highly doped n-type silicon wafer with silicon dioxide layer of 300 nm thickness (capacitance C = 13 nF cm^{-2}). Figure 6-1 illustrates the fabrication of carbon electrodes.[29] The substrate was washed with acetone, isopropyl alcohol, and ultra pure water. For the surface treatment, the substrate was exposed to hexamethyldisilazane (HMDS) vapor at 150°C for 3 h. Ultraviolet light was irradiated for 1 h through a shadow mask to form the hydrophilic region. Carbon paste (CH-10) purchased from Jujo Chemical Co., LTD was dispersed in $CHCl_3$ (1g in 30 ml) and sonicated. Supernatant of this carbon solution was dropped on the substrate using a glass capillary and annealed at 120°C for 20 min. After repeating this process two or three times, the substrate was washed ultrasonically in ethyl acetate/hexane = 1:1 and successively acetone in order to remove the carbon on the hydrophobic region. Finally, the substrate was annealed again at 120°C for 20 min. The channel length and width were measured by an optical microscope (channel length L = 33-166 μm and channel width W = 1000 μm). Since the channel boundary was slightly warping, the channel length was estimated at the minimum, so that the evaluated mobilities were also the minimum values.[28] C_6-DBTDT of about 40 nm or 120 nm thickness was evaporated under a vacuum of 10^{-4} Pa.

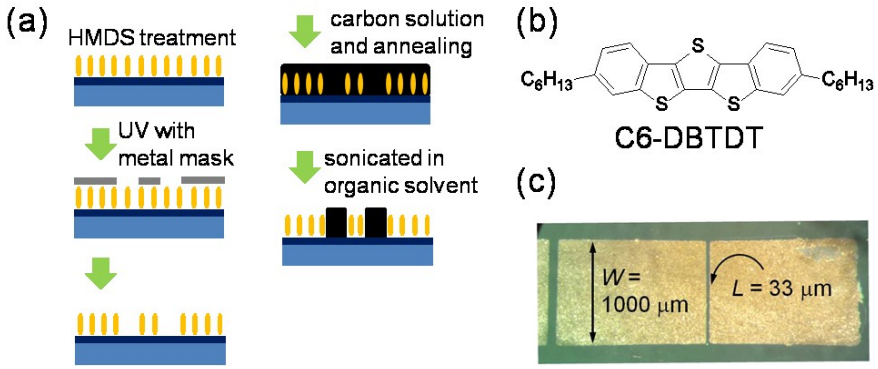

Figure 6-1. (a) Fabrication of the carbon-electrode transistors. (b) Molecular structure of C_6-DBTDT. (c) Optical image of the resulting device.

For comparison, we also fabricated the ordinary bottom- and top-contact Au transistors. The S/D electrodes were formed by vacuum evaporating Au through a metal mask (channel length L = 50-200 μm and channel width W = 1000 μm). The transistor characteristics were measured with a Keithley 4200 semiconductor parameter analyzer in the ambient condition. The field-effect mobility (μ) was estimated in the saturation region. $R_C W$ was evaluated by the conventional transfer-line method from the linear region of the output characteristics.

6.3 MAXRD patterns and AFM images

Figure 6-2 shows MAXRD patterns. On the SiO_2 surface (Figure6-2 (a)), a series of sharp peaks are observed starting from $2\theta = 3.26°$, corresponding to half the *c* axis of the C6-DBTDT single crystal.[37] Figure 6-2 (b) and (c) exhibit a peak at the same position, indicating that the C6-DBTDT molecules are oriented in an edge-on manner as well. Additional peaks at $2\theta = 26.5°$ and $2\theta = 38.3°$ are related to carbon and Au (111), respectively.[27] The in-plane (φ) rocking curve of the $2\theta = 3.26°$ peak on Au is significantly broader than those on the HMDS-treated SiO_2 and carbon (Figure 6-2(d)). This implies that a part of the C6-DBTDT molecules are tilted to some extent.

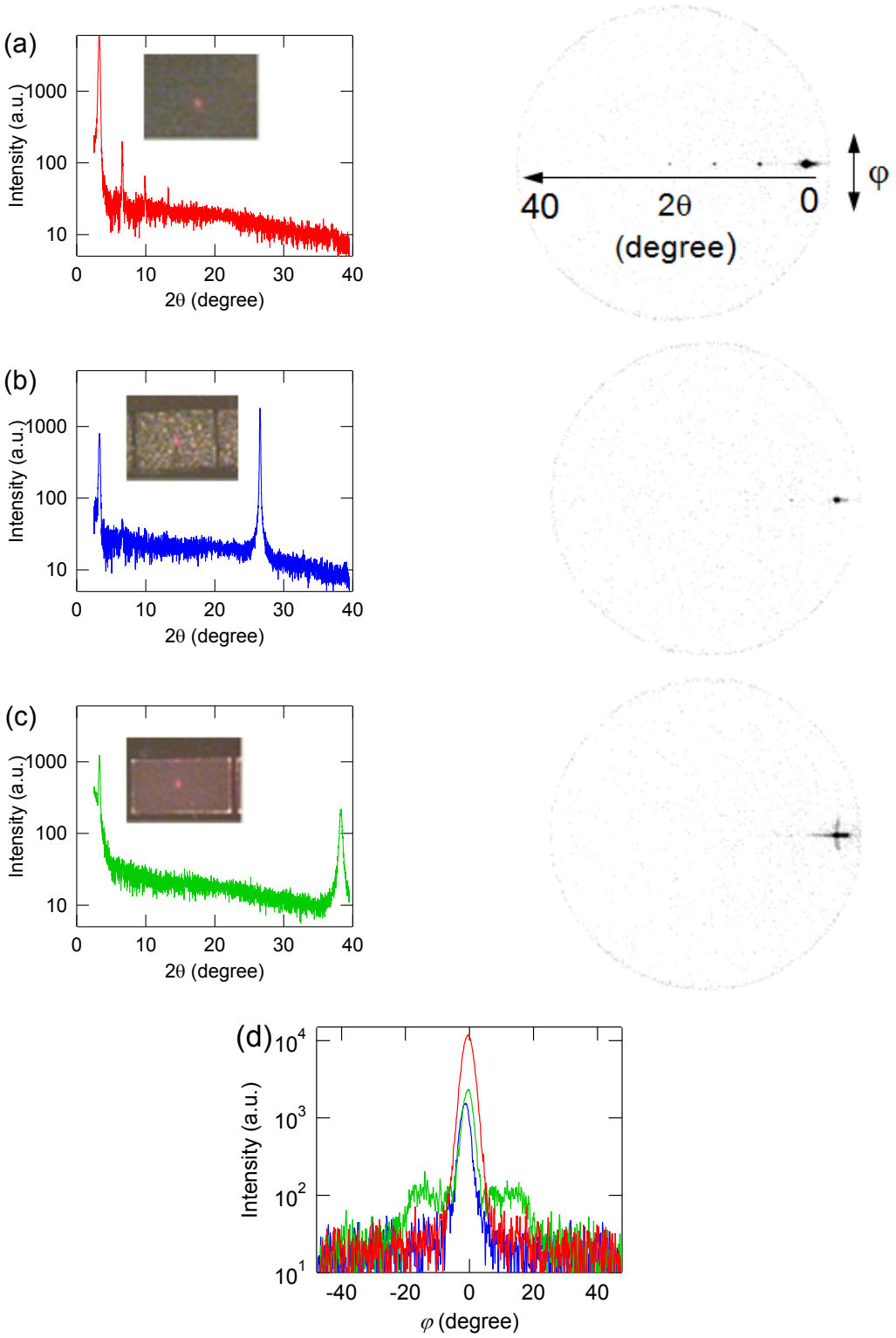

Figure 6-2. MAXRD patterns of 40 nm C6-DBTDT films on (a) HMDS-treated SiO_2, (b) carbon, and (c) Au. The insets show the optical images of the sample, where the bright spots are X-ray irradiated regions. (d) In-plane (φ) rocking curves of the $2\theta = 3.26^{o}$ peaks.

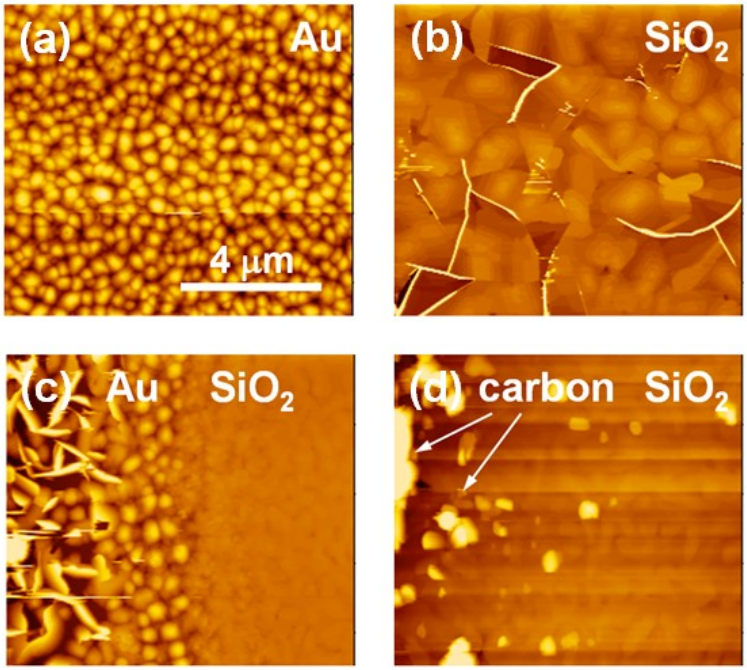

Figure 6-3. AFM images on the (a) Au, (b) SiO_2 surface, (c) around the electrode/semiconductor interface in a bottom-contact Au transistor and (d) a bottom-contact carbon transistor.

AFM images are shown in Figure 6-3. The grain size is significantly affected by the surface treatment. Accordingly, the drastic morphological discontinuity observed at the boundary of Au and HMDS-coated SiO_2 (Figure6-3 (c)). This is quite consistent with the results of the (φ) rocking curve. As previously reported, such a remarkable morphological change results in large interfacial potential and contact resistance.[15]

6.4 Transistor characteristics and contact resistance

A typical output characteristics of the carbon-electrode transistor is shown in Figure 6-4(a). The transfer characteristics are depicted in Figures 6-4(b) and (c). In the top-contact Au transistor, the performance decreases significantly with increasing the semiconductor thickness (Figure 6-4(b)). However, in the carbon-electrode transistor, the transistor property is not much influenced by the active layer thickness (Figure 6-4(c)). In this case, $R_C W$ estimated from the transfer line method is as small as 4 kΩ cm (Figure 6-4(d)).

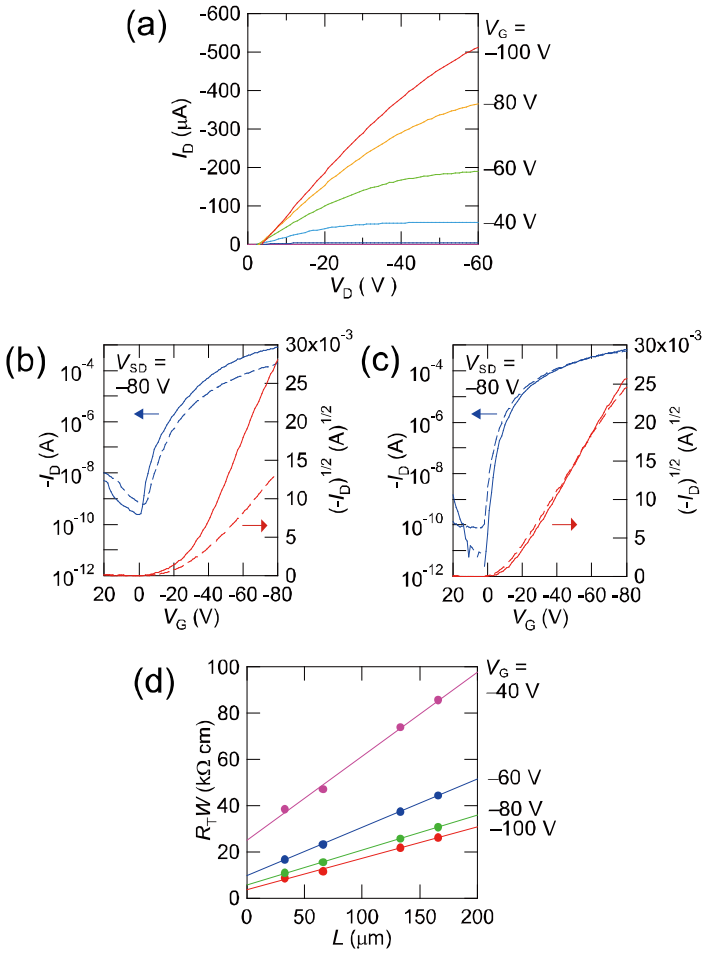

Figure 6-4. (a) Output characteristics of the carbon-electrode devices for 40 nm C6-DBTDT. (b) Active-layer thickness dependence of transfer characteristics in the top-contact Au transistors (L = 50 μm and W = 1000 μm), and (c) the carbon-electrode transistors (L = 33 μm and W = 1000 μm). The solid curve represents the 40 nm device and the dotted curve shows the 120 nm device. (d) Channel length L dependence of the total resistance R_T normalized with respect to the channel width W for carbon-electrode transistors with 40 nm C6-DBTDT.

Figure 6-5(a) shows V_G dependence of $R_C W$. In the 40 nm C6-DBTDT film, the carbon electrodes attain as low $R_C W$ as the top-contact Au transistors, though the device geometry is bottom contact. When the C6-DBTDT film thickness increases to 120 nm, $R_C W$ increases, but the top-contact Au device shows a much larger increase. Figure 6-5(b) shows semiconductor-thickness dependence of $R_C W$. Since R_{int} does not

change by the semiconductor thickness, the gradients of straight lines correspond to the R_{acc}. It is clearly observed that R_{acc} of the carbon electrodes are lower than that of the top-contact Au electrodes. When V_G is increased, R_{acc} is reduced. In addition, Figures 6-4 and 6-5 demonstrate that the carbon-electrode device is not significantly influenced by the semiconductor thickness. In particular, when V_G is large, $R_C W$ of the carbon-electrode transistors does not change depending on the active-layer thickness (Figure 6-5(a)). The resulting transistor properties are listed in Table I. The bottom-contact Au transistors, without any contact surface treatment, exhibit considerably low performance with large scatters; this is ascribed to the molecular disorder at the electrode/semiconductor interface. The top-contact Au transistors with 40 nm thickness show as large μ as the previous report, but the threshold voltage V_{th} is comparatively large.[37] A trade-off is reported in many organic thin-film transistors that when V_{th} is small, μ is reduced at the same time.[37–39] The present carbon-electrode transistors show, to some extent, the same tendency, but as large μ as 1 $cm^2\ V^{-1}\ s^{-1}$ is maintained together with the small $V_{th} \sim -12$ V. In the top-contact Au transistors, μ_{av} significantly decreases in the 120 nm transistors owing to the increased R_{acc}, and at the same time, V_{th} increases slightly. However, μ and V_{th} are not susceptible to the active layer thickness in the carbon-electrode transistors.

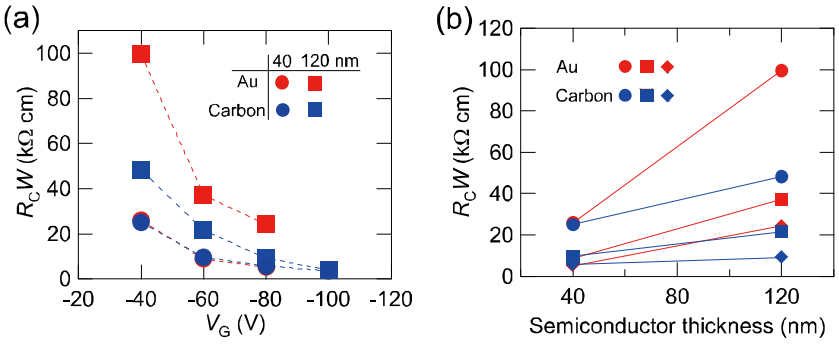

Figure 6-5. (a) V_G dependence of $R_C W$. Red circles and squares represent top-contact Au transistors, and blue circles and squares indicate carbon-electrode transistors with 40 nm and 120 nm active layers, respectively.
(b) Semiconductor-thickness dependence of $R_C W$. Circles, squares, and diamonds represents V_G = –40 V, –60 V, and –80 V.

TABLE I. Characteristics of C6-DBTDT-based transistors: field-effect mobility μ, average mobility μ_{av}, threshold voltage V_{th}, average threshold voltage $V_{th\,av}$, on/off ratio, and contact resistance $R_C W$.

Electrode[a]	C6-DBTDT (nm)	μ [μ_{av}] ($cm^2\ V^{-1}\ s^{-1}$)	V_{th} [$V_{th\,av}$[b]] (V)	on/off	$R_C W$[c] (kΩ cm)
Au BC	40	10^{-5} - 0.038 [0.012]	–11 - –44 [–29]	10^5	
Au TC	40	1.3 - 2.2 [1.7[b]]	–10 - –37 [–17[b]]	10^6	5
	120	0.26 - 0.74 [0.55[b]]	–17 - –30 [–22[b]]	10^5	24
Carbon BC	40	0.60 - 1.2 [0.85[b]]	–8 - –16 [–12[b]]	10^7	6 4[d]
	120	0.40 - 0.84 [0.65[b]]	–10 - –16 [–12[b]]	10^6	9 4[d]

[a]TC: top contact, and BC: bottom contact.
[b]Average for more than 13 transistors.
[c]V_G = –80 V.
[d]V_G = –100 V.

As shown in Figure 6-6 (a), the carbon-electrode thickness is about 5 μm, and this is sufficiently larger than the active layer thickness. In general, the transistor performance of a thin-film transistor is maximized when the active layer is as thin as several ten nm, because the useless "bulk" layer lowers the performance, and because R_{acc} increases with an increase of the thickness. This thickness dependence is also observed in the ordinary bottom-contact transistors.[40] Moreover, since C6-DBTDT molecules are standing perpendicular to the substrate, the resistivity of the resulting thin film is highly anisotropic; the resistivity is high in the longitudinal direction along the insulating long alkyl chain, while the resistivity is low in the lateral direction due to the molecular stacks (Figure 6-6(b)). This also gives rise to the high R_{acc} in top-contact transistors (Figure 6-6(c)). However, in the carbon-electrode transistors, the contact between the electrode and the semiconductor is mostly realized on the side surface (Figure 6-6(a)). Therefore, smooth charge injection is expected parallel to the gate insulating layer (Figure 6-6(d)). Therefore, carbon electrodes are also effective to not only improve the morphology but also suppress R_{acc}, which appears in the perpendicular direction to the gate insulating layer.

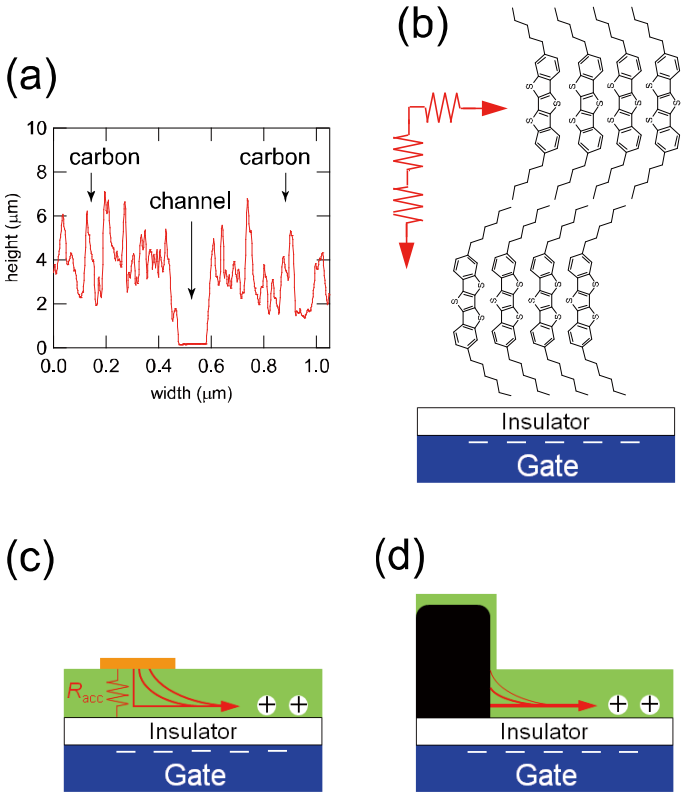

Figure 6-6. (a) Carbon-electrode thickness profile around the channel region. (b) Anisotropy of resistivity in a C6-DBTDT film. Charge-injection process in the (c) metal-top-contact and the (d) carbon-electrode transistors.

6.5 Conclusion

In conclusion, we have investigated charge injection in C_6-DBTDT thin-film transistors. Solution-processed carbon electrodes significantly reduce $R_C W$ of the bottom-contact transistors, which is in the same order as the ordinary Au top-contact transistors. In particular, we have found another type of charge injection process, where R_{acc} is suppressed by the lateral carrier injection from the S/D electrodes. The carbon electrodes provide another solution to reduce R_{acc}, which is different from the ordinary way to make the semiconductor films as thin as possible.

6.5 Reference

1 G. Horowitz, *Adv. Mater.* **10**, 365 (1998).

2 Z. Bao, *Adv. Mater.* (Weinheim, Ger) **12**, 227 (2000).

3 H. Sirringhaus, T. Kawase, R. H. Friend, T. Shimoda, M. Inbasekaran, W. Wu, and E. P. Woo, *Science* **290**, 2123 (2000).

4 C. D. Dimitrakopoulos and P. R. L. Malenfant, *Adv. Mater.* **14**, 99 (2002).

5 K. Takimiya, H. Ebata. K. Sakamoto, T. Izawa, T. Otsubo, and Y. Kunugi, *J. Am. Chem. Soc.* **128**, 12604 (2006).

6 H. Ebata, T. Izawa, E. Miyazaki, K. Takimiya, M. Ikeda, H. Kuwabara, and T. Yui, *J. Am. Chem. Soc.* **129**, 15732 (2007).

7 T. Yamamoto and K. Takimiya, *J. Am. Chem. Soc.* **129**, 2224 (2007).

8 M. J. Kang, I. Doi, H. Mori, E. Miyazaki, and K. Takimiya, *Adv. Mater.* **23**, 1222 (2011).

9 K. Takimiya, S. Shinamura, I. Osaka, and E. Miyazaki, *Adv. Mater.* **23**, 4347 (2011).

10 C. Mitsui, T. Okamoto, H. Matsui, M. Yamagishi, T. Matsushita, J. Soeda, K. Miwa, H. Sato, A. Yamano, T. Uemura, and J. Takeya, *Chem. Mater.* **25**, 3952 (2013).

11 T. Okamoto, C. Mitsui, M. Yamagishi, K. Nakahara, J. Soeda, Y. Hirose, K. Miwa, H. Sato, A. Yamano, T. Matsushita, T. Uemura, and J. Takeya, *Adv. Mater.* **25**, 6392 (2013).

12 C.-a. Di, G. Yu, Y. Liu, X. Xu, D. Wei, Y. Song, Y. Sun, Y. Wang, D. Zhu, J. Liu, X. Liu, and D. Wu, *J. Am. Chem. Soc.* **128**, 16418 (2006).

13 C.-a. Di, G. Yu, Y. Liu, Y. Guo, Y. Wang, W. Wu, and D. Zhu, *Adv. Mater.* **20**, 1286 (2008).

14 Y. Yu, M. Kanno, H. Wada, Y. Bando, M. Ashizawa, A. Tanioka, and T. Mori, *Physica B* **405**, S378 (2010).

15 K. P. Puntambeker, P. V. Pesavento, D. Frisbie, *Appl. Phys. Lett.* **83**, 5539 (2003).

16 I. Kymissis, C. D. Dimitrakopoulos, and S. Purushothaman, *IEEE Trans. Electron Devices* **48**, 1060 (2001).

17 C. Bock, D. V. Pham, U. Kunze, D. Käfer, G. Witte, and Ch. Wöll, *J. Appl. Phys.* **100**, 114517 (2006).

18 K. Fukuda, Y. Takeda, M. Mizukami, D. Kumaki, and S. Tokito, *Sci. Rep.* **4**, 3947 (2014).

19 K. Shibata, H. Wada, K. Ishikawa, H. Takezoe, and T. Mori, *Appl. Phys. Lett.* **90**, 193509 (2007).

20 T. Kadoya, M. Ashizawa, T. Higashino, T. Kawamoto, S. Kumeta, H. Matsumoto, and T. Mori, *Phys. Chem. Chem. Phys.* **15**, 17818 (2013).

21 A. Aumüller, P. Erk, G. Klebe, S. Hünig, J. U. Von. Schütz, and H. P. Werner, *Angew. Chem. Int. Ed. Engl.* **25**, 740 (1986).

22 T. Kadoya, D. de Caro, K. Jakob, C. Faulmann, L. Valade, and T. Mori, *J. Mater. Chem.* **21**, 18421 (2011).

23 Y. Takahashi, T. Hasegawa, Y. Abe, Y. Tokura, K. Nishimura, and G. Saito, *Appl. Phys. Lett.* **86**, 063504 (2005).

24 Y. Takahashi, T. Hasegawa, S. Horiuchi, R. Kumai, Y. Tokura, and G. Saito, *Chem. Mater.* **19**, 6382 (2007).

25 R. Pfattner, C. Rovira, and M. Mas-Torrent, *Phys. Chem. Chem. Phys.* (2015) DOI: 10.1039/c4cp03492a

26 S. Tamura, T. Kadoya, T. Kawamoto, and T. Mori, *Appl. Phys. Lett.* **102**, 063305 (2013).

27 S. Tamura, T Kadoya, and T. Mori, *Appl. Phys. Lett.* **105**, 023301 (2014).

28 T. Kadoya, S. Tamura, and T. Mori, *J. Phys. Chem. C* **118**, 23139 (2014).

29 H. Wada and T. Mori, *Appl. Phys. Lett.* 93, 213303 (2008).

30 T. Minari, T. Miyadera, K. Tsukagoshi, Y. Aoyagi, and H. Ito, *Appl. Phys. Lett.* **91**, 053508 (2007).

31 K. Tsukagoshi, I. Yagi, K. Shigeto, K. Yanagisawa, J. Tanabe, and Y. Aoyagi, *Appl. Phys. Lett.* **87**, 183502 (2005).

32 C. Vanoni, S. Tsujino, and T. A. Jung, *Appl. Phys. Lett.* 2007, **90**, 193119 (2007).

33 T. Minari, P. Darmawan, C. Liu, Y. Li, Y. Xu, and K. Tsukagoshi, *Appl. Phys. Lett.* **100**, 093303 (2012).

34 K-D. Jung, Y. C. Kim, H. Shin, B-G. Park, J. D. Lee, E. S. Cho, and S. J. Kwon, *Appl. Phys. Lett.* **96**, 103305 (2010).

35 Y. Xu, T. Minari, K. Tsukagoshi, J. A. Chroboczek, and G. Ghibaudo, *J. Appl. Phys.* **107**, 114507 (2010).

36 L. Bürgi, T. J. Richards, R. H. Friend, and H. Sirringhaus, *J. Appl. Phys.* **94**, 6129 (2003).

37 Y. Miyata, E. Yoshikawa, T. Minari, K. Tsukagoshi, and S. Yamaguchi, *J. Mater. Chem.* **22**, 7715 (2012).

38 T. Takahashi, S. Tamura, Y. Akiyama, T. Kadoya, T. Kawamoto, and T. Mori, *Appl. Phys. Express* **5**, 061601 (2012).

39 D. Shukla, S. F. Nelson, D. C. Freeman, M. Rajeswaran, W. G. Ahearn, D. M. Meyer, and J. T. Carey, *Chem. Mater.* **20**, 7486 (2008).

40 S. Hoshino, T. Kameta, and K. Yase, *J. Appl. Phys.* **92**, 6028 (2002).

Chapter 7

General Conclusion

In this thesis, how to use chemical doping in organic field-effect transistors, and charge-injection process is investigated. Such a doping is a representative method to induce conductivity in silicon technology, but usually not used in organic electronics. Chapter 1 introduces the recent progress of organic transistors and the background of the present work including the outline of CT complexes. In chapter 2, experimental procedures are presented.

In chapter 3, carrier injection from organic contacts to semiconductor films, TMTTF, is investigated in the thin-film transistors. When TCNQ is patterned on a TMTTF film, the resulting (TMTTF)(TCNQ) works as highly conducting source and drain electrodes. In such self-contact transistors using chemical doping, the organic material constructing the active layer is selectively transformed to the contacts. Such self-contact transistors have achieved low contact resistance and high performance.

In chapter 4, by using ink-jet printing instead of vacuum evaporation, organic field-effect transistors with chemically doped source/drain electrodes are fabricated by selectively transforming the active layer to the conducting organic charge-transfer (CT) complex. The formation of the CT complex is investigated by X-ray diffraction and

raman spectroscopy, and the resulting CT complex is conducting enough to realize satisfactory transistor performance. The solvent of the ink is a key factor to achieve the optimal chemical doping to form a well-ordered CT complex. In such a manner, we can obtain semiconductor-specific electrodes which significantly reduce the Schottky barrier at the electrode/semiconductor interface because ideal energy-level engineering is automatically attained between the same type of molecules.

In chapter 5, an highly conducting organic CT complex derived from an organic-transistor material is described. BTBT ([1]benzothieno[3,2-*b*][1] benzothiophene) is an organic semiconductor that realizes high mobility in organic transistors. The CT complex, $(BTBT)_2PF_6$, shows as high room-temperature conductivity as 1500 S cm^{-1}. The electric state is one dimensional. This compound exhibits a resistivity jump around 150 K, but when covered with Apiezon N grease the resistivity jump is suppressed, and the metallic conductivity is maintained down to 60 K. Owing to the very high conductivity, the ESR signal shows significantly asymmetric Dysonian lineshape (A / $B \cong 3$) even at room temperature. According to the optical properties, the ground state is not regarded as charge order, but attributed to the lattice modulation. Since most organic conductors are based on strong electron donors, it is remarkable that such a weak electron donor as BTBT realizes a stable and highly conducting organic metal.

In Chapter 6, contact resistance of bottom-contact organic transistors based on dihexyl-substituted dibenzo[*d*,*d*']thieno[3,2-*b*;4,5-*b*']dithiophene (C_6-DBTDT) is remarkably reduced by using carbon electrodes. In the Au top-contact transistors, the contact resistance increases in proportion to the semiconductor thickness owing to the access resistance, whereas the performance of the carbon-electrode transistors does not

largely depend on the active-layer thickness. This is attributed to the lateral charge injection from the side of the thick carbon electrode.

These results demonstrate that chemical doping on the semiconductor films is an effective method to reduce the contact resistance, and smooth charge injection is realized by constructing the semiconductor-specific electrodes. In addition, organic semiconductors which realize high mobility have a potential to form new kinds of CT complexes. Although chemical doping and field effect are different methods, the concept that generates the charge carriers in organic compounds is the same. Accordingly, there is a meaningful connection between organic conductors and organic electronics. Exploration of the boundary research area is quite interesting, which has a possibility to establish novel materials chemistry and physics.

List of Publications

The publications contributed to this thesis

[1] S. Tamura, *T. Kadoya, T. Kawamoto, T, Mori / Self-Contact Thin-Film Organic Transistors Based on Tetramethyltetrathiafulvalene / *Appl. Phys. Lett.* **102**, 063305 (2013).

[2] T. Kadoya, S. Tamura, *T, Mori / Energy-Level Engineering in Self-Contact Organic Transistors Prepared by Inkjet Printing / *J. Phys. Chem. C*. **118**, 23139 (2014).

[3] *森健彦、角屋智史 / 化学ドープを用いた有機トランジスタ / 色材協会誌, **86**(12), 456-460 (2013).

[4] 特許出願 2013-34805　2013 年 2 月 25 日出願　特許公開 2013-211534

【発明者】森健彦，角屋智史

【名称】 有機薄膜トランジスタの製造方法及び有機薄膜トランジスタ

[5] *T. Kadoya, M. Ashizawa, T. Higashino, T. Kawamoto, S. Kumeta, H. Matsumoto, T. Mori / A Highly Conducting Organic Metal Derived from an Organic-Transistor Material: Benzothienobenzothiophene / *Phys. Chem. Chem. Phys.* **15**, 17818 (2013).

[6] *T. Kadoya, O. Pitayatanakul, T. Mori / Suppression of Access Resistance by Carbon Electrodes in organic transistors Based on Alkyl-Substituted Thienoacene / *Org. Electronics to be submitted*.

The publications not included in this thesis

[1] Y. Wang, T. Kadoya, L. Wang, T. Hayakawa, M. Tokita, T. Mori and *T. Michinobu / Benzobisthiadiazole-based conjugated donor-acceptor polymers for organic thin film transistors: effects of π-conjugated bridges on ambipolar transport / *J. Mater. Chem. C* **3**, 1196 (2015).

[2] *O. Pitayatanakul, T. Higashino, T. Kadoya, M. Tanaka, H. Kojima, M. Ashizawa, T. Kawamoto, H. Matsumoto, K. Ishikawa, *T. Mori / High Performance Ambipolar Organic Field-Effect Transistors Based on Indigo Derivatives / *J. Mater. Chem. C* **2**, 9311 (2014).

[3] S. Tamura, *T. Kadoya, T, Mori / All-Organic Self-Contact Transistors / *Appl. Phys. Lett.* **105**, 023301 (2014).

[4] *T. Higashino, T. Kadoya, S. Kumeta, K. Kurata, T. Kawamoto, T. Mori / An Organic Metal Derived from a Selenium Analogue of Benzothienobenzothiophene / *Eur. J. Inorg. Chem.* **24**, 3895 (2014).

[5] T. Takahashi, S. Tamura, Y. Akiyama, T. Kadoya, T. Kawamoto, *T. Mori / Organic Field-Effect Transistors Based on Small-Molecule Organic Semiconductors Evaporated under Low Vacuum / *Appl. Phys. Express.* 5, 061601-061603 (2012)

[6] T. Kadoya, D.de Caro, K. Jakob, C. Faulmann, L. Valade, *T. Mori / Charge Injection from Organic Charge-Transfer Salts to Organic Semiconductors / *J. Mater.*

Chem. **21**, 18421-18424 (2011).

[7] *D. de Caro, K. Jacob, H. Hahioui, C. Faulmann, L. Valade, T. Kadoya, T. Mori, J. Fraxedasd, L. Viaue / Nanoparticles of Organic Conductors: Synthesis and Application as Electrode Material in Organic Field Effect Transistors / *New J. Chem.* **35**, 1315-1319 (2011).

List of Conferences

International conference

[1] T. Kadoya, M. Ashizawa, T. Kawamoto, S. Kumeta, H. Matsumoto, ○T. Mori / A New Charge-Transfer Salt, $(BTBT)_2PF_6$ / International Symposium on Materials Science Openes by Molecular Degrees of Freedom (MDF2012) / O-18 / Miyazaki, Japan / Dec.,2012

[2] T. Kadoya, ○T. Mori, D. de Caro, K. Jakob, C. Faulmann, L. Valade / Organic Electronics Based on Organic Charge-Transfer Complexes / International Symposium on Crystalline Organic Metals,Superconductors and Ferromagnets (ISCOM 2011) / I-14 / Poznan, Poland / Sep.,2011

[3] ○T. Kadoya, S. Tamura, T. Kawamoto, T. Mori / Self-Contact Organic Transistors Using Chemical Doping / International Conference on Science and Technology of Synthetic Metals (ICSM 2014) / P2.035 / Turku, Finland / June, 2014

[4] ○T. Kadoya, M. Ashizawa, T. Higashino, T. Kawamoto, S. Kumeta, H. Matsumoto, K. Yamamoto, T. Mori / Molecular Conductor Derived from an Organic-Transistor Material / International School and Symposium on Molecular Materials (ISSMM 2013) / P15 / Tokyo, Japan / Nov.,2013

[5] ○S. Tamura, T. Kadoya, T. Kawamoto, T. Mori / All-Organic Self-Contact

Transistors / International School and Symposium on Molecular Materials (ISSMM 2013) / P17 / Tokyo, Japan / Nov.,2013

[6] ○S. Tamura, T. Kadoya, T. Kawamoto, T. Mori / All-Organic Self-Contact Transistors / The 2012 International Conference on Flexible and Printed Electronics (ICFPE2013) / G05-P06 / Korea / Sep.,2013

[7] ○T. Kadoya, M. Ashizawa, T. Higashino, T. Kawamoto, S. Kumeta, H. Matsumoto, T. Mori, K. Yamamoto / Highly Conducting Organic Radical-Cation Salt $(BTBT)_2PF_6$ Based on a Weak Electron Donor / International Symposium on Crystalline Organic Metals,Superconductors and Ferromagnets (ISCOM 2013) / PII-12 / Montréal, Canada / July,2013

[8] ○T. Higashino, T. Kadoya, T. Kawamoto, T. Mori / Synthesis, Structure, and Physical Properties of $(DBrBTBT)_3X_2(PhCl)_2$ / International Symposium on Crystalline Organic Metals,Superconductors and Ferromagnets (ISCOM 2013) / PI-11 / Montréal, Canada / July,2013

[9] ○T. Kadoya, T. Mori / Ink-Jet Printing of Self-Contact Organic Transistors / The 2012 International Conference on Flexible and Printed Electronics (ICFPE2012) / Tokyo / Sep.,2012

[10] ○S. Tamura, T. Kadoya, T. Kawamoto, T. Mori / Organic Field-Effect Transistors Based on TMTTF under Low Vacuum / P25 / England / Sep.,2012

[11] ○T. Kadoya, T. Mori / Organic Field-Effect Transistor with Solution-Processed Charge-Transfer-Salt Electrodes / International Conference on Science and Technology of Synthetic Metals (ICSM 2012) / USA / July,2012

[12] ○T. Kadoya, D. de Caro, K. Jakob, C. Faulmann, L. Valade, T. Mori / Organic Transistors Using Charge-Transfer Complex Microparticles as Electrode Materials

/ International School and Symposium on Multifunctional Molecule-based Materials (ISSMMM 11) / D6 / Argonne, Chicago, USA / Mar.,2011

Domestic conference

[1] ○角屋智史, 森健彦 / 塗布型カーボン電極を用いたボトムコンタクト型C6-DBTDTトランジスタ / 第75回応用物理学関係連合講演会 / 17p-A4-6 / 北海道 / 2014年9月

[2] ○角屋智史, 田村純香, 森健彦 /印刷法を用いたセルフコンタクト有機トランジスタⅡ / 第61回応用物理学関係連合講演会 / 19a-E3-1 / 東京 / 2014年3月

[3] ○T. Higashino, T. Kadoya, T. Kawamoto, T. Mori, O. Jeannin, M. Fourmigué/ Charge-Transfer Complexes with Tetragonal Crystal Symmetry / 2nd Workshop on Strongly Correlated Electron and Complex Systems: From Intermetallics to Molecular Materials / Lisbon, Portugal / Nov.,2013

[4] ○田村純香, 角屋智史, 川本正, 森健彦 / 有機物のみで形成したセルフコンタクト型トランジスタ /第 74 回応用物理学会秋季学術講演会 / 20a-C5-1 / 京都 / 2013年9月

[5] ○角屋智史, 山本薫, 芦沢実, 川本 正, 松本 英俊, 森健彦 / 有機伝導体$(BTBT)_2PF_6$の伝導性と低温ラマンスペクトル / 日本物理学会 / 27pXF-4 / 広島 / 2013年3月

[6] ○田村純香, 角屋智史, 川本正, 森健彦 / HMTTFを用いたセルフコンタクト型有機トランジスタ /第60回応用物理学会秋季学術講演会 / 20a-C5-1 / 神奈川 / 2013年3月

[7] ○角屋智史, 山本薫, 芦沢実, 川本 正, 松本 英俊, 森健彦 / 有機伝導体

$(BTBT)_2PF_6$ の伝導性と低温ラマンスペクトル / 日本物理学会　/ 27pXF-4 / 広島 / 2013 年 3 月

[8] ○角屋智史, 芦沢実, 川本 正, 松本 英俊, 森健彦 / 有機伝導体$(BTBT)_2PF_6$ の伝導性と結晶構造 / 日本物理学会　/ 20aHA7 / 横浜 / 2012 年 9 月

[9] ○角屋智史, 芦沢実, 久米田 翔平, 川本 正, 松本 英俊, 森健彦 / 有機伝導体$(BTBT)_2PF_6$の構造と物性/第 6 回分子科学討論会　/ 1C-15 / 東京/ 2012 年 9 月

[10] ○角屋智史, 森健彦 / 有機電荷移動錯体電極を用いた有機トランジスタと電荷移動現象 / 日本化学会第 92 春季年会　/ 3 A5-44 / 神奈川 / 2012 年 3 月

[11] ○角屋智史, 森健彦 / 印刷法を用いたセルフコンタクト有機トランジスタ / 第 59 回応用物理学関係連合講演会 / 17a-F9-1 / 東京 / 2012 年 3 月

[12] ○藤末智夏, 角屋智史, 東野寿樹, 川本正, 森健彦 / ジベンゾピロロピロールを用いた電荷移動錯体の構造と物性 / 1P059 / 広島 / 2014 年 9 月

[13] ○増田 直彰, 東野 寿樹, 角屋 智史, 小田島 岳史, 芦沢 実, 川本 正, 松本 英俊, 森 健彦 / イソインジゴ誘導体を活性層に用いた有機電界効果トランジスタ / 3P062 / 広島 / 2014 年 9 月

[14] ○田村純香, 角屋智史, 川本正, 森健彦 / TMTTF を用いた有機トランジスタ/ 第 73 回応用物理学会学術講演会 / 13p-PB2-21 / 愛媛 / 2012 年 9 月

[15] ○Joungmin Cho, 秋山雄斗, 角屋智史, 森健彦 / Variable Temperature Characteristics of n-Channel Organic Transistors Using DMDCNQI / 第 73 回応用物理学会学術講演会 / 13p-PB2-26 / 愛媛 / 2012 年 9 月

[16] ○角屋智史, D.de Caro, K.Jakob, C.Faulmann, L.Valade, 森健彦 / 有機電荷移動錯体から有機半導体へのキャリア注入 / 第 72 回応用物理学会学術講演

会 / 30a-R-2 / 山形 / 2011 年 8 月

[17] ○角屋智史, D.de Caro[3], K.Jakob, C.Faulmann, L.Valade, 森健彦 / 電荷移動錯体微粒子を電極に用いた有機トランジスタ / 第 58 回応用物理学関係連合講演会 / 24a-BU-8 / 神奈川 / 2011 年 3 月